UNIVERSITÀ DEGLI STUDI DI MILANO

Facoltà di scienze Matematiche Fisiche e Naturali

Ph.D. Thesis in Physics

FAST: a scintillating tracker for antiproton cross section measurements

Author: **Aldo Mozzanica**
Supervisor: **Prof. Ileana Iori**
Co-supervisor: **Dr. Michela Prest**

Contents

Introduction **1**

1 Cross section measurement at the Cern AD **3**
1.1 The antiproton discovery 3
1.2 The low energy antiproton challenge 5
1.3 The $\bar{p}$ interaction at low energies: an open problem . . 7
1.4 The Antiproton Decelerator beam 10
1.5 The layout of the measurement 13

2 Fast timing scintillating fiber trackers **19**
2.1 Physics of scintillating fiber detectors 19
2.1.1 Light production and collection 19
2.1.2 Light to charge conversion 27
2.2 Existing fiber trackers 36
2.2.1 The UA2 fiber detector 36
2.2.2 The D0 Scintillating Fiber Central Tracker . . . 37

3 Detector design and simulation **41**
3.1 Defining the detector module 41
3.1.1 The photodetector 42
3.1.2 The fibers and their layout 42
3.2 The detector electronics 47
3.2.1 The frontend ASICs 47
3.2.2 The frontend boards 49
3.2.3 Post production board characterization 57
3.2.4 The repeater boards 59
3.2.5 Completing the DAQ system 61
3.3 Test of a stereo prototype at the Beam Test Facility . . 63
3.3.1 The prototype and the beam line 63
3.3.2 Results of the stereo prototype beam test 65
3.4 The FAST detector 69
3.4.1 The tracker assembly 69
3.4.2 Montecarlo simulation of the detector 72

4 FAST commissioning and physics expectations 79
4.1 The cosmic ray run 79
4.1.1 Adapting FAST for cosmic ray detection 79
4.1.2 Time resolution 81
4.1.3 Efficiency 84
4.1.4 Cross talk 85
4.1.5 Hit reconstruction and resolution results 87
4.2 Data taking at the ASACUSA beam line 92
4.2.1 The ASACUSA beam line 92
4.2.2 The experimental setup 94
4.2.3 Tuning the antiproton beam 97
4.2.4 Towards the cross section measurements 102

5 The FAST system in other physics fields 107
5.1 Sampling logic for a neutron Time of Flight 107
5.1.1 Neutrons from radiotherapic accelerators 107
5.1.2 The detector 108
5.1.3 Flux measurements 111
5.1.4 Arrival time measurements 112
5.1.5 Montecarlo simulation 112
5.2 VLSI readout of a GEM detector 115
5.2.1 The GEM detectors: principles and properties . 115
5.2.2 The ASACUSA frontend board for the GEM readout 116
5.2.3 Results at the Frascati BTF 117
5.3 The scintillating fiber profilometer 120
5.3.1 The profilometer assembly 121
5.3.2 The results at the Frascati BTF 123
5.3.3 Results on the SPS H8 beam line 125

Conclusions and outlooks 129

A An apparatus for $\bar{p}$ studies: the OBELIX detector 133

B The FAST DAQ software 139

List of acronyms 143

List of figures 150

List of tables 151

Introduction

The dynamics of the antiproton-nucleus ($\bar{p}$A) interaction and the structure of the nucleus appear to affect in an unexpected way the behaviour of the $\bar{p}$A annihilation cross section (σ_{ann}) at low energies. In light nuclei the $\bar{p}$D and $\bar{p}$ ^{4}He annihilation cross sections at a $\bar{p}$ momentum below 60 MeV/c drop to the $\bar{p}$-p level, whereas at higher momenta they increase regularly with the number of nucleons in the nuclei. Low statistics measurements of both the $\bar{p}$ ^{20}Ne and the $\bar{p}$ ^{3}He annihilation cross section at around 60 MeV/c show a saturation effect of σ_{ann} with the mass number A at decreasing $\bar{p}$ momentum, suggesting a strong dependence on the nucleus structure.
The goal of our group, as a part of the ASACUSA collaboration (AD3, CERN), is to reach a better understanding of the behaviour of $\sigma_{ann}(\bar{p}\text{A})$ through $\bar{p}$ annihilation cross section measurements able to confirm the existing low statistics results (for ^{3}He and ^{20}Ne) and with new measurements to be performed with heavier nuclei and at even lower energies.
The Antiproton Decelerator machine, the only slow antiproton facility now running, has been designed and tuned for the antiHydrogen production and spectroscopy measurements: it delivers a very high intensity $\bar{p}$ bunch (up to 5×10^7 particles) in a 200 ns time window, with a repetition period of 120 s.
This beam structure places some major constraints on the cross section measurement and on the detector requirements; in particular the detector has to:

- Provide a time separation between the on-target annihilations and the huge background produced when the antiproton bunch reaches the end wall of the system

- Perform an annihilation vertex reconstruction to separate in-target events from wall events given by the beam halo

- Cover a fiducial volume large enough to contain (in the transverse direction) not only the beam core but also the beam tails.

To meet these requirements a scintillating fiber tracker (FAST, Fiber Antiproton Scintillating Tracker) has been developed; this PhD Thesis will discuss the design, the development, the commissioning of the FAST detector and the results of the data taking.
The first Chapter of this work is a review of the most interesting results in Antiproton Physics during the last 50 years, with a particular focus on the status of the low energy cross section experiments; for a better analysis of the problems involved in this kind of measurements, the most recent experimental apparatus, the OBELIX detector, is described (Appendix A).
The second Chapter focuses on detectors; since the detector chosen for our experiment is a scintillating fiber tracker, in this Chapter the most advanced fiber detection systems are reviewed. To introduce the topic, a general summary on the scintillating fiber physics is presented showing the pros and cons of this kind of detector.
The third Chapter describes the ASACUSA detector, a 2500 channel scintillating fiber tracker readout by 42 multianode photomultipliers and Very Large Scale of Integration (VLSI) electronics. The choice of the design has been validated both with montecarlo simulations and with dedicated beam tests on prototypes. More in detail, the results obtained with the prototypes have been used to check the detector performance and to obtain the figures used by the simulation to define the geometrical constraints of the device. The assembly and testing procedures of both the sensor and the electronics boards are reported too.
The tracker has been tested with cosmic rays to characterize the efficiency, the time resolution and the spatial resolution. The fourth Chapter describes this detector commissioning phase and reports the results of the data collected on the Antiproton Decelerator beam line.
In the last Chapter some applications of the system developed for the $\bar{p}$-nucleus measurement in different physics fields are shown.
In particular the frontend electronics has been used in Medical Physics, allowing a Time of Flight neutron detection in a radiotherapic environment, and in imaging applications, connected to a GEM pad detector.
A modified version of the detector module has been used as a beam profile monitor with a large energy range and high rate capabilities at the CERN SPS H8 beam line.
For each application an overview of the framework and its specific problems, with a particular focus on the advantages of our system with respect to traditional ones, will be given and the results of the measurements will be reported.

Chapter 1

Cross section measurement at the Antiproton Decelerator

This Chapter, after a brief historical introduction on the antiproton physics, will give a review of the existing data regarding the antiproton annihilation cross section at low energy, with particular focus on the theoretical problems that are still open and that cannot be solved for the lack of experimental data.
In the second half of the Chapter the measurement that has been proposed, with the aim of solving these ambiguities, will be presented: the Antiproton Decelerator machine and the constraints it places on the measurement will be described; then the layout of the experiment itself will be reported in detail.

1.1 The antiproton discovery

The concept of antimatter has been introduced by Dirac in 1927: his new equation for the electron had a second positively-charged solution; even if, at the beginning, the proton was used to explain this extra solution, he finally arrived to the concept of antimatter, predicting a positively charged counterpart of the electron, the so called anti-electron [1].
Four years after Dirac's prediction, in 1932, the first positron tracks have been experimentally observed by Anderson in the cosmic rays, with the help of a cloud chamber placed in a magnetic field. Anderson himself detected the first electron–positron pair production from a high energy γ ray (from a Thorium source) [2].
On the wave of this exciting discovery, the idea of antimatter has

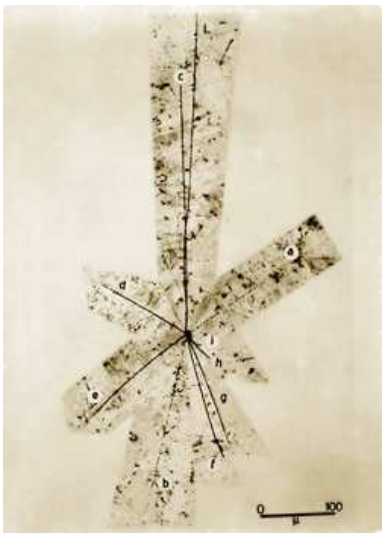

Figure 1.1: The first antiproton annihilation event detected with the emulsion-stack, at the Bevatron, a few days after the antiproton discovery (based on momentum and velocity measurements). The antiproton enters from the top of the image and travels about 400 μm before hitting a proton. Nine charged particles are emitted from their mutual annihilation.

been promptly extended to the strong interaction domain, with the assumption that, for any hadron, a corrisponding anti-hadron should exist, with the same mass and spin but opposite electric charge.
Searches for the antiproton, the proton counterpart, were soon performed in the cosmic rays by means of cloud chambers and photographic emulsions. Although a few tracks that could be identified as antiprotons were detected, these measurements couldn't say the last word on the antiproton existence [3][4][5].

The existence of the antiproton was definitively demonstrated, in 1955, at the Bevatron accelerator at Berkeley; the antiprotons were produced by sending a 6 GeV proton beam on a solid target and were detected by measuring independently the momentum (with a magnetic quadrupole spectrometer) and the velocity (with a ToF system and a Cherenkov discrimination) [6]; soon after, the measurement was confirmed by the detection of the annihilation "star" signature in the emulsion-stack detector (see Fig. 1.1).
One year after, the existence of the neutron counterpart, the antineutron, was experimentally demonstrated again at Berkeley [7].

1.2 The low energy antiproton challenge

Soon after the discovery of the antiproton, beams consisting in these "new" particles were produced trying to use the antiprotons to investigate the annihilation physics. Already in the early '60s, stopping the antiprotons in bubble chambers filled with Hydrogen, the first data on the annihilation on protons or neutrons were obtained at Brookhaven [8][9][10], at CERN [11] and at KEK [12][13]. These experiments, thus demonstrating that the $\bar{p}$-p annihilation is a powerful tool to study meson resonances, used partially separated antiproton beams produced from an external target; as a result they were characterized by a low rate of stopped antiprotons over large volumes and by a large contamination of undesired particles, like muons, pions and electrons. These facts limited the statistics and the accuracy of these early experiments. For this reason, and thanks to the progresses in the antiproton collection and cooling techniques pushed by the necessities of the 300 GeV CERN proton-antiproton collider (Sp$\bar{p}$S), several methods to obtain slow antiprotons have been developed, resulting in the Low Energy Antiproton Ring (LEAR) construction at CERN in the '80s [14]. In the following the sequence of operations performed by the decelerator is described (see Fig. 1.2).

A 10^9 $\bar{p}$ bunch, coming from the Antiproton Accumulator (AA) serving the Sp$\bar{p}$S, was injected in the Proton Synchrotron ring every 30 minutes; the antiprotons were decelerated by the PS machine at 600 MeV/c and then transferred to the LEAR ring. Here successive phases of deceleration and stochastic cooling were applied to slow the beam down to 300 MeV/c. To reach even lower energies maintaining a low momentum dispersion, an electron cooling technique was used: with this method the antiprotons transfer their energy to a cool electron beam, comoving with the $\bar{p}$, which is continuously injected in the beam line; the electron beam is then dumped bringing away the energy surplus of the antiprotons. This system allowed to obtain, with the LEAR machine, particles as slow as 105 MeV/c (5 MeV of kinetic energy).

The LEAR facility could deliver to the experiments antiproton beams with a typical momentum spread $\Delta p/p \simeq 0.1\%$ and a very slow extraction that enabled essentially DC beams to be produced, with spills lasting up to hours, intensities in the range $10^4 \div 10^6$ $\bar{p}$/s and a 100% beam purity.

In the 13 years of operation of the LEAR machine, from 1983 to 1996, several experiments were carried out, among which the most important are ASTERIX, in the first phase, and OBELIX and Crystal BARrell (CBAR) in the second one; these experiments have brought many,

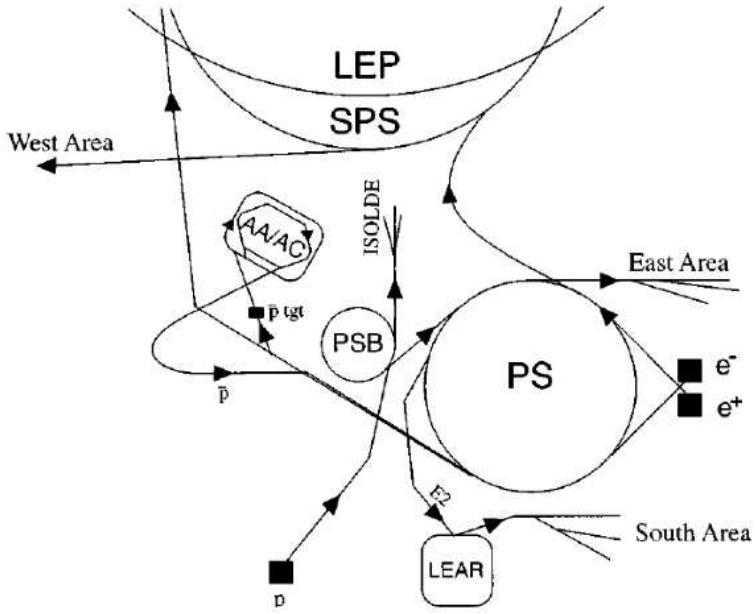

Figure 1.2: The PS complex and the LEAR machine. The protons from the Linac were pre accelerated by the PS Booster (PSB) before being injected into the PS. After the acceleration up to 26 GeV/c the protons hit the target used for the $\bar{p}$ production. Antiprotons were collected by the Antiproton Collector (AC) and stored into the Antiproton Accumulator (AA). AA and AC were two concentric rings. Then the beam was transferred to the PS for being decelerated, and finally delivered to LEAR for the last deceleration phase.

very high precision and sometimes surprising, antiproton physics results.

While a detailed review of the experiments held at LEAR is beyond the goal of this work, a description of the OBELIX detector with an example of an annihilation cross section measurement is given in App. A.

After the closure of the LEAR facility, CERN has continued its involvement in the low energy antiproton physics with the construction of the Antiproton Decelerator (AD). However, this machine (see Sec. 1.4 for a description) is not devoted to the intense experimental study of low energy antiproton annihilation processes: in fact the goal of AD is the production of trapped antiHydrogen and the formation of light antiprotonic atoms.

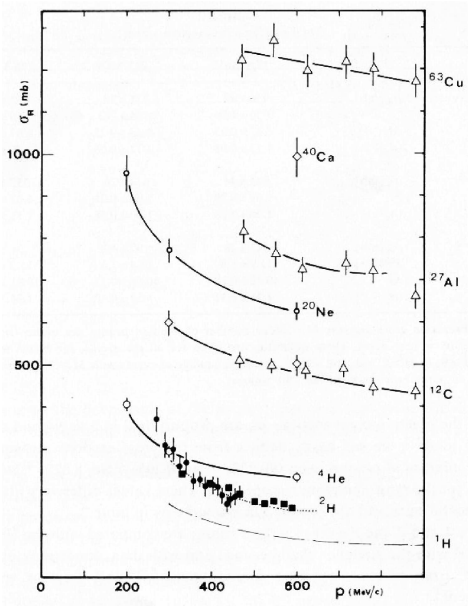

Figure 1.3: Antiproton annihilation cross section for p, D, ^{3}He, ^{4}He and Ne for incident momenta between 200 MeV/c and 800 MeV/c. The momentum is expressed in the laboratory frame. See text for references.

1.3 The $\bar{p}$ interaction at low energies: an open problem

The measurements, performed during the '80s at LEAR, of $\bar{p}$ and $\bar{n}$ annihilations on nuclei in the 200÷600 MeV/c momentum range showed a dependence of the cross section from the target mass of the kind $\sigma_{ann} \simeq \sigma_0 A^{2/3}$ [15][16]. Moreover the behaviour of σ_{ann} with the incident momentum is independent from the target nucleus, and is similar to the $\bar{p}$-p one (see Fig 1.3). This seems to suggest that the most important reaction process is the nucleon-antinucleon interaction, and that the nucleon can be considered quasi-free; the "surface" $A^{2/3}$ term can be explained, in this scenario, with the fact that only the surface nucleons are involved. As far as antineutron data are concerned, this situation can be extended to the lower energy region, down to ∼60 MeV/c, at least for medium heavy (Z>4) target nuclei [17][18]. On the other hand the $\bar{p}$ annihilation cross section on light nuclei seems to be rather weakly dependent on the mass of the target nuclei in the low momentum range (<100 MeV/c) [19][20][21].

Fig. 1.4 shows a summary of the available data for antiproton and antineutron cross sections at momenta below 100 MeV/c. A few interesting behaviours can be noticed: the data for $\bar{p}$-^{4}He and $\bar{p}$-D in-

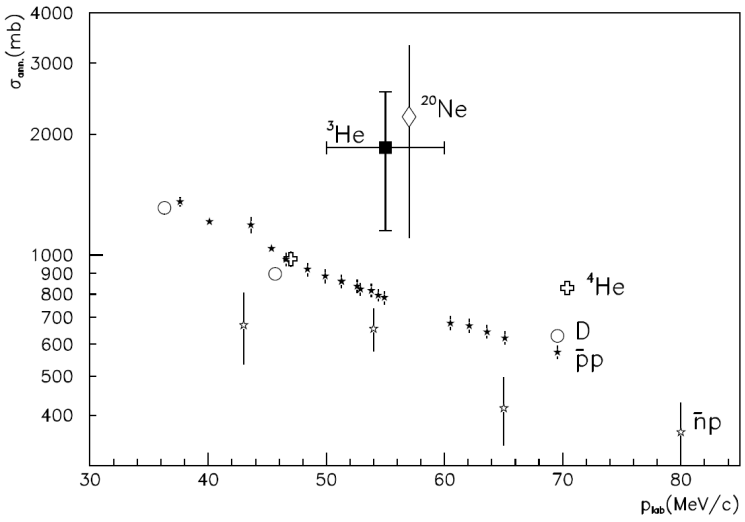

Figure 1.4: Antiproton annihilation cross section for p, D, ^{3}He, ^{4}He and Ne for incident momenta below 100 MeV/c. Full stars and empty stars correspond respectively to $\bar{p}$ and $\bar{n}$. The momentum is expressed in the laboratory frame. See text for references.

tersect the $\bar{p}$-p trend in the momentum region between 40 MeV/c and 60 MeV/c, so that the cross section for these nuclei is higher than the proton one at high incident momenta but becomes lower reducing the momentum. Moreover, the Neon σ value is not as high as expected: in fact, once the Coulomb contribution is subtracted, the Neon cross section is as small as the $\bar{p}$-p one [21]. Finally, the ^{3}He values are twice as large as the ^{4}He ones at the corresponding energies. Such a large rate in ^{3}He can be explained only by a special role played by the structure of this nucleus. Within errors, the ^{3}He cross section is the sum of the Deuteron and Hydrogen cross sections, suggesting that in the ^{3}He case, the role of the extra proton with respect to the Deuteron case, is of key relevance [22].

On the interpretation side, different theoretical predictions actually exist as far as the cross section dependence on the atomic number is concerned.

For strongly absorbed particles such as low-energy antiprotons, disregarding the Coulomb potential, it can be assumed that a total absorption occurs if the projectile has an impact parameter smaller than the radius R of the nucleus or, equivalently, if it has an orbital angular momentum smaller than $l_{\max}$, where semiclassically $l_{\max} + 1/2 = kR$ (k being the particle momentum). However, due to the focusing effect of the attractive Coulomb potential, also particles with impact param-

eters larger than R interact with the nucleus, thus causing the cross section to increase. If the low energy Coulomb problem is treated in a semiclassical approach, assuming that total absorption occurs in all partial waves for which the distance of closest approach is smaller than R, the following relation between the Coulomb-modified $l_{\max}$ and R is obtained [23]:

$$\left(l_{\max} + \frac{1}{2}\right)^2 \simeq (kR)^2 \left(1 + \frac{2Z\mu e^2}{k^2 R\hbar^2}\right) \tag{1.1}$$

where e is the electric charge, μ is the reduced mass of the $\bar{p}$-nucleus system, Z is the atomic number and $\hbar$ is the reduced Planck constant. At very low energy the last bracket of the second term is $>> 1$, so that $l_{\max} >> kR$ due to the focusing effect of the Coulomb potential. Since the contribution of each partial wave to the cross section is equal to the area of the annulus with radius equal to the impact parameter $b = l/k$:

$$\Delta\sigma_l = \pi((b + \Delta b)^2 - b^2) = \frac{\pi}{k^2}(2l + 1) \tag{1.2}$$

and the total reaction cross section is the sum of all the l contributions:

$$\sigma_R = \sum_{l=0}^{l_{\max}} (\Delta\sigma_l) = \frac{\pi}{k^2}(l_{\max} + 1)^2 \tag{1.3}$$

Eq. 1.1 can be used to compute the total cross section. Substituting Eq. 1.1 into Eq. 1.3, being $(l_{\max} + 1) \simeq (l_{\max} + 1/2)$ for large $l_{\max}$:

$$\sigma_R \simeq \pi R^2 \left(1 + \frac{2Z\mu e^2}{k^2 R\hbar^2}\right) \tag{1.4}$$

At very low energy (low k) the second term within the brackets, which represents the Coulomb focusing effects, becomes dominant; in this case, given that the radius of the nucleus $R \propto A^{1/3}$, the cross section has a $ZA^{1/3}$ dependence.

Unfortunately this simple picture seems to be hardly compatible with the existing data: in fact, $ZA^{1/3}$ should give a greater separation (among various nuclei) with respect to the $A^{2/3}$ behaviour that fits the experimental points at high energies, which is not the case (Fig. 1.4 shows indeed an opposite trend).

Moreover, if a computation of the total annihilation cross section is performed within an optical potential model, the results have a strong dependence on the free parameters, and can be very different: for Protasov et al. [24][25][26] the $A^{2/3}$ behaviour should still be valid in this momentum range (if the light nuclei are excluded), while for Gal et al. [27][28] the correct dependence is determined by a saturation effect

such that the $ZA^{1/3}$ behaviour is restored only for very high A values. Because of the low statistics for the ^{20}Ne and ^{3}He targets[1] and because of the lack of information for heavier nuclei, it is impossible to disentangle the problem just using these experimental data: several theoretical predictions are simply compatible with the measured points.
For this reason our group, in the framework of the ASACUSA (Atomic Spectroscopy And Collisions Using Slow Antiprotons) experiment, has proposed a new measurement of the antiproton annihilation cross section to be performed at the CERN Antiproton Decelerator.

1.4 The Antiproton Decelerator beam

The Antiproton Decelerator (AD) has been developed for (laser induced) spectroscopy experiments [29]: given the moderately short lifetime of the studied states and since the laser power is limited, such experiments can be performed at best with a high intensity bunched beam, so that the laser (or lasers) can be fired against the highest number of antiprotonic targets.
As a result, the Antiproton Decelerator is designed to extract all the accumulated particles (up to 10^8) in a single bunch (or in a few bunches) a few hundreds of nanoseconds long.
A cross section measurement like the one proposed by ASACUSA was classically performed (for example at LEAR) with the so called "slow extraction" of the beam: a small fraction of the particles circulating in the ring was extracted at each revolution. In this way isolated particles were reaching, with a poissonian time distribution, the target and the detectors.
In the case of the AD machine, this kind of extraction is impossible by design. This fact makes a cross section measurement far more problematic: for this reason, the detector and the measurement method itself have been developed trying to overcome the limits created by the extremely high intensity of the Antiproton Decelerator bunch. It is worth to remember that AD is the only running machine that is capable to deliver a low energy antiproton beam, and this is not going to change before the start up of FLAIR[2], the next generation machine for antiproton studies, foreseen in 7-10 years.
These limits and the proposed solutions will be discussed in Sec. 1.5, while in the following the AD working principles are described.
The intense beam from the Proton Synchrotron (1.5×10^{13} protons

[1] The ^{20}Ne cross section has been computed observing 7 annihilation events [21].
[2] The Facility for Low-energy Antiproton and Ion Research in development at the GSI research center.

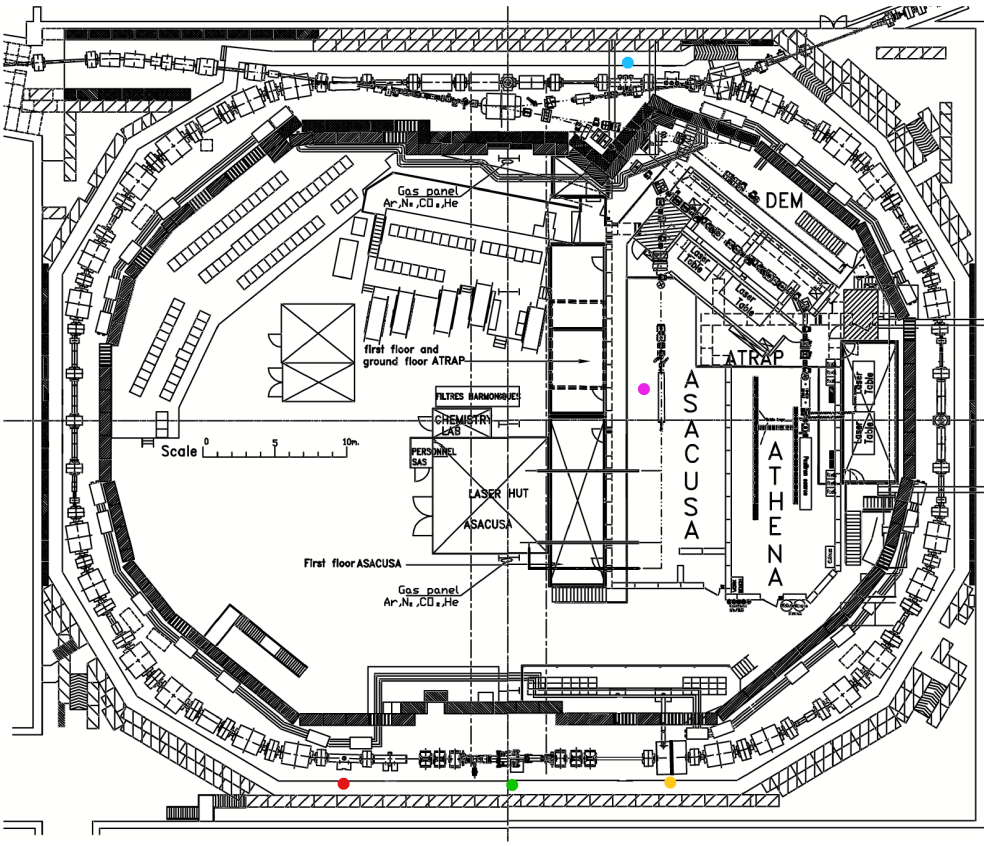

Figure 1.5: The plan of the Antiproton Decelerator, with the main ring, the injection line and the transfer lines to the three experimental areas: ASACUSA, ATRAP and ALPHA (formerly ATHENA).

in 500 ns) impinges, with a 26 GeV/c momentum, on a target [30] producing antiprotons with a wide momentum spectrum: particles with 3.57 GeV/c are focused by a magnetic horn into the transfer line which delivers the beam to the AD ring (Fig. 1.5).

After the injection, the Antiproton Decelerator Cycle begins (Fig. 1.6). It consists of the following steps:

- The beam is debunched so that it can be stochastically cooled: this cooling phase lasts ∼20 s
- The beam is bunched again and decelerated by the Radio Frequency (RF) cavity down to 2 GeV/c
- A second stochastic cooling is performed (∼15 s); this is needed to keep the momentum spread inside the acceptance of the RF cavity

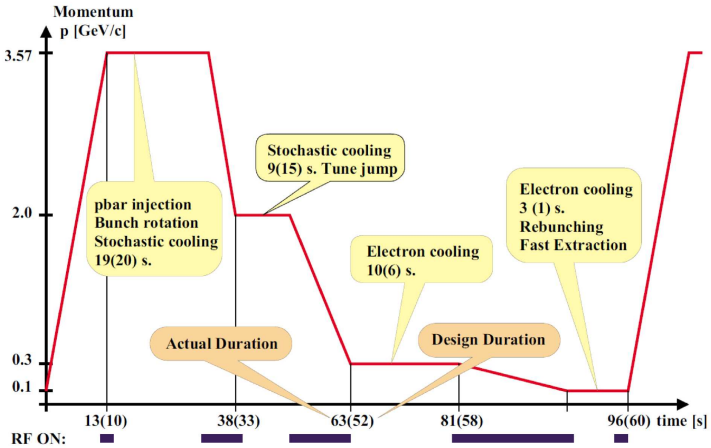

Figure 1.6: The Antiproton Decelerator cycle. Times are indicative, since they may vary with the efficiency of the cooling system. From [30].

- The (bunched) beam is decelerated down to 300 MeV/c
- The beam is debunched and the electron cooling is applied, for 10 s
- The RF system bunches the beam and slows it down to 100 MeV/c (5 MeV of energy)
- A second electron cooling is applied for a few seconds
- At this point the low energy beam is cool and ready for the extraction phase.

The effects of the decelerations and the coolings on the beam emittance[3] and momentum spread is shown in Tab. 1.1. Just before the extraction the RF cavity is switched on: depending on its frequency, from one to six bunches can be obtained (namely 1,2,3,6 bunches are allowed). At this point the bunches are travelling into the AD ring: a magnetic septum (i.e. a fast dipole), which is turned on just before the crossing of a bunch and turned off soon afterwards, can extract the bunches, one after the other, and send them to the transfer line that delivers the beam to the experimental areas.
The bunch time length is ∼200 ns for the single bunch, and it decreases if the number of bunches increases, to reach ∼200/6 ns if 6 bunches are extracted.
The total length of the Antiproton Decelerator Cycle is about 120 s:

[3]The emittance is defined as the area of the smallest ellipse that effectively contains, in the phase space, the particles of the beam.

Momentum (GeV/c)		Emittance (πmm·mrad)	Momentum Spread (%)
3.75	before s.c.	200	1.5
	after s.c.	5	0.1
2.0	before s.c.	9	0.18
	after s.c.	5	0.3
0.3	before e.c.	33	0.2
	after e.c.	2	0.1
0.1	before e.c.	6	0.3
	after e.c.	1	0.01
0.1	bunched	1	0.1

Table 1.1: Transverse emittance and momentum spread during the various phases of the AD cycle. S.c. and e.c. stand respectively for stochastic and electron cooling. Just before the ejection the beam is compressed in space (bunched) by the RF, so the momentum spread increases. Data from [31].

during this time a fraction of the injected $\bar{p}$s is lost, so that from 5% to 30% of the incoming particles are actually reaching the experiments. This wide range of values shows how sensitive the AD machine is to the tuning of the parameters. At its best, $\sim 3 \times 10^7$ $\bar{p}$s were measured by the Shotcky pick-up placed on the transfer line just before the experimental areas (with one extracted bunch) [31].
It is worth to note, even if this comment is already evident from the cycle description, that the Antiproton Decelerator is a very complicate machine, with more than 120 high current high stability (at a 10^{-4} level) magnets, a decelerating Radio Frequency, a wide band stochastic cooling and an electron beam used for the cooling at low momentum: all these components have to be switched with a perfect timing several times during the deceleration cycle.
As a further example, to avoid beam losses and momentum spreads due to the multiple scattering on the residual gas molecules, the vacuum inside the AD ring is 5×10^{-13} bar, ten times lower than the one used in the PS complex [32].
A description of the ASACUSA beam line is presented in Sec. 4.2.1.

1.5 The layout of the measurement

As reported in the previous paragraph, the Antiproton Decelerator could deliver to the ASACUSA experimental area up to 6 high intensity bunches, with a duration as short as few tens of ns, every 2 minutes. This sets a number of constraints on the measurement scheme:

- When the bunch arrives at the blank flange at the end of the apparatus pipe (end wall in the following), the antiprotons promptly annihilate and a huge number (more than 10^6) of charged pions are emitted: even if the end wall is located a few meters apart, the fraction of these particles that reaches the detector is enough to saturate it. This means that the annihilation events have to occur and to be detected before this time
- The previous point implies that the shortest possible bunch has to be preferred. But a short bunch means that, for a given time resolution of the detector, less annihilation events per bunch can be identified: the target "thickness" has to be reduced, so also the statistics is reduced
- No kind of beam collimation can be used near the detector, since secondary pions would impinge on the tracker, with a high probability to saturate it
- For the same reason, the tails and the halo of the beam must not reach the pipe and the vessel walls: the beam has to be small in size, and well centered
- No beam monitor can be placed upstream or in correspondence of the detector: a solid one would stop completely the beam and a grid one would produce too many secondary particles. As a consequence the previous point is hard to accomplish. In principle, a beam monitor could be placed near the end wall
- The thickness of the target itself has to be limited, since the multiple scattering on a thick target could increase the beam divergence and so the probability that a particle, after the scattering, is bended torwards the walls: if more than a tiny fraction ($10^{-4} \div 10^{-5}$) of the particles hits the pipe walls, the tracking becomes impossible
- The incoming particles cannot be counted, so only integral measurements are available for the intensity, limiting the accuracy in case of absolute cross section measurements.

To overcome these issues, the measurement setup of Fig. 1.7 has been proposed.

An ultra high vacuum pipe, with two valves and the pumping system, is directly connected to the AD beam pipe; the diameter is kept large, to avoid as much as possible any collision of the beam tails with the pipe walls. The target element is sputtered on a < 1 μm thick mylar[4]

[4]Commercial name of biaxially-oriented polyethylene terephthalate.

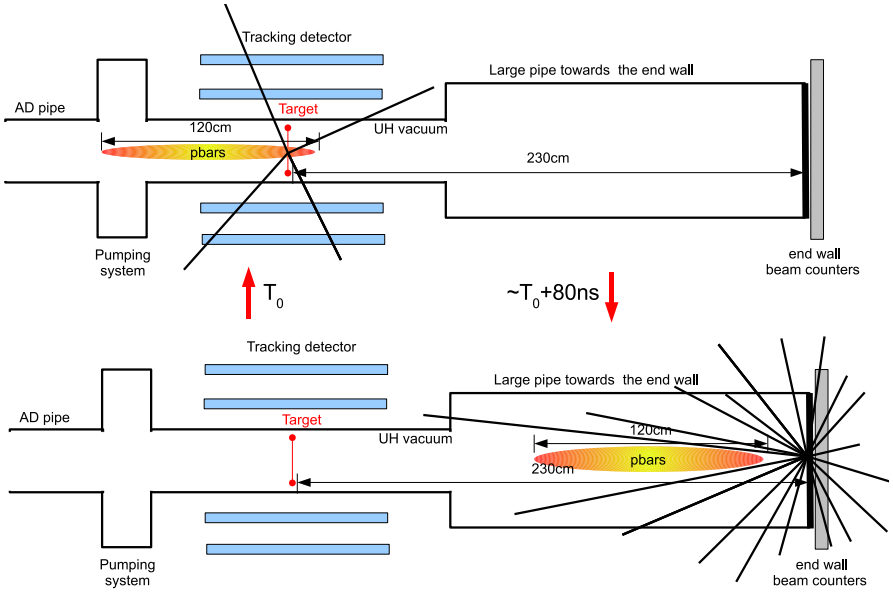

Figure 1.7: Scheme of the proposed experimental setup. The antiproton bunch reaches the target where a few annihilations occur: the outcoming pions (the thick lines) are detected by the tracker, to reconstruct the vertices and count the events. When the front of the antiproton cloud reaches the end wall, a huge number of pions is produced, so the tracker is completely saturated. The FWHM length of the $\bar{p}$ bunch is here represented, assuming a $\sim$20 ns r.m.s. bunch as suggested by the AD experts. The multiple scattering on the target enlarges the transverse size of the beam.

foil tightened on an iron circular frame, which is placed in the middle of the pipe. When the antiproton cloud crosses the target, one (or very few) in flight annihilation can occur. To count them, the pipe is surrounded by a tracking detector which is able to reconstruct the annihilation vertices. After the target, the vessel diameter is increased, to reduce the probability that the diverging particles hit the pipe walls, so that almost every particle can reach the end wall, located quite far, at 2.3 m from the target. Here a huge number of particles is created: the large size of the pipe does not allow the efficient use of any lead shielding, so the tracker detector is completely saturated as soon as the antiproton cloud front reaches the end wall. A detector with high dynamic range is placed near the end wall, to monitor the incoming antiproton multiplicity and the time structure of the beam.
It is clear that the measurement critically depends on the bunch length: all (or most of) the particles have to cross the target before its front hits the end wall. If the bunch is longer than the target–end wall distance, the tracker is saturated before it can detect any annihilation

in the target itself.
Given the antiproton speed of ∼3.0 cm/ns (at 5 MeV) and assuming a gaussian time structure of the beam, a safety margin should be guaranteed by the 20 ns r.m.s. time spread foreseen by the AD experts: when the 3σ head of the $\bar{p}$ cloud reaches the end wall, the center of the cloud is ∼50 cm after the target (180 cm from the end wall).
The thinnest mylar foil that can be used for the target is 0.9 μm, a non negligible thickness for low energy antiprotons: it already accounts for half of the maximum acceptable scattering material (for a divergence small enough to avoid most of the wall background).
For this reason, and given the problems in the antiproton number evaluation, the proposed measurement is only relative: the idea is to compare the number of in flight annihilations on the mylar+X (X=Ni, Sn, Pt) samples with respect to those on the mylar alone. The main constituent (in terms of atom number, not weight) of mylar is Hydrogen. Thus, the measurement will allow to compare the cross section of Hydrogen with respect to higher Z materials (up to Platinum). An automatic or manual system to change the target has to be provided.

The detector requirements

The scheme just described sets a number of requirements on the tracking detector for the in flight antiproton cross section measurement. Before listing them, it is useful to explain why a tracking detector was needed to count the annihilation events. In each $\bar{p}$-p annihilation an average number of 3.1 charged pions with a < 900 MeV/c momentum (~ 300 MeV/c is the most probable value) are emitted [33].
In principle, one could think to perform the measurement with some kind of counting detector, and evaluate the annihilation number on an average basis. Anyway, without a full track reconstruction it is impossible to distinguish between the annihilations on the target and on the wall, which are supposed to be not completely avoided. Moreover, the background is expected to be high, since any small loss of a bunch of 10^6 particles, for example in the transport line, will likely produce a number of secondary particles.
As a consequence, a tracking detector with the following features is needed:

- A space resolution for the annihilation vertices of the order of 1 cm, to allow a good separation between wall and target events
- A time resolution as high as possible, to associate the reconstructed hits and tracks with the correct physics event. In particular this is useful in case of a high background: if the time res-

olution is not good enough, the tracks generated by background events will superimpose to the annihilation ones, hiding them

- A good overall efficiency, since the repetition rate of the Antiproton Decelerator is low
- A low duty cycle: the detector has to be active for some hundreds of nanoseconds six times every two minutes
- A moderately fast readout time: the 6 bunches are extracted from AD at one second distance
- Easy to install on the beam line, since different experiments share the ASACUSA beam line, so a short time for the switch over is available
- Easy to operate, since it should be operated by a small crew
- Whenever possible, a conservative design should be used, given the short time available from the design phase to the data taking. In fact, for the ASACUSA program, the measurements at 5 MeV should end by 2007: after, with the RFQD[5] always operating, only lower energy antiprotons will be available
- A limited cost.

As a last consideration, the detector design has to consider two future measurement configurations, for which it should meet the requirements with no or little modifications:

- A measurement at 5 MeV with a gas target: in this case the annihilations can occur at any position inside the pipe, so the detector should have a large fiducial volume. Moreover the lateral spread is increased due to the multiple scattering effects in the entrance window and in the gas itself. The detector should be large enough to house a larger gas vessel
- A measurement with 1 keV antiprotons produced by the ASACUSA MUSASHI[6] decelerator: since the slow $\bar{p}$s exiting from the RFQD+MUSASHI apparatus are randomly distributed in a few seconds time interval, the sampling gate of the detector has to be increased by orders of magnitude. On the other hand, the sampling resolution can be decreased, since the events are isolated in time.

[5]Radio Frequency Quadrupole Decelerator, that is the apparatus used by the ASACUSA collaboration to slow down the antiprotons to ∼50 keV.

[6]Monoenergetic Ultra-Slow Antiproton Source for High-precision Investigations.

Chapter 2

State of the art of fast timing scintillating fiber trackers

Already in the late '50s, soon after the development of scintillators as a detector medium for charged particles and for gamma spectroscopy, lots of efforts have been put in trying to use them for tracking, following the idea that a longitudinally segmented scintillator, where light is forced to travel in a given direction by the internal reflections, can give the projected optical image of the particle track at the detector face [34][35]. This idea, which is the basis of all scintillating fiber trackers, found a real application only in the '80s, taking advantage of the developments in the field of optical fibers and light detection techniques [36].
The goal of this Chapter is to report the last 20 years of developments in scintillating fiber detectors.
The first part is dedicated to an introduction on the scintillating fiber physics and on the different light detection methods.
In the second part, a review of some of the most important present and past fiber trackers is presented.

2.1 Physics of scintillating fiber detectors

2.1.1 Light production and collection

In order to understand the properties of plastic scintillating fibers, a short introduction on the mechanism of light production inside an organic scintillator will be given.

Scintillation mechanism

Given the fact that scintillating fibers have essentially the same properties of plastic scintillators as far as the interaction with radiation is concerned, in the following only the scintillation mechanism in organic scintillators will be considered. An analysis of the scintillation process in inorganic scintillators can be found in [37].
Differently from the inorganic scintillator case, where the whole crystalline structure participates to the light production process, in the organic materials light emission is an intrinsic molecular property of the aromatic hydrocarbons they consist of.
The basic component ($\sim$98% in weight) of a plastic scintillator is a polymeric material such as polystyrene, polyvinyltoluene (PVT) or polymethylmethacrylate (PMMA) and gives to the scintillator its optical and mechanical properties; furthermore it absorbs the energy of the ionizing particles to be detected and transfers it with a rather good efficiency to the benzene rings of the dye via a nonradiative dipole-dipole interaction known as Forster Transfer [38]. An energy deposit of about 5 eV is required to excite a base molecule of the material and the efficiency of the transfer process is of the order of 3% [39].

The benzene rings are systems with a large number of vibrational levels for the π electrons, as shown in Fig. 2.1. If a ionization process occurs (e.g. a ionizing particle crosses the molecule), the electron is likely to be excited to a higher energy state with a random vibrational state; in a very short time (10^{-12} s) a vibrational relaxation, with the exchange of energy with neighbouring molecules, occurs, bringing the electron to the lowest of the excited states from which it decays in a few ns emitting a photon (this phenomenon is known as fluorescence). In principle the photon can be absorbed by another benzene ring, but this process is suppressed since the average photon energy is not enough to put the electron in one of the available vibrational states. Thus the primary photon can travel inside the scintillator for a few millimeters before being self-absorbed. For most applications the light path from the production point to the scintillator exit wall is longer than a few millimeters, so a second fluorescent component is added in the material compound.

This component (waveshifter) absorbs the primary scintillation light with a high cross section and re-emits light of longer wavelength; being the absorption cross section very large for the primary γs, a small concentration (0.01-0.1%) can be used so that the probability of reabsorption is very low. As a result, the attenuation length λ_{att} of the secondary light is large enough ($\lambda_{att} \geq$2 m) to let the light reach the photodetector. The properties of the most common waveshifters are

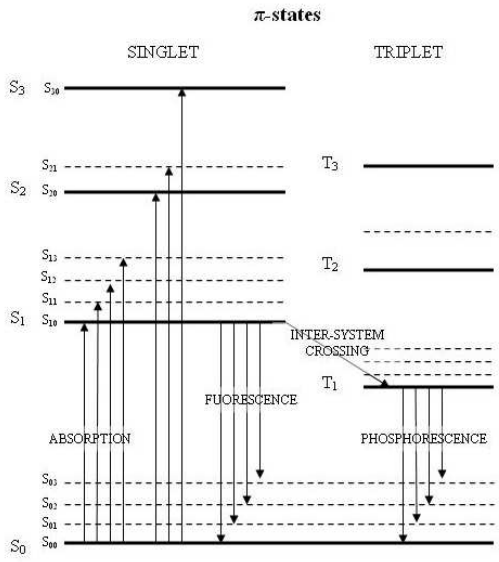

Figure 2.1: Energy states for a π electron in an organic molecule. S_0 is the ground state, S_1 is the first singlet excited state and T_1 the first triplet state, while S_{00}-S_{0n} are the vibrational sublevels. Note that the fluorescence transition $S_1 \rightarrow S_0$ has a lower average energy than the transition $S_0 \rightarrow S_1$, thus reducing the self absorption effect. The decay time of the T_1 states (phosphorescence) is an order of magnitude larger than the fluorescence decay time. For this reason materials with low phosphorescence probability are chosen for detectors.

Short name	Full name	λ_{peak} (nm)	Decay time (ns)	Q.E.
PBD	phenyl-biphenyl-diazole	360	1.1	0.92
POPOP	p-bis-phenyloxazolyl-benzene	410	1.4	0.93
bis-MSB	p-bis-methylstyryl-benzene	420	1.3	0.94
3HF	3-hydroxyflavone	510	<1	0.36

Table 2.1: Properties of the most widespread waveshifters; the quantum efficiency (Q.E.) is the ratio between the number of absorbed and emitted photons. The attenuation length varies with the concentration; the 3HF, given the very small overlap between emission and absorbtion spectra, can be used in higher concentrations, so it is a good candidate for small diameter fibers.

listed in Tab. 2.1.
Tab. 2.2 reports the properties of a general purpose polyvinyltoluene plastic scintillator.

Light collection in scintillating fibers

In bulk scintillators the light reaches the readout system (e.g. a photomultiplier) undergoing reflections on the detector walls; the efficiency

Density	1.032 g/cm^3
Refractive Index	1.58
Softening point	70°C
Light output	∼8000 photons/MeV
Rise time	0.9 ns
Decay Time	2.4 ns
Wavelength of maximum emission	424 nm
Attenuation length	250 cm
C atom density	$5.23 \cdot 10^{22}$ 1/cm^3
H atom density	$4.74 \cdot 10^{22}$ 1/cm^3

Table 2.2: Bicron BC-400 plastic scintillator properties (from datasheet).

depends on the scintillator dimension, on the geometry and on the ratio between the photodetector window and the material walls: typically from 10% to 20% of the emitted photons can reach the photodetector, while the remaining photons are absorbed in the volume for the finite attenuation length or at the walls for inefficiencies in the reflections.
In the case of fibers the situation is more complex. A scintillating fiber is made of an inner polystyrene core, acting as the scintillating material, and an outer cladding region made of a material of lower refractive index (Fig. 2.2). The light remains inside the fiber itself due to the total reflection (Snell law) at the core cladding interface. To increase the light collection properties, a second cladding with an even lower refractive index can be used. The intermediate cladding is needed also to provide mechanical bonding between the polystyrene and the outer cladding. In principle the thickness of the cladding could be reduced to a few multiples of the wavelength needed to contain the exponentially decreasing electromagnetic wave; in practice, the cladding extends to some tens of μm, so that it can provide mechanical resistance and protect the core from chemical attacks.
Polystyrene has a lower mechanical strength if compared to PVT or PMMA, materials widely used in bulk scintillators, so it is easier to bend; moreover it can be easily extruded, simplifying the fiber production process.
If a charged particle crosses the scintillating fiber (Fig. 2.3), it releases energy along its whole path; the energy is locally converted in primary scintillation light, which is isotropically emitted from the points of the track. The concentration of the secondary fluorine is kept higher than in bulk scintillators, so this primary light can only travel for a fraction of millimeter before being absorbed. The wavelength shifter promptly re-emits the light again isotropically.

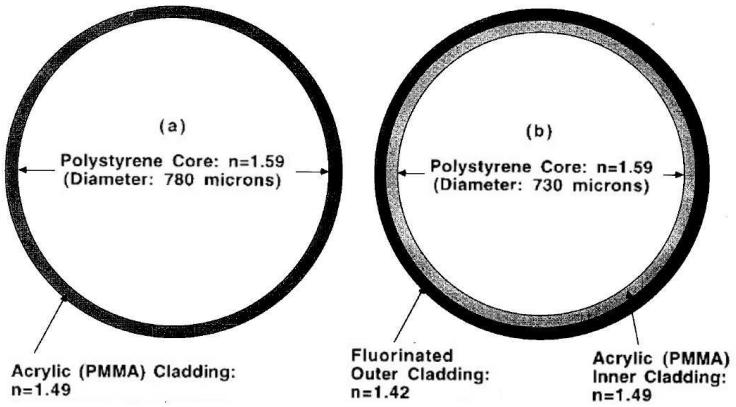

Figure 2.2: Cross section of a single and a double cladding scintillating fiber, with a total diameter of 830 μm. From [40].

The light emitted on the fiber axis is collected by the fiber if it is emitted within a cone whose aperture angle is $\alpha = (\pi/2 - \theta_c)$ (Fig. 2.4), where θ_c is the critical angle of the Snell reflection law given by $\sin\theta_c = \dfrac{n_{clad}}{n_{core}}$; the rest of the light exits from the fiber and should be absorbed by an extra mural absorber (EMA) to avoid cross talk effects in the nearby fibers. The solid angle defined by the cone is given by $2\pi(1 - \cos\alpha)$, so the fraction ϵ of the light collected in the forward cone is $\epsilon = \dfrac{1}{2}\left(1 - \dfrac{n_{clad}}{n_{core}}\right)$.
The typical refractive index of Fig. 2.2 gives $\theta_c \simeq 70^\circ$ and $\epsilon \simeq 3.2\%$ for a single clad fiber and $\epsilon \simeq 4.9\%$ for a double clad fiber. It is worth noting that $\alpha \simeq 30^\circ$ is also the angle of the light cone emitted at the end face of the fiber towards the photodetector.

Moving away from the axis, the collected light doesn't identify a cone anymore but a more complex shape. In fact the rays emitted in the plane containing the fiber axis are still collected within the cone, but out of this plane a bigger angle is accepted; these out of axis rays (skew rays) describe an approximated helical path around the fiber axis. The attenuation of the light on these longer paths partially cancels the increase in the acceptance angle. The net effect, experimentally measured, is a 10-30% increase of the collected light with respect to the value expected for a point-like source on the fiber axis [41].
Another feature of the skew rays is the weak dependence of the collected light from the distance between the particle track and the fiber axis. Increasing the distance, the crossed scintillating material de-

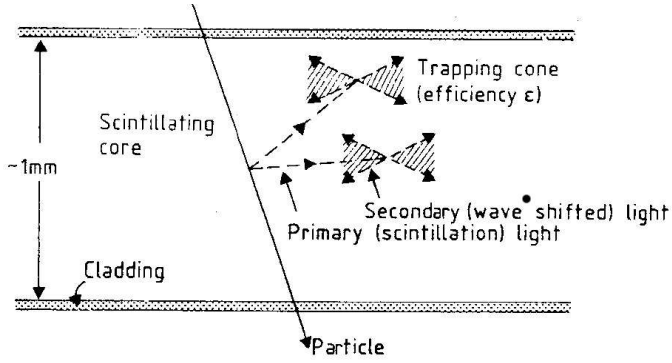

Figure 2.3: When a particle crosses a fiber, an isotropic flux of primary fluorescence photons is emitted along the whole path. This light is immediately absorbed by the waveshifter centers, and re-emitted in all directions: only the fraction within the trapping cone is collected by the fiber. From [41].

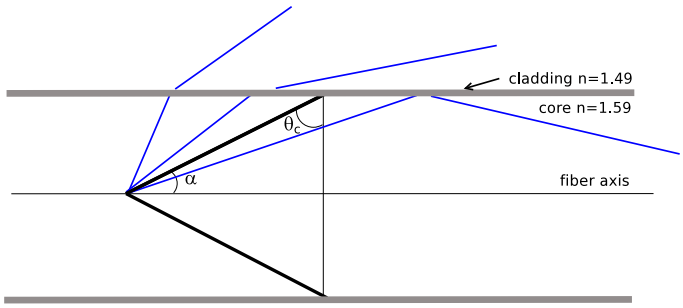

Figure 2.4: The light emitted on the fiber axis is collected within a cone whose aperture angle is $\alpha = \frac{\pi}{2} - \arcsin\left(\frac{n_{clad}}{n_{core}}\right)$, while the γs outside this cone escape from the fiber. The refractive indeces of Fig. 2.2 are used. Angles are not to scale.

creases, but the collection efficiency gets higher because of the contributions of the skew rays: as a result the total light yield is approximately constant over more than 80% of the fiber diameter.
The light collection mechanism becomes much more inefficient when the fiber diameter is reduced; if the attenuation length λ_{att} of the primary scintillation light (that is of the order of 0.5 mm) becomes comparable with the fiber radius r, a large fraction of that light escapes from the fiber before being absorbed by the secondary fluorine, so that, in the limit in which $\lambda_{att} \gg r$, the collection efficiency drops from ϵ to ϵ^2. A reflective layer (e.g. Aluminum) outside the fiber cladding, that reflects back the primary scintillation light into the fiber more and more times, could solve the problem, but it is mechanically difficult to implement on small fibers. It is possible to increase

to a certain extent the secondary fluorine concentration to reduce the attenuation length of the primary light, but the self absorption effect then becomes important reducing the transport properties of the fiber itself. As a result, the smallest diameter for a scintillating fiber of useful length ($\sim$1 m) and good efficiency is of the order of 500 μm.
The number of photons that reach the photodetector for a minimum ionizing particle (m.i.p.) crossing a 1 mm diameter fiber can be computed taking into account all the steps of the process. For the following calculations the data of Tab. 2.3, which refers to the Bicron BCF-10 fibers used in this thesis work, are considered. The energy release of

Core Refractive Index	1.60
Inner Clad Refractive Index	1.49
Outer Clad Refractive Index	1.42
Core Density	1.05 g/cm^3
Inner Clad Thickness	3% of fiber ø
Outer Clad	1% of fiber ø
Trapping Efficiency ϵ	$\sim$5%
Light Output	$\sim$8000 photons/MeV
Decay Time	2.7 ns
Wavelength of maximum emission	432 nm
Attenuation length	220 cm

Table 2.3: Bicron BCF-10 scintillating fiber properties. The core is made of polystyrene, the inner clad of acrylic, the outer one of fluor-acrylic (from datasheet).

a m.i.p. in polystyrene is $< \frac{d\mathrm{E}}{dx} > \simeq 2 \ \frac{\mathrm{MeV}}{\mathrm{cm}}$, and the average path of one particle (considering a uniform flux of particles perpendicular to the fiber axis) is $\frac{\pi}{4} \times$ diameter = 786 μm, so the average energy deposited in the scintillator is $<$ E $>\simeq$157 keV. The number of generated photons can be computed if both the efficiency of the energy transfer to the primary fluorine and the one of the wavelength shifting processes are known; the producers generally don't give these numbers separately, but the product of the two, the so called light output, which for the BCF-10 is $\simeq 8000 \ \frac{\mathrm{photons}}{\mathrm{MeV}}$.
Of the $\sim$ 1250 emitted γs, a fraction ϵ, corresponding to 62 γs (for double cladding fibers), is trapped in the fiber and moves towards the photodetector, while the same amount propagates in the opposite direction. This light can be reflected back if the end face of the fiber is aluminized, with a good improvement in the light yield.
In the path from the track point to the photodetector (at a distance z), the light is attenuated by a factor $e^{-\frac{z}{\lambda_{att}}}$ with $\lambda_{att} \simeq 2$ m for BCF-

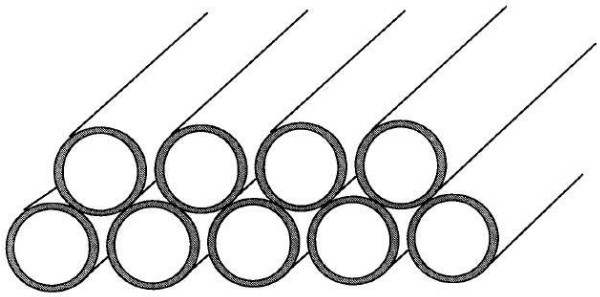

Figure 2.5: The basic element of a scintillating fiber detector is the fiber doublet ribbon, where the upper layer is offset by half the pitch; with this configuration both good efficiency and good spatial resolution are obtained.

10 fibers. In case of a 1 m long fiber, $\simeq 38$ γs arrive to the exit wall near the photodetector; at this interface a fraction ($\simeq 0.1$) of the light is reflected and lost. At the end of the process no more than 35 γs reach the photodetector.

The fibers as detector building blocks

Scintillating fibers can be arranged in different ways to build the basic detection element of a tracking system.
The simplest way is to put the fibers one beside the other on a single plane, but this configuration is characterised by dead areas in the region between fibers. The distance between the sensitive volumes is in fact at least twice the cladding thickness (~ 50 μm) and if tracks are too far from the fiber axis the energy release is too small to generate a detectable signal. A much better configuration is the fiber doublet ribbon of Fig. 2.5: dead areas are avoided, the crossed material is rather constant with the transit position, and a better spatial resolution can be achieved. In this configuration, with individual fiber readout, the spatial resolution can be even better than the digital resolution $\sigma = \frac{p}{\sqrt{12}}$, where p is the readout pitch, since the hits giving signals on 2 fibers are localized in a well defined overlapping region. The spatial resolution of a 830 μm diameter fiber doublet, with a 415 μm readout pitch, measured during the D0 detector commissioning, can be as good as 100 μm [42].
It is important to note that no increase in the resolution can be achieved exploiting the analog information of the fiber (that is the signal proportional to the number of incoming γs), for two reasons: the number of photons is usually so low that statistical fluctuations are the dominant effect, and the light yield has a very small depen-

dence on the track to axis distance, as shown in the previous section. Better resolutions can be obtained only reducing the size of the fiber, or using more fiber planes.
A different configuration can be used if square fibers are available, since they can provide a more uniform space coverage at the expense of a worse light transmission property: the dead region due to the cladding can be avoided with a moderate tilt if a single fiber layer is used. The square shape is ideal for multi layer detectors, reaching in this way a very good resolution with high efficiency. With 10 layers of 0.5 mm square fibers and a shift between planes of 50 μm, a resolution as good as 25 μm has been obtained for a low divergence beam (Fig. 2.6) [43]. The shorter attenuation length of square fibers limits their use to compact detectors made of fibers shorter than 1 m.

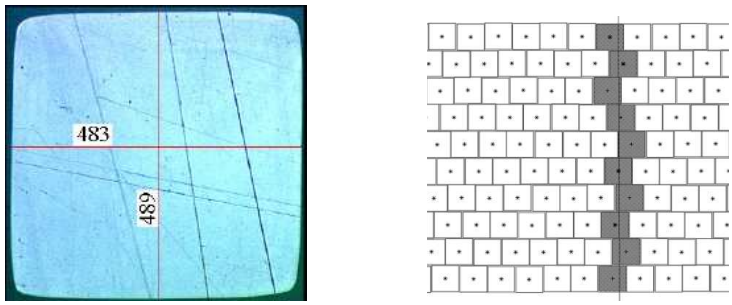

(a) (b)

Figure 2.6: (a) Microscope picture of a (scratched) 500 μm square fiber. (b) Drawing of a square fiber configuration, where the fibers hit by a particle are highlighted; 10 planes of staggered 500 μm fibers allow a 25 μm resolution with $\sim$ 100% efficiency.

2.1.2 Light to charge conversion

The small number of photons reaching the readout interface has been probably the biggest challenge for the development of scintillating fiber trackers. In fact, to maintain a reasonable efficiency, the light conversion system should give an electric signal for a number of incoming photons of a few tens. Moreover, the ideal photoconverter should have:

- A good spectral matching between the scintillation light and the photodetector sensitivity window
- A time resolution below the ns level to fully exploit the good time resolution of the fiber itself
- A small dead time to allow high rates per channel

- An output signal large enough to avoid preamplification and noise issues
- Compactness, because a large number of channels has to be connected not far from the tracking volume
- The capability to work in a magnetic field
- A low cost.

Of course no real system exists with all these properties, but these are the terms different devices are compared on. It is important to note that the device linearity with the incident light is not always requested; the number of photons is given by statistics, so usually the system can be operated in threshold mode without any substantial loss. The most widespread photoconverters for scintillating fiber readout can be divided into vacuum based (Photomultipliers, Micro Channel Plates) and solid state (Avalanche Photodiodes, Visible Light Photon Counters, Silicon Photomultipliers) devices. The following sections describe their features.

Charge Coupled Devices (CCD) with light intensifier

A compact and cost-effective[1] multichannel readout system for a scintillating fiber tracker can be assembled using a multi stage light intensifier with a CCD chip collecting the secondary light; a Micro Channel Plate is usually inserted in the intensifier chain to provide fast time gating. A scheme of a two stage photodetector is presented in Fig. 2.7. The electrons converted at the photocathode are accelerated and focused on a first phosphor screen, which lights a second photocathode. Photoelectrons are multiplied with a Micro Channel Plate and hit a second phosphor screen and a lens system conveys the light to a CCD device. There is no need of a 1 to 1 matching between the scintillating fibers and the CCD pixels, since the low cost per channel of the CCD allows a much easier oversampling of the fiber face, with the light of a single fiber readout by more than one pixel. Such a system exploits both the high gain of the image intensifier and the high granularity of the CCD devices; the last feature in particular allows the use of fiber diameters as small as 25 μm [44]. One major drawback of this type of photodetector is the poor timing capability; the full frame readout of a single CCD needs up to 10 ms, so no fast signals such as the ones used for trigger are available. Even if an independent trigger is used and the trigger rate is low enough, the image intensifier system has an intrinsic time resolution dominated by the phosphor decay time

[1] Considering the cost per channel.

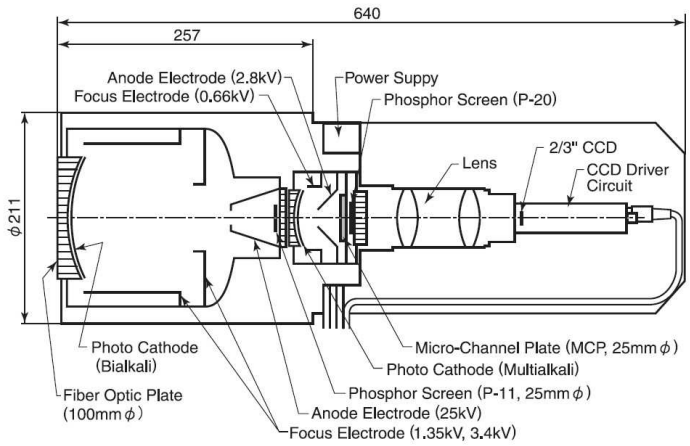

Figure 2.7: The image intensifier system with CCD readout developed for the K2K scintillating fiber detector; the total gain in the photoyield is ≈ 5000. From [45].

($\tau \sim$40 ns), so that the good gating capability of the Micro Channel Plates can't be fully exploited.
The focusing system is negatively affected if a too strong magnetic field is applied, but the device can still work for moderate magnetic fields and the metal shielding of the low number of image intensifiers is possible. Other drawbacks are the low radiation hardness of the CCD chip and eventually the degradation of the MCP performances due to age.

The Multianode Photomultipliers

A standard photomultiplier readout, while commonly used for fiber readout for example in calorimetry, is not feasible for the large number of channels of a tracking system. To overcome this problem, since the late '80s, the major PMT producers have developed the so called Multianode Photomultiplier. A Multianode PMT is a single vacuum tube with a flat photocathode, a dynode system with many different channels for electron multiplication and a segmented anode (Fig. 2.8); in this way the device behaves like many different PMTs sharing the same case and the same voltage divider thus greatly increasing compactness and cost effectiveness. The performances of a Multianode Photomultiplier, summarized in Tab. 2.4, are similar to the standard photomultiplier ones, except for a slightly reduced gain. In particular they provide a very fast response with a dispersion on the pulse rise times better than 0.5 ns, so they can fully exploit the timing capabilities of the fiber systems. Two important issues of these devices are the

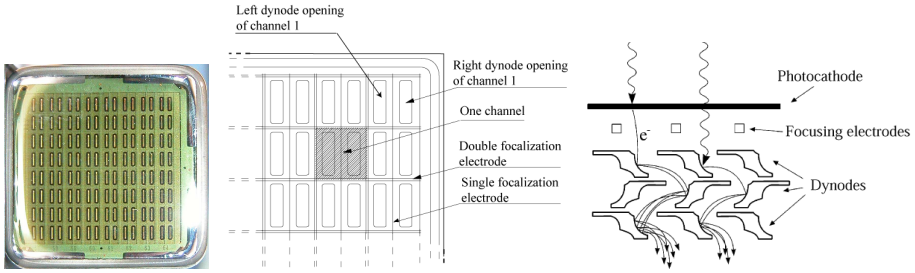

(a) (b) (c)

Figure 2.8: (a) A picture of the front face of the Hamamatsu H7546 Multianode Photomultiplier, used for the FAST detector. (b) Drawing of the face itself. (c) Scheme of the multiplication process inside a MA-PMT; at the end of each dynode chain the electrons are collected by different pads.

channel by channel gain dispersion and the cross talk between adjacent pads. The first effect can be taken into account with a calibration and channel by channel threshold correction. The latter, which is harder to solve, needs to be treated more in detail.

The light on a cell of the photocathode can give an electric signal on

Number of channels	8×8
Anode size	2×2 mm^2
Cathode sensitivity	70 μA/lm
Quantum Efficiency at peak wavelength	0.21
Gain	3.0×10^5
Anode Dark Current	0.2 nA
Rise Time	1.0 ns
Transit Time Spread	0.3 ns

Table 2.4: Main parameters of a Hamamatsu R7600-M64 photomultiplier (from datasheet). More parameters are listed in Tab. 3.1.

a nearby pad because of three different processes [46]:

- The light can reach the wrong region of the photocathode and produce a photoelectron that will be multiplied in the wrong dynode chain; this is possible given the divergence of the light exiting from the fiber and the thickness of the entrance glass window that separates the fiber light emitting surface from the photocathode layer. To obtain a relative sturdiness with the planar geometry of the device this thickness cannot be reduced below ∼1 mm. It is worth to remember that the light exits a fiber with a highly diverging cone
- A photoelectron created in a region of the cell near the cell bound-

ary can be focused on the wrong first dynode; this depends on the shape of the electric field in the boundary region, which can only have a small component parallel to the photocathode plane

- Some of the electrons can be collected by the wrong dynode during multiplication, in a sort of leakage of a fraction of the whole charge to all nearby channels.

The last effect, which is usually referred to as "electrical" cross talk, gives rise to an electric signal much smaller (∼2% in charge for the H7546 tube) than the single photoelectron (p.e.) one and can be an issue only for calorimetry applications; on the other hand the first two processes, referred to as "optical" cross talk, produce a ∼1 p.e. signal that is totally indistinguishable from a true signal, so a wrong hit might be detected on the tracking system. The level of the optical cross talk depends on the geometry of the photocathode lighting; the datasheet values and the ones reported in Tab. 2.5 refer to a lighting from a 1 mm diameter round fiber placed in the center.

The photomultiplier multiplication process is very sensitive to the

.0011	.0054	.0013
.0068	1.0	.0080
.0011	.0056	.0012

Table 2.5: Optical cross talk measurements for the Hamamatsu H7546 photomultiplier, evaluated as the number of times a wrong cell is triggered with ∼0.5 p.e. normalized to the counts on the central cell, if the central cell is lighted with a 1 mm round fiber at the center, one photon at a time. From [46].

magnetic fields, so μ-metal shieldings are needed also if moderate fields are involved.

The Avalanche Photodiodes

The quantum efficiency of a PMT or of an image intensifier photocathode is smaller than 25% in the spectral region of interest. The higher quantum efficiency of a silicon photodiode could be helpful to detect the few photons collected by the fiber system, but the generated electron-hole pairs (one per photon) don't produce an electric signal strong enough.

The avalanche photodiode (APD) is a silicon photodiode that provides an intrinsic multiplication process of the electric signal. The photons are converted in the depletion region (Fig. 2.9), producing hole-electron pairs; the electrons drift to the high field multiplication region and start the avalanche process. The APD can be operated

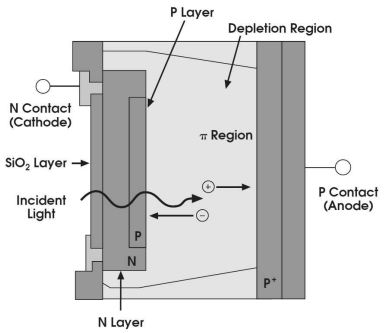

Figure 2.9: Scheme of an avalanche photodiode. The intrinsic region converts the light into hole-electron pairs, while the high field region at the n-p junction provides the multiplication stage.

in proportional mode or in Geiger mode; in the first case the gain is limited to a few hundreds, so an external low noise amplification system is needed. If the bias voltage is raised over the breakdown limit (usually $\sim$ 200 V) the device enters in the Geiger region; every electron that reaches the multiplication region starts a discharge current that lasts until the voltage drop on the bias resistor lowers the APD voltage below breakdown. The effective gain is given by the voltage drop and the capacitance of the APD junction and can easily reach $\sim 10^6$. In this case the passive quenching introduces a dead time of the order of tens of μs, that can be reduced with an active quenching scheme.
The dark count rate at room temperature is proportional to the device volume and, for the size needed for a fiber readout, it is too high given the long dead time of a Geiger mode APD. For this reason the Geiger mode APD has to be cooled down to $\sim$-50°C; in addition a light concentrator can be used to reduce the size of the detector and so the count rates [47].

On the other hand, the proportional APDs can in principle sustain a high count rate; anyway, cooling the APD enhances the gain of the detector, since the lower temperature reduces the number of phonons, and phonon interactions slow down the electrons during the avalanche process. At $\sim$-50°C the APD can be used, in proportional mode, for a scintillating fiber readout with a high detection efficiency [48][49]. A low noise VLSI electronics is still needed for further amplification, and this limits the timing properties of the detection system.
For the Geiger mode APDs the rise time of the signal can be short (e.g. 2 ns) since both the electron drift in the depletion region (with a speed of 5 $\frac{\text{ps}}{\mu\text{m}}$) and the avalanche development are fast processes.

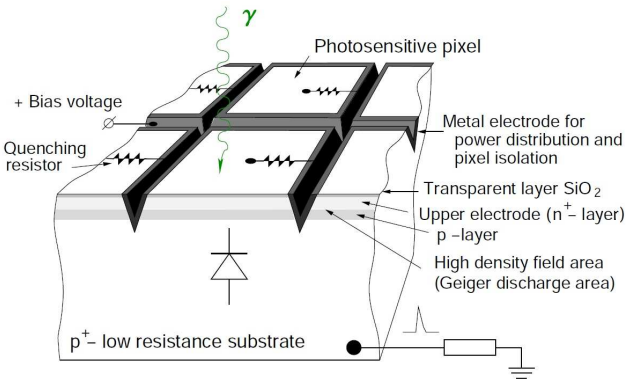

Figure 2.10: Scheme of a Silicon Photomultiplier. Each single cell is a scaled-down version of the APD of Fig. 2.9.

A cross talk can be present if arrays of Geiger mode APDs are used on the same substrate. During the avalanche, electrons with relatively high energy can be released and the subsequent electron thermalization generates optical photons that can travel to the nearby APD cells; this can be solved increasing the distance between the pixels, decreasing compactness.
APDs are not sensitive to magnetic fields and are rugged and compact devices.

The Silicon Photomultipliers

Silicon Photomultiplier (SiPM) is the common name of the Geiger mode multipixel avalanche photodiode, developed for the first time in 1999 by CPTA[2]. They are arrays of tiny (as small as 15×15 μm^2) Geiger mode avalanche photodiodes connected in parallel, with individual quenching resistors, so that the photodiode signal is the sum of all the fired pixels (Fig. 2.10) [50].
Since the cells are operated in Geiger mode, the amplitude of a single pixel signal does not depend on the number of collected photons in this pixel. Each pixel acts as a binary (on/off) device, but the multipixel photodiode as a whole unit is an analog detector with a dynamic range limited by the finite number of pixels of the detector itself. Typical silicon photomultipliers are manufactured with areas ranging from 0.5 mm^2 to 2 mm^2 and with a number of pixels in the range 200-2000 [51][52]. The probability for single photon detection (PDE) is the product of the quantum efficiency and the ratio between the effective area and the total area, which is limited by the dead

[2]Center of Perspective Technologies and Apparatus, Moscow.

space between neighbouring pixels. A PDE of 40% can be reached in optimized devices. The bias resistor ($\sim$10 MΩ) is normally grown in polysilicon and placed in the cell boundary; in practice it is the biggest limitation for the increase of the effective area. A possible solution is the use of a transparent high resistive layer for the bias. If this bias scheme is used the devices are also called Metal Resistive layer Semiconductor APDs, or MRS-APDs; anyway, the increase in the sensitive area is compensated by the light absorption in the resistive layer, with little or no increase in the PDE.
The dark count rate at room temperature is still very high ($\sim$1 MHz) but the advantage of the SiPMs with respect to the conventional APD is that, if the single photon sensitivity is not needed, it is possible to set the threshold at a higher level (e.g. 1.5 p.e.) with a big suppression of the dark count rate, since the dark counts of two cells are unlikely to be in coincidence.
The dead time of the single cell is given by the pixel capacitance charging constant through the bias resistor, which is in general of the order of a fraction of μs. Only the pixels involved in the avalanche processes are blind during this time, so the effective dead time can be much lower if the baseline shift can be handled.
The cross talk due to the photon production during the avalanche is still present at a 5% level [53]; the effect is a degradation of the linearity of the device and an increased dark count rate with a 1.5 p.e. threshold, but it is not an issue if the SiPMs are used for fiber readout.
Summarizing, the SiPMs may be the choice for the fiber tracking detectors of the next future, given the following figures:

- Overall PDE greater than 40%
- Sensitivity extended on a wide spectral range
- Time resolution better than 400 ns for single p.e. detection
- Low voltage operation ($\sim$ 40V), no cooling
- Insensitive to magnetic fields
- Compactness, when arrays of SiPMs will be available
- Low cost per channel.

The Visible Light Photon Counters (VLPC)

The VLPCs, developed by the Rockwell International Science Center, are silicon diodes designed to convert photons into many thousands of electrons with a high quantum efficiency exploiting an avalanche multiplication process [54][55]. A scheme of the device is shown in

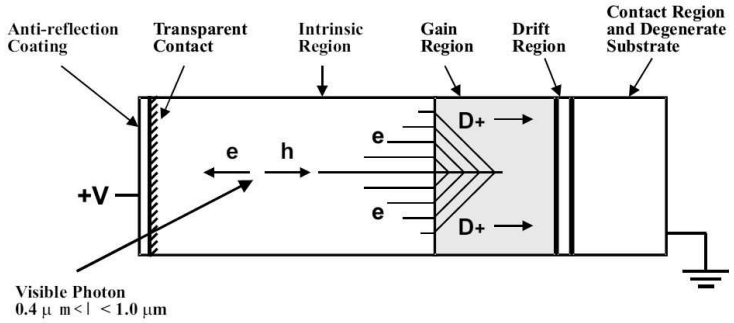

Figure 2.11: Scheme of the Visible Light Photon Counter detector. The whole thickness is less than 500 μm.

Fig. 2.11. The photon enters the VLPC through an antireflection coating and a transparent anode metalization, and creates an electron-hole pair across the standard valence-to-conduction band gap in the intrinsic (non-doped) zone. The hole drifts until it reaches the high field depletion region (Gain region in Fig. 2.11) where it collides with a neutral donor, freeing an electron which starts an avalanche by impact ionization. The gain region is doped with a high donor concentration (up to $10^{17}\mathrm{cm}^{-3}$), so that the Fermi level is situated only 50 meV below the conduction band; in this way the multiplication process is accomplished by only one type of carrier (the electrons) giving a very low gain dispersion and a good confinement of the avalanche itself. The avalanche process is self-limiting for space charge effects and the gain saturates at a few 10^4. If n photons hit the device at the same time, different avalanches are created, so that the total signal is n times the single photon one making the VLPC an almost ideal photon counter. In particular it can provide a very high quantum efficiency (up to 85% at 543 nm) over all the visible light spectrum [56]; further on, the avalanche develops and the signal is collected in a time as short as 4 ns, so VLPCs can offer the time resolution needed to fully exploit the timing properties of a fiber system [57].
Given the small gap between the impurity band and the conduction band in the multiplication region, VLPCs have to be operated at cryogenic temperatures as low as 6 K to avoid the thermal excitation of the impurities into the conduction band. Moreover the infrared background has to be strongly suppressed because the device is sensitive to a wavelength up to 30 μm.
VLPCs are manufactured in small arrays (4 by 2) of detectors of moderate large size (1 mm diameter) as shown in Fig. 2.12; 16 to 32 arrays are then enclosed in a single cassette providing the liquid Helium cryo-

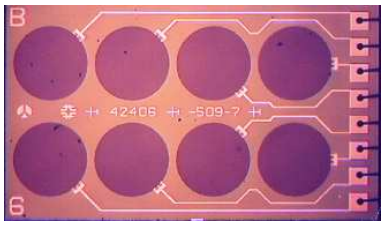

Figure 2.12: Close-up of a chip with a 2 by 4 VLPC array. The diameter of each detector is 1 mm.

genic system, a preamplifier array and the optical coupling to 128 or 256 fibers.
VLPCs can be operated in magnetic fields but are sensitive to radiation damage. For this reason and considering the clearances due to the cooling system, they are usually placed rather far from the detection zone; anyway the very high efficiency of VLPCs compensate for the light attenuation in the transport fibers.

2.2 Existing fiber trackers

In the following sections two large scale tracking applications of the scintillating fibers are presented:

- The UA2 Scintillating Fiber Detector, developed in the early '80s, which is the first application of the scintillating fiber technology to a collider
- The D0 Central Fiber Tracker, a tracking-triggering detector with 70000 channels representing the state of the art of the technology in the year 2000.

2.2.1 The UA2 fiber detector

The first important application of the scintillating fiber technology in tracking is the Scintillating Fiber Detector (SFD) of the UA2 experiment at the CERN SPS collider. The detector was used for the outer tracking and for the electron/π preshower identification [58][59][60].
It was composed of more than 60000 fibers of 1 mm diameter and $\sim$240 cm length arranged in a cylindrical geometry with a 41 cm mean radius. A total of 24 fiber layers was used, with 6 stereo triplets (angle 0, $\pm 15.8°$) before a 1.5 X_0 lead converter[3] and the remaining 2 stereo

[3]The radiation length X_0 is the mean distance over which a high energy electron loses a fraction $1 - \frac{1}{e}$ of its initial energy.

triplets (0, ±21.0°) placed after the lead for the preshower measurement (Fig. 2.13).
The scintillating fibers had a core of polystyrene, with a POPOP waveshifter and a polyvinylacetate single cladding, and a sputtered Aluminum layer acting as extra mural absorber. The fiber light was readout by 32 image intensifier + CCD modules. Since the detector was operated in no magnetic field, a 2 stage electrostatic focus, with a total demagnifying factor of 0.08, could be used, allowing the mapping of a large number of fibers in a single CCD chip. The system could be triggered at 100 kHz and readout at a maximum rate of 100 Hz.
The efficiency of the single fiber layer was found to be ∼91%, a good

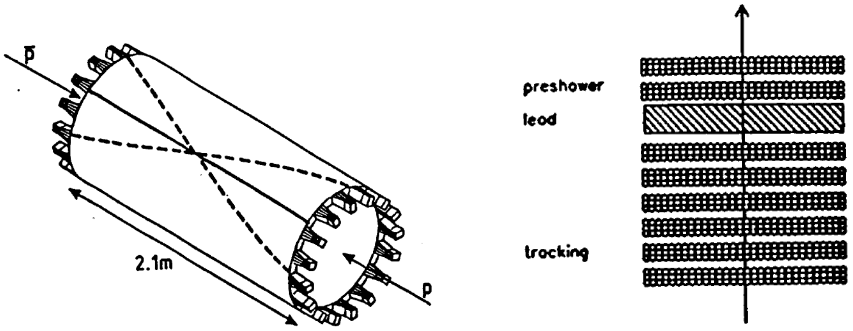

(a) (b)

Figure 2.13: (a) The geometry of the UA2 Scintillating Fiber Detector, with the 32 image intensifiers with CCD readout at both ends. (b) The 24 fiber layers crossed by a particle coming from the interaction point. From [40].

value considering this is a real single layer and not a fiber doublet ribbon. The resolution of the single layer is σ=350 μm (Fig. 2.14a), with a small degradation with respect to the binary resolution due to the presence of distorsions in the electrostatic focusing system that could induce cross talk [61]. Considering the 18 layers of the inner tracking altogether, a track efficiency of 96% was achieved, with a track resolution of σ=150 μm.
The preshower system allowed a clear separation between π and e considering the total pulse height of the fibers after the lead converter, as shown in Fig. 2.14b. For 40 GeV particles a π rejection factor of 15 could be obtained, with an electron detection efficiency of 98%.

2.2.2 The D0 Scintillating Fiber Central Tracker

A Central Fiber Tracking detector has been assembled as a part of the upgrade of the D0 experiment for the operation at Tevatron with

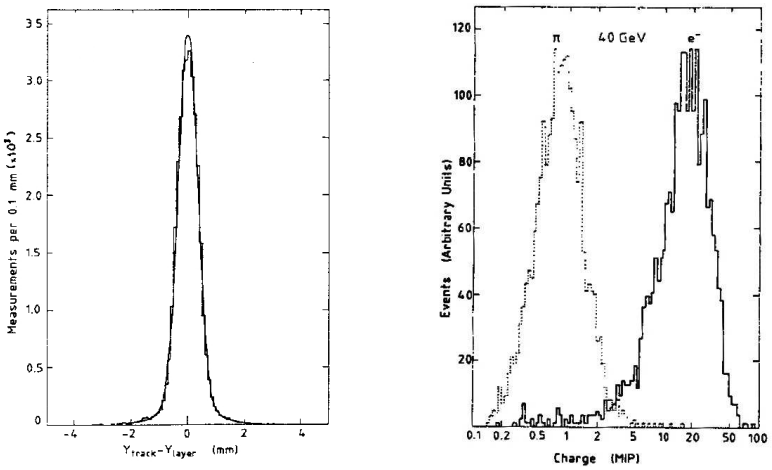

(a) (b)

Figure 2.14: (a) Single layer track residuals. Data are fitted with a gaussian with σ=350 μm. (b) The total pulse height (in m.i.p. units) collected by the preshower fiber layers for electrons and pions, at 40 GeV. From [61].

the new high luminosity Main Injector (Tevatron Run II, from 2002). With the increase in luminosity and with the reduction of the bunch crossing period with respect to Run I (from 3.5 μs to 132 ns), an extensive upgrade of the D0 detector was necessary.
For the calorimetry and the muon system a new frontend electronics with bunch tagging capabilities has been designed, while a completely new tracking system has been developed, focusing on the following points: momentum measurement with a 2T solenoid; large pseudorapidity[4] tracking coverage (η=$\pm$3); capability to extract a first level trigger; fast detector response and no dead time; radiation hardness [62][63].
The tracking system is composed of the inner Silicon Tracker and the outer Central Fiber Tracking detector (CFT) (Fig. 2.15). The CFT is made of 8 fiber superlayers, each one composed of 2 fiber doublet ribbons either with *zu* or *zv* orientations (the angle for the stereo layers *v,u* is $\pm$3°). Each doublet consists of two layers of 830 μm diameter multiclad fibers with 870 μm spacing (as in the right part of Fig. 2.2) and is held in place by a carbon fiber support.
The Kuraray SCSF-3HF fiber has been used, featuring a polystyrene core doped with 1.25% p-terphenyl and with 1500 ppm 3HF. This waveshifter, having a low self-absorption probability, increases the at-

[4]The pseudorapidity η is defined as $\eta = -\ln\left(\tan\left(\frac{\theta}{2}\right)\right)$ where θ is the angle between the particle track and the beam axis.

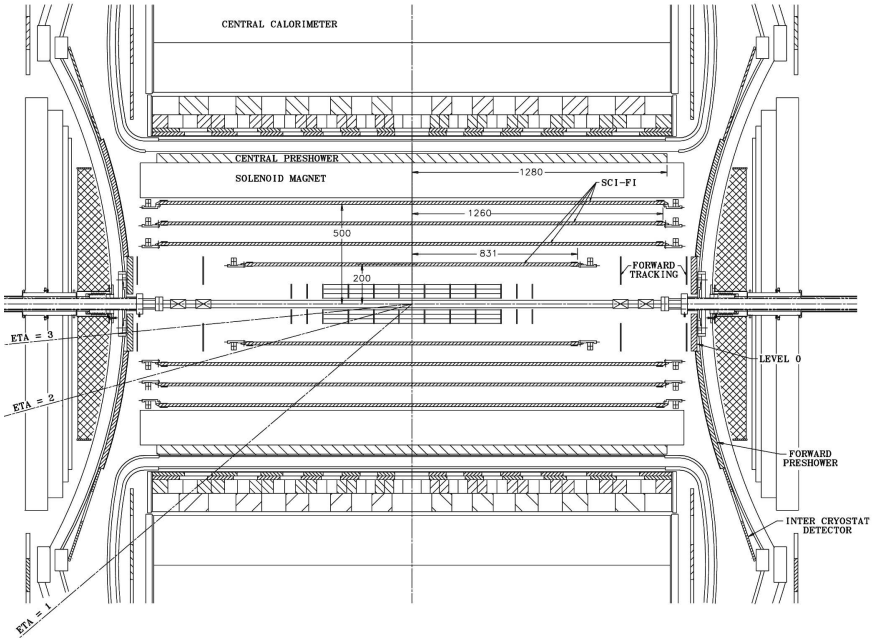

Figure 2.15: Overview of the D0 detector upgrade; 4 layers of the CFT, each one containing 2 superlayers, are referred as SCI-FI in the picture. From [62].

tenuation length λ_{att} up to 5.5 m, a fundamental characteristic, since the fibers are 1.7-2.5 m long.
The scintillating fibers are optically coupled to clear fiber waveguides $\sim$11 m long that carry the light to the photodetectors, placed outside the sensitive volume of the detector itself. This distance is comparable with the attenuation length of the clear fibers, which has been measured to be λ_{att}=10.5 m.
A VLPC array, which is kept at 7-9 K by a cryogenic system, allows to readout each fiber, for a total of 77000 channels. To minimize the light loss during the transport to the photodetector, the diameter of the clear fiber is intermediate between the scintillating fiber one (830 μm) and the VLPC one (1 mm); in this way the system is less sensitive to alignment errors.
Given the very high Q.E. of the VLPC detectors, the average number of photoelectrons collected by each fiber doublet is still high ($\sim$8.5 p.e., see Fig. 2.16a) allowing an efficiency greater than 99.9%. The spatial resolution of the doublet, as shown in Fig. 2.16b, is better than 100 μm in the ϕ direction. The signals from the $\sim$36000 axial fibers of the CFT detector are digitized and sent to a FPGA system in order to provide the trigger information; in less than 100 ns the system can compute a Level 1 trigger decision with a sharp threshold on the transverse

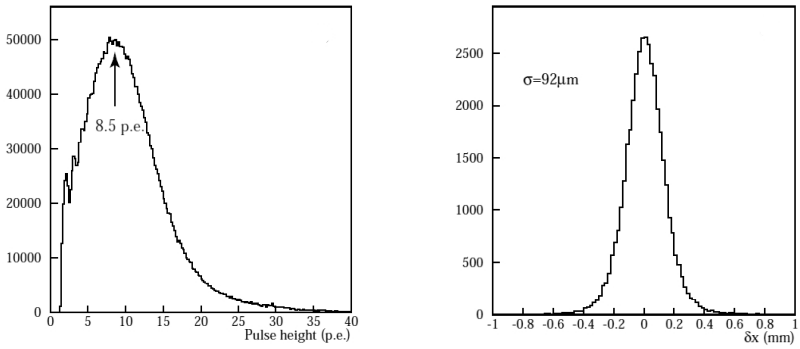

(a) (b)

Figure 2.16: (a) Pulse height collected by a D0 fiber doublet with VLPC readout; with a 0.5 p.e. threshold the efficiency is greater than 99.9%. (b) Residuals of the hit on the fiber doublet from the fitted track. A "digital" computation of the hit position has been used, assigning the fiber center in case of one hit and the mean point in case of two neighbouring hits. From [63].

momentum P_T (at around P_T=1.5 GeV/c), a high efficiency and a no dead area coverage [64][65].

Chapter 3

Detector design and simulation

Sec. 1.3 has described the importance of the antiproton cross section measurements and the requirements from the physics point of view. This Chapter translates these requirements in a real detector, that is the scintillating fiber tracker of the ASACUSA experiment. The different steps of the detector development are described focusing on the three main aspects of the tracker design:

- The different fiber and photomultiplier configurations, that have been tested and characterized to choose the optimal building block for the tracker
- The development of a custom frontend electronics and a dedicated DAQ system; a stereo prototype of the detector has been tested with the full electronics chain at the Frascati Beam Test Facility
- The definition of the detector geometry with the help of a montecarlo simulation.

The Chapter ends with a description of the final FAST detector.

3.1 Defining the detector module

The starting point for the detector module development is represented by the constraints given by the photodetectors, by the total volume to be covered by the tracker and by the cost limitation.

3.1.1 The photodetector

The choice of the photodetector has been almost straightforward: the need for a good time resolution with triggering capabilities and low dark counts limited the range to the multianode photomultipliers and the VLPCs. The VLPCs, whose cost per channel would be otherwise competitive, require the construction and the operation of an expensive 4 K cryogenic system.
The multianode photomultiplier featuring by far the lowest cost per channel ($\sim 30 \frac{\$}{\text{ch}}$) is the Hamamatsu R7600-M64 tube. It is a 12 stage 64 channel multianode photomultiplier, with a 2×2 mm^2 anode size (see Fig. 3.1) and a bialkali photocathode with a Q.E. greater than 20% in the 300÷500 nm range. The other specifications are listed in Tab. 3.1 and a picture of the device, from the photocathode side, is shown in Fig. 2.8. The R7600-M64 is endowed with an insulated plastic case with integrated voltage divider, which simplifies the PMT housing and the high voltage connections.

Anode size (mm^2)	2×2
Effective area (mm^2)	18.1×18.1
Spectral Range (nm)	300÷650
Peak wavelength (nm)	420
Q.E. at 390 nm	0.21
Window material	Borosilicate glass
Maximum HV (V)	-1000
Gain at -800 V	$3 \cdot 10^5$
Anode gain uniformity	1:2.5
Transit time (ns)	12.0
Transit time spread (ns)	0.38
Dark counts per ch. at 25 C° (Hz)	∼50

Table 3.1: Main properties of the R7600-M64 photomultipliers. The values are typical unless differently indicated (from datasheet). For the cross talk figure see Tab. 2.5.

3.1.2 The fibers and their layout

The sensitive volume of the detector is given primarily by the diameter of the vessel pipe: for a good containment of the beam tails, considering the multiple scattering on the target material, this has to be of the order of 10 cm in radius. As a result the inner radius of the tracker should be greater than 11 cm; given this value, the requirement on the solid angle sets a lower limit on the detector length, which in our case is of the order of 50 cm, for a total surface per layer greater than $2\pi \times 11 \times 50$ cm^2 $\sim$ 3500 cm^2. Moreover, 3 layers (2 stereo and 1

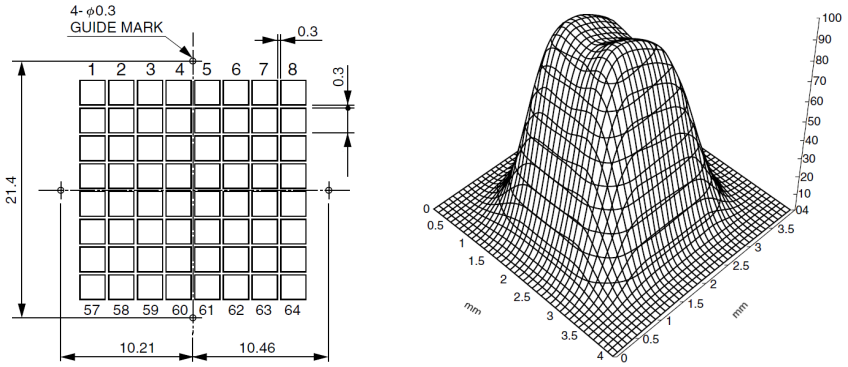

Figure 3.1: (a) The R7600-M64 anode placement and numbering. (b) Relative efficiency of a given anode as a function of the incoming light position. The center of the anode is in (2 mm, 2 mm). The efficiency is greater than 80% over a 1.6×1.6 mm^2 square. Since the anode spacing is 2.3 mm a small overlap is present (from H7546B datasheet).

axial, see Fig. 3.17a) should be used to identify a single hit in space with a good hit-ghost separation (in case of medium occupancy), so a minimum of 6 fiber layers is needed.
The fiber configuration has been selected to fully exploit the anode size, thus covering such a large area with a still limited number of channels. Following this criterium, two configurations have been investigated and tested [66]: one ø=2 mm fiber per anode, with a single layer placement, or four ø=1 mm fibers per anode, arranged in a doublet ribbon. In both cases the effective readout pitch is 2 mm, so the total number of channels remains the same. The goal of the tests was to measure the time resolution of the fiber+PMT system and, at the same time, to verify the detection efficiency.
A prototype with 16 fibers 50 cm long and with ø=2 mm, produced by PolHiTech[1], has been assembled with a Hamamatsu R7600-M16, a 16 channel multianode photomultiplier with specifications similar to the 64 channel version apart from a 10 times greater gain which allows a standard NIM electronics readout. The fibers have been wrapped with a white teflon tape (∼70 μm) acting as an extra mural absorber. The coupling and alignment between fibers and multianode pixels has been accomplished by a drilled rubber mask fixed to the PMT, with each hole diameter smaller than the fiber one.
The analog signals from the photomultiplier were digitized with a

[1]Pol.Hi.Tech. Srl S.P. Turanense km. 44,400 67061 Carsoli (AQ).

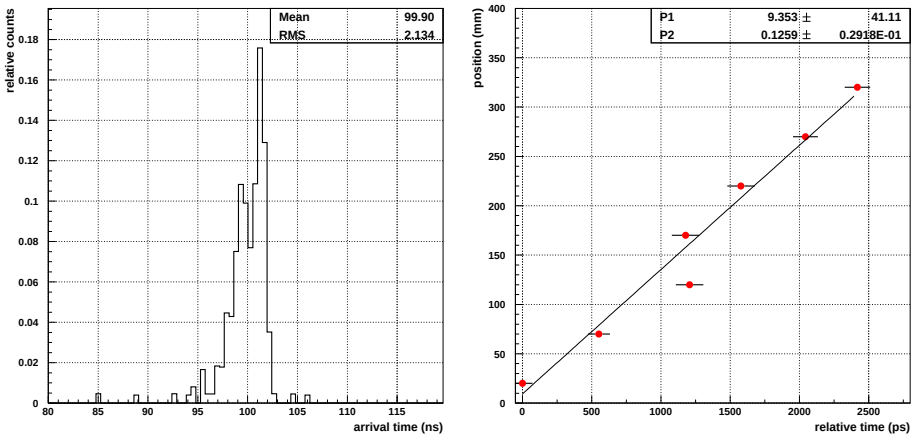

(a) (b)

Figure 3.2: (a) Distribution of the hit arrival times as measured by the TDC, showing a r.m.s. of 2.1 ns. (b) Source position as a function of the measured arrival time. The slope of the linear fit P2=12.6±0.3 cm/ns gives the propagation speed of light inside the fiber.

LeCroy 623A NIM discriminator (threshold 30 mV), converted to ECL and sent to a CAEN V775 (12 bit Time to Digital Converter with a 35 ps least significant bit (LSB) resolution). A PMT voltage of 950 V has been set for all the measurements described in this section.
A ^{60}Co source has been used for the time resolution measurement: it emits 2 synchronous photons (of 1.17 MeV and 1.33 MeV); one hits the fibers and the other a plastic scintillator, with a time resolution better than 500 ps, used as a timing reference. The TDC has been used in common stop mode, with the delayed scintillator acting as the stop signal. Different data samples have been taken moving the source on the fiber axis. The overall results, for all the fibers, are shown in Fig. 3.2a. The time resolution is of the order of 2 ns, well within the expected range. A linear fit of the position of the source as a function of the arrival time (Fig. 3.2b) gives the transmission speed of light in the fiber. The measured value (1.26×10^8 m/s) is lower than $c \times n^{-1}$ because of the multiple reflections the light undergoes during its path.

An efficiency measurement has been performed using cosmic rays; in this setup a tracking device was needed to select the particles that really were crossing the fibers.
A Silicon tracking system made of 4 planes (2 X-Y) of 9.5×9.5 cm^2 strip detectors [68] has been placed under the fiber prototype. The strip physical pitch is 121 μm and the readout pitch is 242 μm, for a total of 384 channels per plane (for a description of Silicon strip

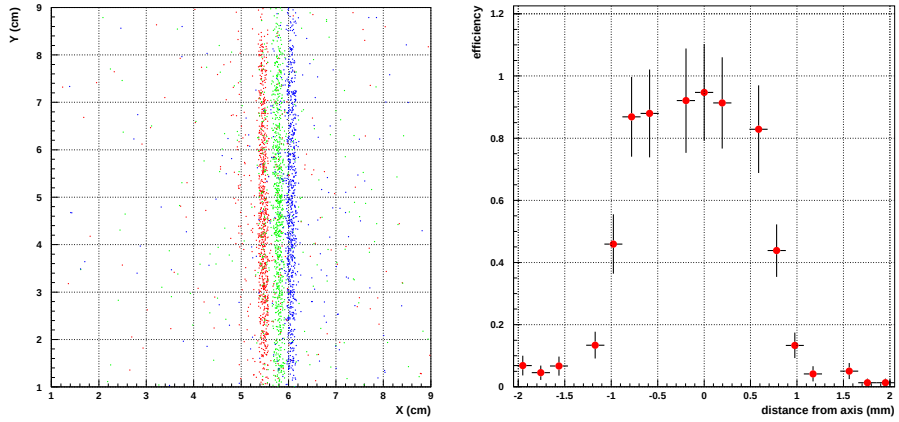

(a) (b)

Figure 3.3: (a) 2D profile of 3 scintillating fibers, as reconstructed by the Silicon tracking system. (b) Efficiency of one scintillating fiber as a function of the distance between the track and the fiber axis. It is computed as the fraction of the tracks reconstructed by the tracking system which are detected also by the fiber acquisition system.

detectors with capacitive charge division see [69][70]). A spatial resolution on the fiber plane better than 50 μm in both directions could be obtained with this system and the analysis methods described in [71].
The trigger signal was provided by a pair of 10×10 cm^2 plastic scintillators, positioned above the fiber module. The acquisition system was the same as the one used for the time resolution measurement, and a fiber was considered hit if its TDC signal was within a 30 ns window around the mean time value. More than 40000 events have been collected, corresponding to $\sim$ 1000 particles per fiber.
Fig. 3.3a shows the reconstructed image of a sample of 3 scintillating fibers; the hits out of the fiber region are errors in the track reconstruction (e.g. due to multiple scattering for the low energy particles) and negligible in number. The efficiency has been evaluated, averaging over thin ($\sim$200 μm) slices in the fiber axis direction, as the ratio between the number of tracks giving signals in the fiber channel and the total number of tracks in the slice. Fig. 3.3b shows the results for one fiber: in the central region the efficiency is nearly 100%, but, due to the low performance of the lateral regions, it falls down to an average value of $\sim$80% if the whole 2 mm diameter is considered.

This value of the efficiency is far too low: in fact a hit in space would be reconstructed with the 2 stereo and the axial layers with a $(0.8)^3$=50% efficiency, with only 2 layers in the $\sim$40% of cases and

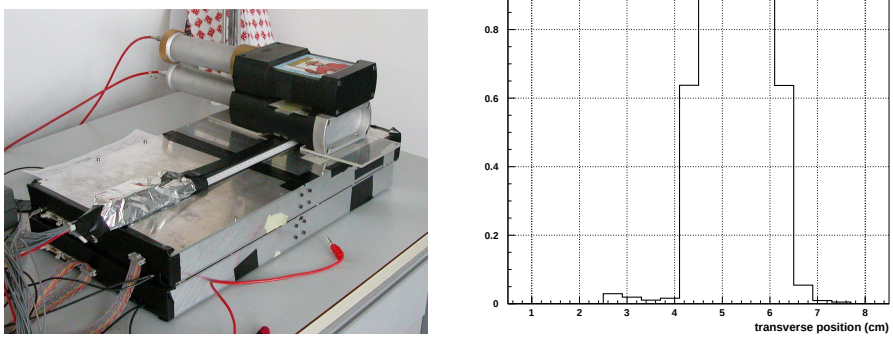

(a) (b)

Figure 3.4: (a) Experimental setup for the cosmic ray efficiency measurement: the ø=1 mm fiber prototype is placed between the scintillators used for the trigger and the Silicon detectors providing the tracking. These are enclosed in an Aluminum dark box. Apart from the fiber module, the setup was the same for the measurements with the ø=2 mm prototype. (b) Efficiency as a function of the transverse position on the fiber module. The average efficiency of the central region is greater than 99%. The module is ∼25 mm wide.

would have a probability of being missed greater than 12%.
For this reason the ø=2 mm fiber design has been rejected and further tests on the ø=1 mm fiber ribbon doublet configuration have been performed.
48 BCF-10 multiclad fibers 70 cm long have been glued, positioned as in Fig. 2.5, on a plastic support and sent, in groups of 4 fibers, to 12 channels of the R7600-M16 photomultiplier. As in the previous prototype, a teflon tape has been used as EMA. A time resolution measurement with the ^{60}Co source has been performed, obtaining a 2 ns r.m.s. resolution as in the ø=2 mm fiber case.
The efficiency evaluation has been performed with the cosmic ray setup shown in Fig. 3.4a. Since the fibers are grouped and could not be identified anymore, the efficiency has been computed averaging on the whole detector region. Fig. 3.4b shows a transverse efficiency profile, corresponding to a very high efficiency if the edge regions of the detector are excluded. A fit of the plateau gives a value of ∼99% for the efficiency.

3.2 The detector electronics

The electronics acquisition system has been developed with the following scheme:

- The analog signals from the multianode photomultipliers are amplified, shaped and discriminated
- The discriminated signals are sampled with a high frequency clock by a Field Programmable Gate Array (FPGA)
- The outcoming bits are stored on the local memory
- Once the memory is full, the FPGAs are sequentially readout, transferring the data, through the so called repeater boards, to the VME input/outputs (I/O) and finally to the personal computer.

In the next subsections the different stages of the signal processing are described in detail.

3.2.1 The frontend ASICs

Since the gain of the multianode photomultiplier is of the order of 10^5, a single photoelectron generates a pulse corresponding to an integrated charge of $\sim$10 fC; such a low value requires a device with a low noise amplification stage and a discriminator on the same die. The VA64TAP2.1, produced by IDEAS [2], is a 64 channel low noise ASIC, built in 0.35 μm N-well CMOS technology with a low gain preamplifier, a fast shaper, a tunable threshold discriminator and a parallel digital output.

The channel architecture is shown in Fig. 3.5: the output of the charge sensitive preamplifier feeds, through a pole zero cancellation filter (tunable by changing VPZ), the shaping amplifier, whose time constant can be adjusted in the $50 \div 70$ ns range acting on VFS.
The shaper output OS is filtered and feeds the comparator circuit; changing the trim DAC (one per channel) current i, it is possible to tune the reference voltage of the comparator to a value $V_{th} \pm Ri$ where V_{th} is the global threshold voltage and R=400 Ω. In other words, the 4 bit DAC can set, channel by channel, the comparator threshold in a $V_{th} \pm 7$ mV range.
The comparator output OC polarity can be reverted if negative signals (like the photomultiplier ones) are used. If the channel is not disabled the comparator output triggers a monostable circuit whose width can

[2] Gamma Medica - Ideas (Norway), http://www.ideas.no/

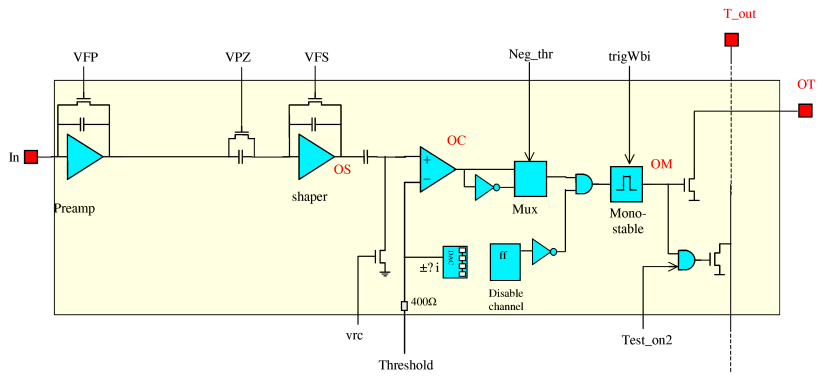

Figure 3.5: The single channel architecture of the VA64TAP2.1 ASIC (from datasheet). See text for a functional description and for the naming convention. The sample and hold circuitry is not shown.

be adjusted by trigWbi. The output of the monostable is sent to the output pad (OT) and, if the Test_{on2} signal enables the channel, to the T_{out} line, that is the wired OR of all the discriminated signals.
The shaper output OS feeds also a sample and hold circuit whose stored signal can be accessed by a demultiplexer: clocking the register that controls the demultiplexer the signals of the 64 channels appear one after the other at the differential analog outputs out_p and out_n. A global hold signal for all the channels has to be provided.
Most of the parameters of the VA64TAP2.1 are encoded in the configuration shift register that should be loaded in the device at any power-on or configuration change. In particular the register, which is 396 bit long, sets the trim DACs for all the channels (4 bit/ch), enables the digital outputs, decides if negative or positive signals are used, enables the test mode and routes the test signals to the desired channel.
In test mode a known electrical pulse can be sent to any channel, and both the analog signal OS (on the out_p and out_n pads) and the digital one can be investigated. A 65^{th} channel with no input pad is present for further testing purposes.
The most important ASIC specifications are listed in Tab. 3.2.
The sequential control inputs and outputs have been designed in such a way that different VA64TAPs can be connected in daisy chain, so that, in analog mode, all the ASICs of the chain can be readout one after the other. As far as the configuration registers are concerned, the last bit of the $(n-1)^{th}$ chip is connected to the first bit of the n^{th} chip, in order to have a single shift register $n \times 396$ bit long.
The parallel outputs of the VA64TAP2.1 are open-drain so they can't

Peaking time (ns)	50 ÷ 75
Lowest threshold (fC)	∼10
Noise level ENC, no load	440 e^-
Noise level ENC, 50 pF	2200 e^-
Maximum rate (MHz)	2.5
Gain after shaper stage (mV/fC)	∼11
Linear Range (fC)	-200 ÷ +160
Analog readout clock (MHz)	10
Trim DAC threshold range (mV)	-7 ÷ +7
VFS (mV)	700
VPZ (mV)	500
trigWbi (μA)	-4

Table 3.2: The main VA64TAP2.1 specifications (from datasheet and private comunications). Some of the working parameters are also listed.

feed a FPGA as they are. For this reason a level shifter ASIC, the LS64_2 by IDEAS, has been used to convert the signals to low voltage TTL (LV-TTL). The chip, with 64 inputs and 64 outputs, is quite simple requiring only the bias and no control signals for its operation. A close picture of the ASICs pair bonded to the board is shown in Fig. 3.6.

3.2.2 The frontend boards

The prototype

A prototype board has been designed and assembled to test the VA64-TAP2.1 connected to a R7600-M64 photomultiplier module and to verify the digital readout scheme of the ASIC by a FPGA. The board, shown in Fig. 3.7, is a FR4[3] Printed Circuit Board (PCB) housing a VA64TAP2.1 + LS64_2 pair and an Altera Cyclone 2 FPGA. The ASIC biases and control signals are provided by a 50 pin ERNI connector, while 8 input bits and 16 output bits for the FPGA control are routed, through LVDS drivers and receivers, to the scotchflex connectors interfacing the board to the readout system.
The bias for the digital part (1.2 V, 1.5 V and 3.3 V) is provided by a 10 pin scotchflex connector; a second 10 pin connector is needed for the JTAG[4] programming of the Cyclone 2 chip. A 10 MHz quartz is used as a clock reference for the FPGA.
The link to the photomultiplier is provided by four 26 pin ERNI con-

[3]Flame Resistant 4, a composite resin epoxy reinforced with a woven fiberglass mat, used in the production of PCBs.

[4]Joint Test Action Group, common name for the IEEE 1149.1 standard, a serial protocol to access a chain of integrated circuits on a printed circuit board.

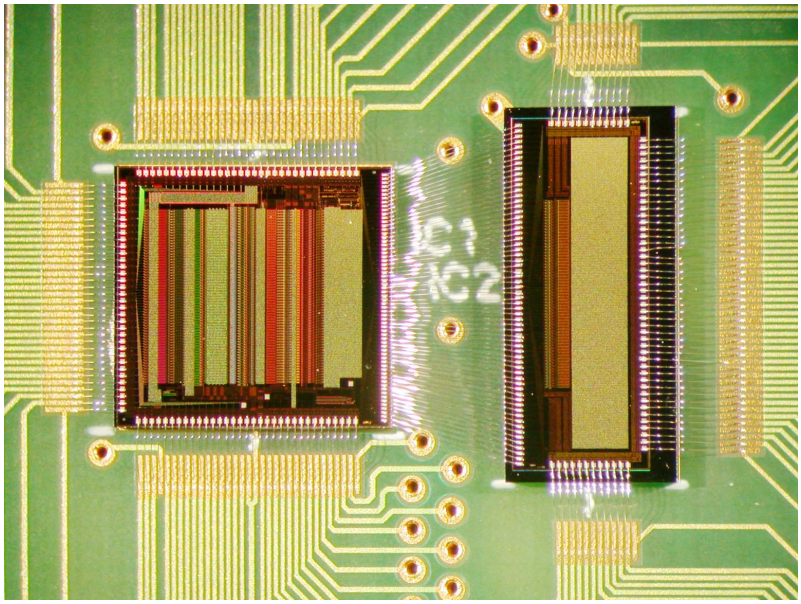

Figure 3.6: The VA64TAP2.1 (left) and the LS64_2 (right) bonded to the PCB with Aluminum wires. To match the different pitch between the VA output and the LS input pads a fan-shaped bonding was required.

nectors and some resistive and capacitive networks are inserted between these connectors and the inputs of the VA64TAP2.1: the tested networks included a direct link, a capacitive coupling with or without 50 Ω ground termination and a resistive network with -6 dB attenuation.

The FPGA is an Altera Cyclone 2 EP2C8Q208C7, whose specifications are listed in Tab. 3.3. The chip is a low power, low cost device with a ∼164 kbit on board RAM memory, which can store more than 2000 sampled bits per channel.

The two Phase-Locked Loops (PLLs) clock generators, with a maximum multiplier factor of 32, can provide (from the 10 MHz quartz on the PCB) the 320 MHz clock needed for the fast sampling. The number of Logic Elements (LEs) is much greater than the one needed to handle the sampling and readout logic.

The board assembly, from the ASIC gluing and bonding to the FPGA soldering, has been performed by Mipot[5].

The following steps have been undertaken to characterize the board, on both the analog and digital sections [67]:

- The bias networks have been tuned to set the ASIC currents to nominal values

[5]Mipot S.p.A. - Via Corona, 5 - 34071 Cormons (GORIZIA) - Italy.

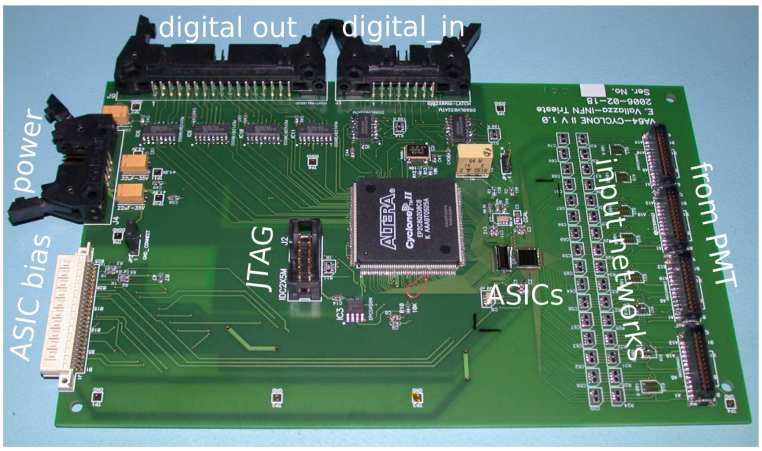

Figure 3.7: Picture of the first prototype VA64TAP2.1 board. The 2 ASICs can be seen at the low right corner of the Altera Cyclone 2. Different resistive and capacitive networks, connecting the VA64TAP2.1 inputs to the 4 ERNI connectors, can be mounted.

Number of Logic Elements	8256
Total RAM bits	166000
I/O pins	138
PLLs	2
Max. PLL multiplier	32
package	plastic quad flat pack
package pins	208

Table 3.3: The Altera Cyclone 2 EP2C8Q208C7 specifications (from datasheet).

- The configuration registers have been loaded, monitoring the effects on the chip behaviour
- The ASIC biases have been checked for different register configurations
- Using the ASIC in test mode, which allows to monitor the shaper analog output (OS) with an electric calibration pulse, the amplifier parameters have been tuned to minimize the peaking time and the undershoot
- The best resistive network has been chosen maximizing the S/N ratio with the analog readout and asynchronous hold (pedestal mode): since the direct link demonstrated to be the best solution, no more input networks have been used in the following production

- Several test designs have been implemented on the Cyclone 2 to check its functionality
- 64 scalers have been fitted on the FPGA to perform the threshold scans and verify the FPGA-LS64_2 comunication
- Threshold scans have been performed both with electric pulses on the calibration circuit and with light pulses hitting a PMT channel
- A sampling logic has been loaded on the Altera and tested with a delay unit
- The sampling logic has been used to measure the time resolution of a prototype fiber module with a cosmic ray run.

The most important results of the characterization procedure are described in the following subsections.

Noise and uniformity characterization

To evaluate the noise figure, different pedestal sets have been collected in different configurations. The pedestal, that is the baseline of the frontend and readout electronics, is obtained averaging a certain number (e.g. 200) of random trigger acquisitions. The noise is defined as the r.m.s. of the pedestal distribution and describes, in practice, the pedestal fluctuations.
An example of the pedestal distribution of a board connected with a biased photomultiplier is shown in Fig. 3.8a: the r.m.s. noise before and after the common mode subtraction is computed. The common mode is a global fluctuation of all the ASIC channels in the same direction, due to global events like bias noise or radio pick-up: the single channel total noise can be seen as an intrinsic noise plus the common mode contribution. In this case the two contributions are comparable in size.
A structure can be identified in the noise plot: the noise increases every 16 channels. The explanation for this effect has been found in the 26 pin ERNI cable connections towards the photomultiplier. Each cable transfers 16 signals, and the first and last channels are located on the cable edges, unscreened. The noise is still at a moderate level, so no possible solutions have been investigated.
Pedestal sets taken with different configurations allowed to extract the following information:

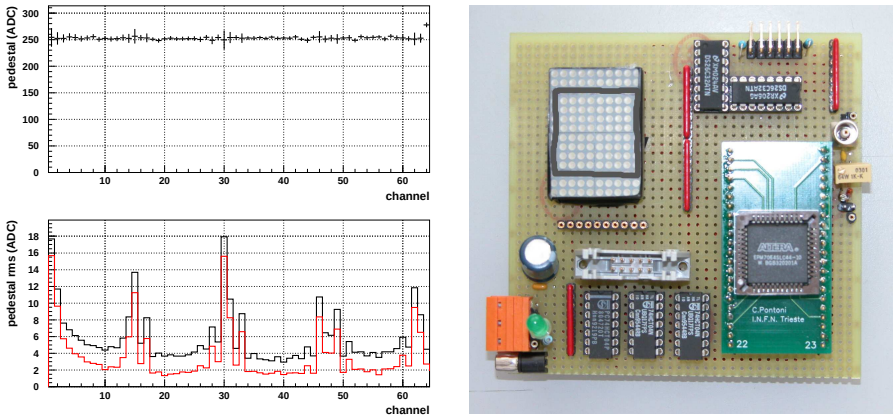

(a) (b)

Figure 3.8: (a) Example of pedestal plots, with the prototype board connected to the photomultiplier biased with 850 V. The upper plot shows the average pedestal value as a function of the channel number, the lower one shows the pedestal fluctuations before (black) and after (red) common mode subtraction. A region with higher noise can be identified at the edges of the 16 channels blocks corresponding to different ERNI cables. (b) The 8×8 led matrix used for the threshold scans. The Altera FPGA, controlled by a VME I/O, selects which led has to be used, while a pulsed signal on the lemo connector controls the lighting timing. The led spacing is 2.54 mm, so a pitch adapter (to 2.3 mm) built with 1 mm clear fibers is inserted between the led matrix and the PMT.

- The main contribution to the noise is given by the cables capacitance: with unconnected cables the noise falls well below 2 ADC (compare with Fig. 3.8a)
- The photomultiplier anode capacitance adds only a few percent contribution
- There is no dependence on the PMT voltage (i.e. gain).

The last statement is particularly important, since it means that, increasing the voltage, the S/N ratio can be arbitrarily increased. Anyway, the absolute value of the noise is small, so S/N ratios of the order of 10 (for 1 p.e. signals) are achievable with a PMT bias well under 700 V.
The led matrix of Fig. 3.8b has been used to test the digital section of the ASICs: a scaler array implemented on the FPGA counted the number of detected pulses as a function of the threshold voltage, lighting one channel after the other. The measurements have been repeated changing the photomultiplier voltage (Fig. 3.9a).
At a fixed PMT bias, for each channel the threshold at which the rate was half of the input one has been computed. The results are shown

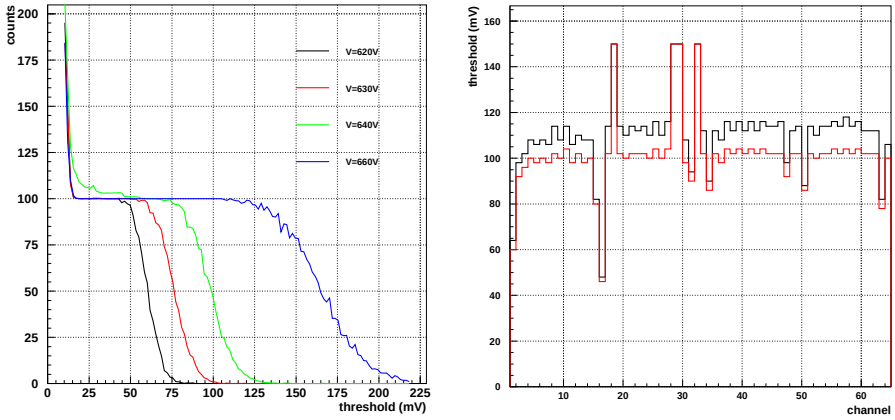

(a) (b)

Figure 3.9: (a) Threshold scans on one channel for different PMT biases. 100 led pulses were sent on the PMT anode. (b) Threshold levels at which the count rate is half of the nominal one, as a function of the ASIC channel. The red line refers to data collected with all the channels enabled, while for the black one, only the channel under test has been enabled. The PMT bias was 640 V.

in Fig. 3.9b, where fluctuations are dominated by the gain dispersion of the photomultiplier anodes.
To verify the presence of a digital cross talk at the ASIC level, the measurement has been done both enabling all the VA64TAP2.1 inputs and enabling only the probed channel, obtaining the 2 sets of Fig. 3.9b. The differences are within 10%, evidence of a low digital cross talk effect.

Time resolution of the digital sampler

A VHDL design to perform the readout scheme described in the following has been written and loaded on the Cyclone 2 chip. 128 RAM based 256 bit deep shift registers are created, so that each input channel from the LS64_2 is connected to two of them. Once in the idle condition, the FPGA waits for a trigger signal and when it receives it, the 320 MHz clock generated by the PLL is sent to 64 shift registers, to start the digital sampling. An opposite polarity clock is sent to the remaining 64 registers, so they can sample the same signals but with a half period time shift. In this way an effective sampling clock of 640 MHz is obtained, meaning a 1.57 ns LSB. The total sampling gate is 512×1.57 ns= 800 ns. Two more registers, which sample a digital input instead of the LS64_2 signals, are present for synchronization and debug purposes.
After 256 clock counts, the FPGA changes to the busy condition, dis-

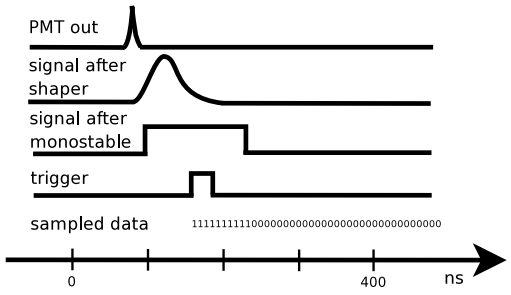

Figure 3.10: Time diagram for one hit channel, as seen by the FPGA: the trigger signal arrives after the fiber one, so only the falling edge of the monostable is detected. The number of sampled bits is not to scale.

abling the clocks of the registers and waiting for the transfer to the DAQ of the data stored in the registers themselves. Having 16 output bits, 4 read cycles (switched by 2 input bits) are needed to transfer the 64 channel data of one register position; then the registers are clocked and another position is accessed. The other 64 opposite clock registers are then read, and the data are interleaved via software.
During the busy phase the last bit of the register is connected to the first, closing the ring, so that data can be transferred an indefinite number of times. This is needed because all the boards receive, in broadcast, the same input signals, and, from the point of view of front-tend boards, there is no way to know which board is accessed: in practice, each board sends the data many times, but these data reach the VME I/O only once.
A reset signal, that can be sent at any time, sets the FPGA again in the idle state, waiting for the next trigger.
A fiber module 30 cm long has been assembled with Bicron BCF-10 1 mm in diameter fibers matched to a R7600-M64 tube, to perform a measurement of the time resolution in the digital sampling configuration. The signal from a 10×10 cm^2 plastic scintillator ($<$ 500 ps resolution) has been used as a trigger and timing reference, but, because of the delays in the level adapters, it reached the FPGA after the signals from the fiber module. So, the time jitters have been measured on the falling edge of the VA64TAP2.1 monostable circuits, as shown in the time diagram of Fig. 3.10. A PMT voltage of 880 V and a threshold of 140 mV have been used.
The results are shown in Fig. 3.11, where the distribution of the arrival times measured by the digital sampler has been fitted with a gaussian with σ=3.5 ns. This value is given by the square sum of three contributions:

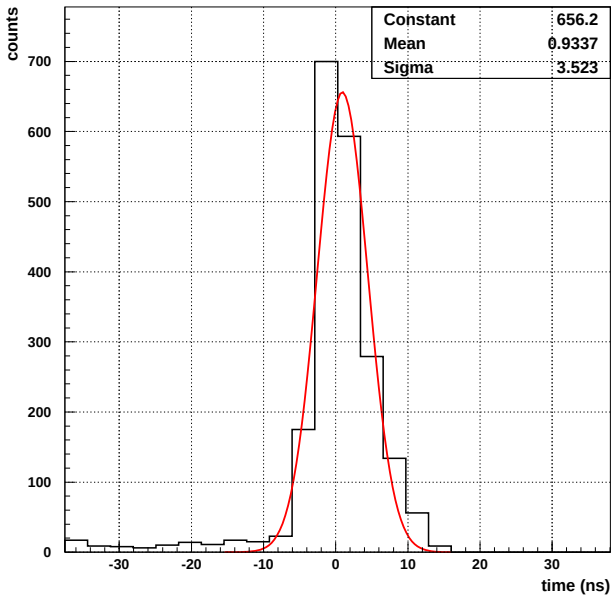

Figure 3.11: Arrival time distribution of the fiber hits as measured by the Altera FPGA, with a gaussian fit superimposed. An offset has been subtracted to center the distribution peak in zero.

- The intrinsic resolution of the fiber+PMT system, 2.1 ns as measured in Sec. 3.1.2
- The digital resolution of the sampler given by $\frac{1.57}{\sqrt{12}}$ ns=$\simeq$0.5 ns
- The error introduced, inside the VA64TAP2.1, by the constant level discrimination of a shaped signal (with a $\sim$50 ns constant) of variable amplitude.

Since the first two contributions are known, the last, which is the main one, can be evaluated to be $\sim$3 ns.

The final version

Thanks to the information collected during the prototype board tests, the final PCB has been designed.
It is a 125×230 mm^2 FR4 board which hosts, closely packed, two full frontend chains (Fig. 3.12a). A block diagram of the board is shown in Fig. 3.12b. The VA64TAP2.1s are connected in daisy chain, so a single 50 pin ERNI connector provides the bias and the control and allows the analog readout of both ASICs. The 2 FPGAs share the LVDS I/O connection with the rest of the DAQ system; both the 16 inputs and the 16 outputs are connected in parallel. To avoid conflicts, when an

output from one Altera is on, the outputs from the other must be in a high impedance state (tristate). The value of one of the input bits decides which device is sending the output, and a different design has to be loaded in the two FPGAs to accomplish this task. The Altera can be programmed both with the JTAG, useful for a fast debugging, and with the Active Serial method, that loads the design in a dedicated flash memory allowing a power on auto configuration.
The biases for the digital section are locally generated so that only a 3.3 V source has to be provided on the 10 pin scotchflex connector.

3.2.3 Post production board characterization

All the boards have been verified with the following procedure:

- Digital bias voltages and currents measurement
- FPGAs programming and verification test
- FPGAs functionality test with a simple loop-back design
- ASIC bias check, for digital and analog sections
- Test of the analog readout in pedestal mode, with and without ERNI cables connected
- Parallel outputs functionality verification, counting the noise triggers (with a very low V_{th}) on the FPGA scalers
- Dead channels identification
- Threshold scans for all the 128 channels of the board to compute the gain and offset figures. This procedure will be described in the following.

All the boards successfully passed the procedure, and the total number of dead channels is well under 10, for the complete production (that is 3200 channels).
The threshold scans have been a fundamental tool to check the behaviour uniformity of all the boards, given that thresholds have to be set in the final DAQ. Starting with the lowest threshold, a pulse, generated with a fixed voltage step on a 1 pF capacitor, has been injected into the channel through the on chip analog multiplexer. After one hundred pulses the scalers on the FPGA have been readout, the threshold has been increased and the operations repeated, obtaining a scan like the one in Fig. 3.13a. The data have been fitted with an error function, to measure the corresponding value, in DACs, of the injected pulse (that is the inflection point).

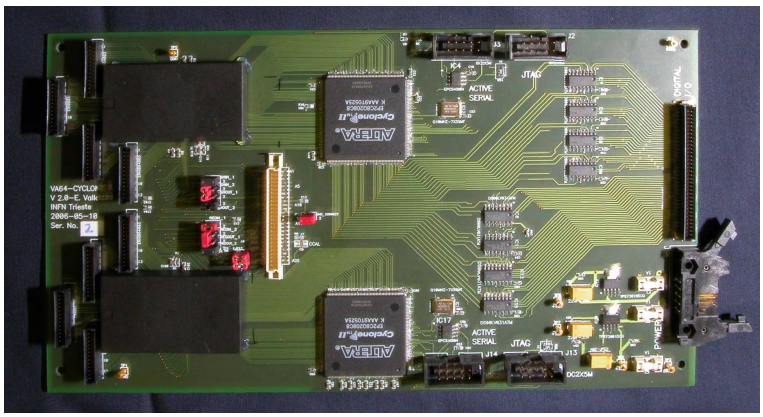

(a)

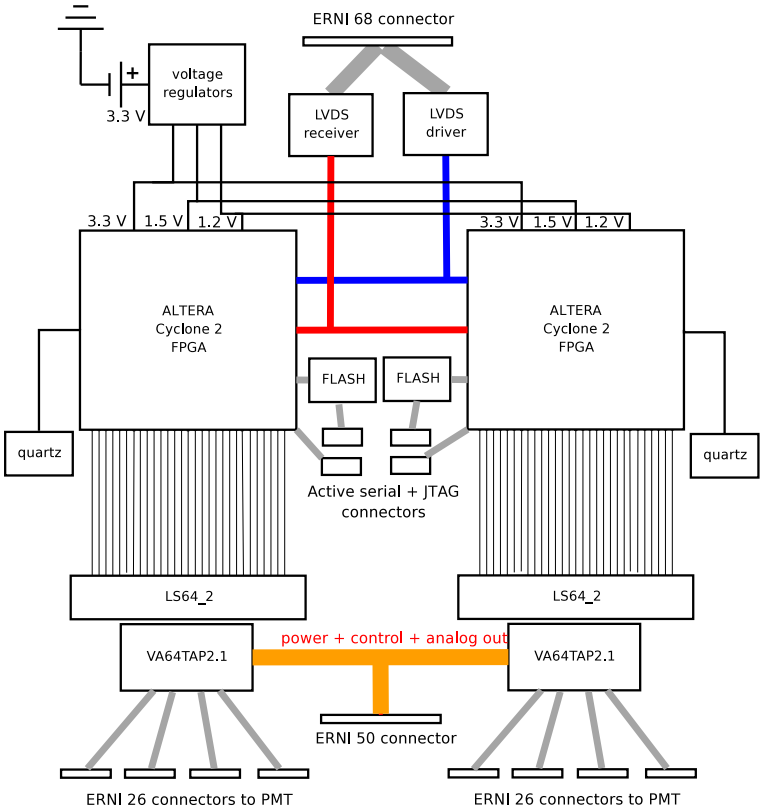

(b)

Figure 3.12: (a) The VA64TAP2.1 board, housing 2 VA64TAP2.1+LS64_2 ASICs and 2 FPGAs, can readout two multianode photomultipliers. The ASICs (under the black covers) are controlled and biased by the 50 pin ERNI connector, while the 64 pin ERNI connector handles the digital comunication with the two FPGAs. (b) Block diagram of the board itself.

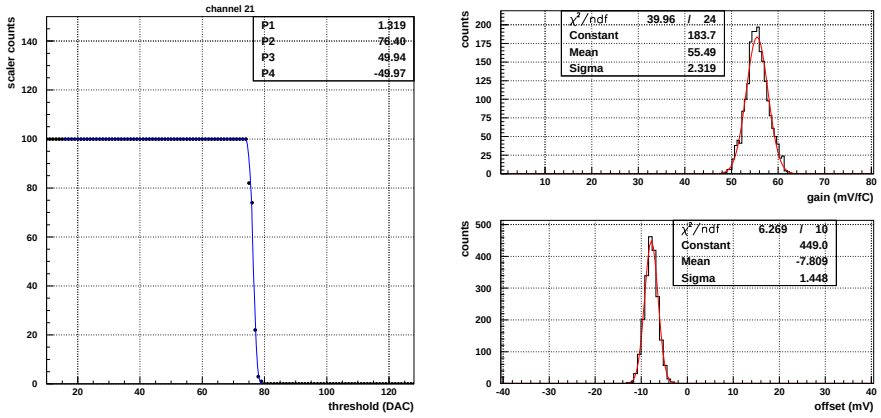

(a) (b)

Figure 3.13: (a) Example of a threshold scan for one channel, for an injected charge of 2.5 fC. The data have been fitted with a function $f(x) = erf\left(\frac{x - \mathrm{P2}}{\mathrm{P1}}\right)\cdot\mathrm{P4}+\mathrm{P3}$. One DAC corresponds to 1.71 mV. (b) Gain and offset distributions for all the 25 boards produced. The gain dispersion is σ=4.1%. Values are computed from the threshold scans as described in the text.

Scans with different voltage steps (1 mV, 2.5 mV and 3.5 mV) have been performed. A linear fit of the DAC pulse values as a function of the voltage step gives both the offset and the gain of the channel. Fig. 3.13b shows the distribution of these values over all the board production; to obtain a gain in mV/pC the voltage steps have been converted into the corresponding injected charge (multiplying for the capacitance) and the DAC values have been converted to voltages. The gain dispersion is within 4% r.m.s., and can be considered negligible with respect to the gain variations of the multianode photomultiplier; the offset values and their dispersions are also very low, of the order of 0.1 fC, a few percent of a 1 p.e. signal at a 800 V PMT bias.

3.2.4 The repeater boards

To handle the more than 20 frontend boards needed for the FAST detector, an intermediate board, called repeater board, placed between the frontend and the VME system has been developed and built. A single board, shown in Fig. 3.14, can control up to 6 frontend boards, performing the following tasks:

- It provides the biases and digital controls to the ASICs through the 50 pin ERNI cables. Most of the signals are broadcast to all the boards at the same time, while the configuration registers are serially loaded in one VA64TAP2.1 after the other

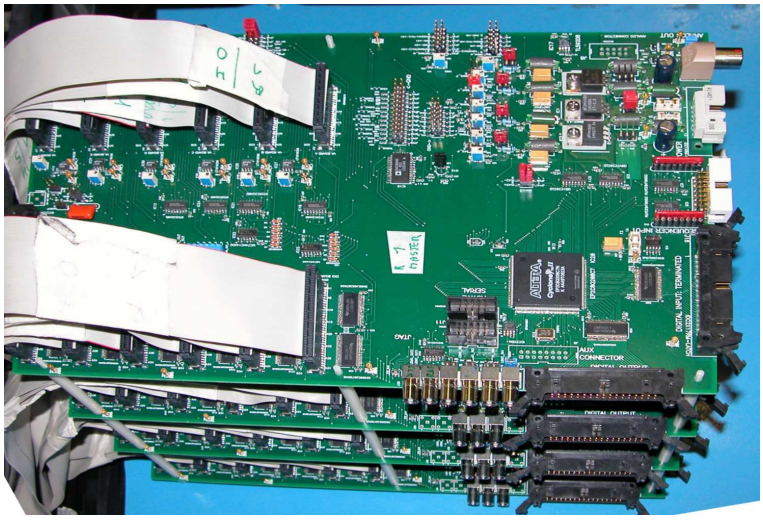

Figure 3.14: A stack of 4 repeater boards, that handles up to 24 frontend boards. The cabling toward the VME system is not present in the photo.

- It demultiplexes the differential analog signals from the frontend boards
- It amplifies the differential signals and routes the amplified signals to the VME flash ADC
- It sets the threshold voltages V_{th}, one per board
- It receives and discriminates the analog trigger signals, one per board
- It handles the comunication between the 12 frontend FPGAs and the VME I/Os, broadcasting the signals to the boards and demultiplexing the signals back from them
- It broadcasts the trigger and synchronization signals to the boards.

The digital data multiplexing and demultiplexing is performed by an Altera Cyclone 2 FPGA, which controls also the analog multiplexer for the analog readout mode and the DAC for the threshold selection. The FPGA is connected to a VME Input Output (INFN Trieste) with two 34 pin flat cables, while 4 lemo inputs are available for the trigger and synchronization signals.
The common control signals for the frontend ASICs are generated by a VME sequencer (INFN Trieste) and transmitted through a 16 pin scotchflex cable, that is shared between other boards if more than one repeater is used.

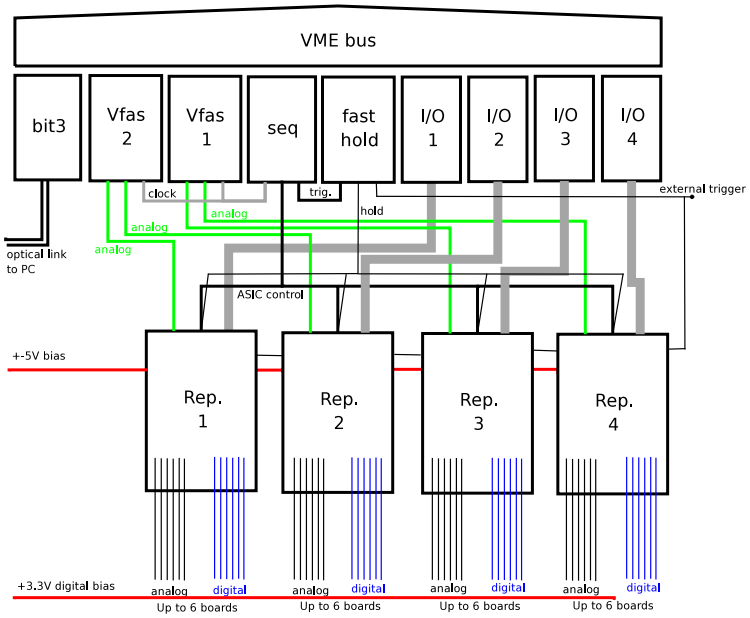

Figure 3.15: Connection scheme for the complete DAQ chain.

The board generates the biases for the ASICs and for the frontend FPGAs (starting from ±5 V inputs), thus simplifying the biasing scheme. More than 250 digital input output connections are present on each board; this has been made possible by the use of 16 channel TSSOP[6] drivers and receivers with integrated termination resistors, and by the extensive use of surface mounting (SMT) components.

3.2.5 Completing the DAQ system

This section describes the complete DAQ system both from the analog and digital point of view. Fig. 3.15 shows the connection scheme of the DAQ for the whole FAST tracker.

The VME sequencer is connected to the four repeaters in parallel, with a 16 pin flat cable, that provides the control signals for the ASICs, such as the reset signal and the readout clock. In analog mode, after a trigger signal has been received, the board sends 768 clock counts (at a maximum rate of 5 MHz) to the repeater, which forwards the first 128 to the 1st frontend board, the second 128 to the 2nd one and so on, and connects the differential output of the right board to the flash ADC. The sequencer provides also a NIM clock signal for the flash ADC; the delay between the ASIC clock and the ADC one can

[6]Thin-Shrink Small Outline Package, a package standard with a 0.65 mm pin pitch.

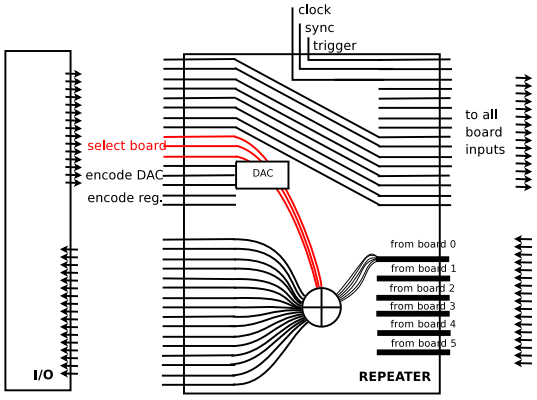

Figure 3.16: Diagram of the I/O–FPGA via repeater board comunication. The working principle is explained in the text.

be fine tuned to compensate the delay due to the cables. Moreover, the sequencer can generate a random trigger signal for the pedestal acquisition. During a digital run this board is inactive.
The fast hold board is a modified Input Output board (INFN Trieste) that, if not busy, generates a hold signal immediately after it receives a trigger. The board is polled by the DAQ software to detect an event occurrence, and needs a software reset to recover from the busy state after a trigger. This board is needed, in analog mode, to avoid that a hold signal is sent before the full system is ready to accept data. For a digital run the hold output is inhibited, and the board is only used by the software to detect an event. For the pedestal acquisition the random trigger generated by the sequencer is used as an input by the fast hold board. The hold signal is sent to the repeaters with a custom 16 pin scotchflex cable shared with the sequencer.

Two dual channel 12 bit flash ADCs are used to sample the analog signals. A differential lemo cable connects each repeater board to its slot on the ADC. Both Caen V550 and VFAS[7] ADCs have been used. Each repeater is connected to a VME Input Output board by two 34 pin flat cables; since LVDS signals are used, 16 bits are available for the input and 16 for the output (Fig. 3.16). The first 8 bits of the repeater input are used to encode the ASIC registers (2 bits), to set the DAC threshold values (3 bits) and to select the frontend board to be read (3 bits, for a $0 \div 5$ range). The last 8 bits are broadcast to the frontend board as they are, and they are used during the data transfer procedure. The output of the repeater is directly connected to the input of the selected frontend board. A copy of the trigger signal is

[7]Developed by LEPSI, Strasbourg.

sent to the lemo input of the 4 repeaters, so it can be forwarded to the frontend FPGAs; synchronization signals can be sent to the FPGAs in the same way. A SBS[8] Bit3 620 VME to PCI optical link allows the comunication between the VME system and the data acquisition PC.
The system can sustain with no dead time a trigger rate higher than 3 kHz in analog mode and higher than 1 Hz in digital mode, where more than 1.5 Mbit of data are collected for each trigger.
A mixed analog and digital readout can be performed: anyway, since the hold signal freezes the input of the comparator of the VA64TAP2.1, no more digital hits will appear after the hold is sent. For this reason this mixed mode is only useful with physics events well defined in time (e.g. cosmic rays) and for debug purposes.

3.3 Test of a stereo prototype at the Beam Test Facility

A fiber module prototype with a single multianode photomultiplier has been built and tested on an electron beam at the Beam Test Facility (BTF) of the INFN Frascati National Laboratories [72]. The goal was to study the performances of a fiber module as close as possible to the final tracker building block readout by the final electronics.

3.3.1 The prototype and the beam line

The 64 channels of the PMT have been divided into 16 channels for the longitudinal fibers and 24 channels for each of the stereo ($\pm 20°$) layers, obtaining a fiducial area of 144×32 mm^2, as shown in Fig. 3.17. The fibers (ø=1 mm Bicron BCF-10 with multicladding and white EMA) have been glued on a 5 mm PVC support starting from the axial layer and the total thickness of the detector is 6 mm.

The mask for the alignment of the fibers with the multianode photomultiplier is shown in Fig. 3.18a. It is a 3 mm thick iron foil with a grid of 2×2 mm^2 square holes obtained by electrophoresis and it is identical to the ones used for the whole tracker. The PMT has been connected to a frontend board and to a repeater board, thus assembling a small scale version of the DAQ system described in Sec. 3.2.5: both the analog and digital readouts were possible.
The Beam Test Facility is a positron/electron beam line with tunable energy (30÷750 MeV) and multiplicity. The beam, from the high

[8]SBS Technologies, Inc., US, http://www.sbs.com

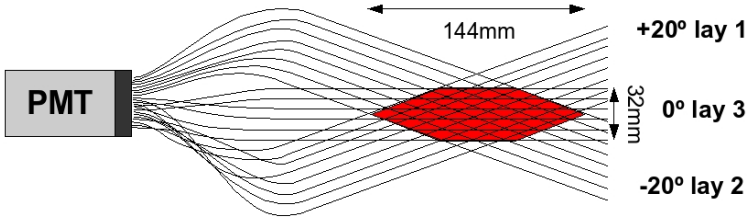

(a)

(b)

Figure 3.17: (a) Schematic view of the prototype, with the fiducial area (highlighted), that is the area covered by all the layers. The total length of the fibers is ∼70 cm. (b) Picture of the prototype before its enclosure in a light tight envelope. The mechanical support of the PMT is visible on the left, while the sensitive area is on the far right.

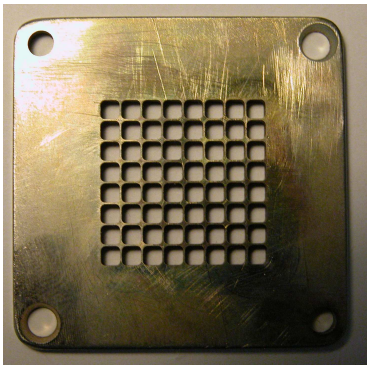

(a)

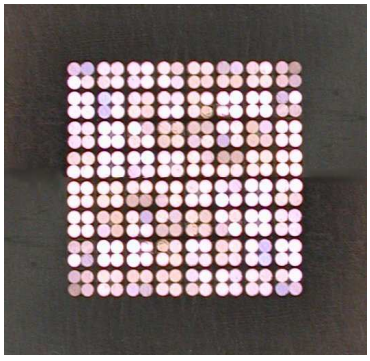

(b)

Figure 3.18: (a) The iron mask for the fiber-PMT alignment. The holes, which are 2×2 mm^2 in size, are produced by electrophoresis. The spacing between 2 channels is slightly larger than 0.2 mm. (b) Detail of the same mask after the fibers have been inserted, glued, cut and polished. The fibers are enlightened from the side, so the differences in light emission is due to the fiber position in space.

current linac serving the DAΦNE e^+e^- collider, is steered, at 50 Hz, against a W target; the set of (tunable) magnets and collimators of the extraction line collects, from the particles of the shower, the ones within a given energy window and takes them into the user area. Other collimators can be used to reduce the beam intensity obtaining a one particle multiplicity and a beam spot size of a few mm (r.m.s.).
The module has been placed on the beam after a Silicon strip tracking system identical to the one described in Sec. 3.1.2.
The trigger was provided by the linac itself and a delay unit allowed a fine tuning of the delay.

3.3.2 Results of the stereo prototype beam test

The events with only one single particle detected in all the 4 layers of the Silicon detector have been selected and, among these events, the tracks which were crossing the active region of the fiber module have been chosen. For this subset of events the following analysis has been performed on the fiber analog data:

- The pedestal values have been subtracted, channel by channel, from the raw data, obtaining the pulse height value in ADC units
- The channels with a pulse height value 20 times greater than their pedestal r.m.s. noise were selected, as shown in Fig. 3.19a; this is the so called pull cut, being the pull defined as the ratio between the pulse height and the r.m.s. noise of the channel with the maximum signal in the event
- The channels with a pulse height greater than 400 ADC (pulse height cut) were added to the selected ones; this avoids inefficiencies that would occur in case of very noisy channels, where 20 times the r.m.s. noise is comparable with the ADC dynamic range (see Fig. 3.19b). The two cuts (pull and pulse height) have been selected trying to obtain a smooth beam profile plot (Fig. 3.20b)
- All the fibers corresponding to the selected channels have been used for the reconstruction.

The efficiency ϵ_n of each layer can be evaluated directly from the plots in Fig. 3.20a, representing the number of hit fibers per event, for the three layers. An inefficiency occurs when zero fibers are hit, so the following efficiencies can be computed: ϵ_1=92.9%, ϵ_2=84.4% and ϵ_3=91.7% (for layer numbering see Fig. 3.17a).
The lower efficiency of layer 2 can be explained with the bad placement

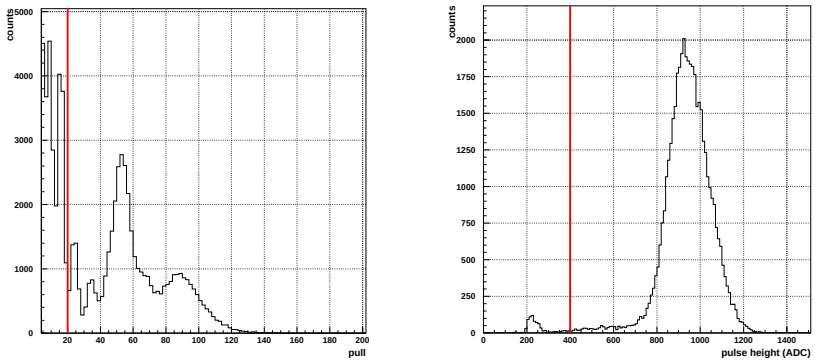

(a) (b)

Figure 3.19: (a) Pull distribution for the fiber prototype, with a 850 V bias: the pull is defined as the ratio between the pulse height and the r.m.s. noise and it is evaluated, event by event, for the channel with the maximum signal. (b) Pulse height distribution for the same events and channels. In both plots the cuts used for the fiber selection are shown with red lines.

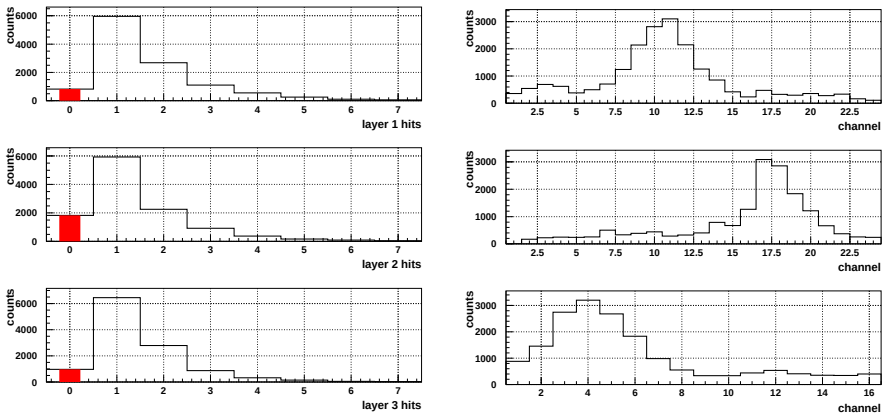

(a) (b)

Figure 3.20: (a) Distributions of the number of hits per layer. When 0 fibers are detected (in red) an inefficiency has occurred. High multiplicity can happen if the electron starts a shower in the detector volume. (b) Beam profile plots on the three detector layers.

of at least 8 fibers at the PMT–fiber interface, as a visual inspection after the beam test has shown. It is worth to note that the ratio between one hit and two hit events ($\sim 40\%$) is mainly due to the fiber doublet ribbon geometry and the 4 fiber–1 PMT channel readout (that would account for 33%).

A particle that crosses the three layers generates a signal, neglecting the inefficiencies, on three or more fiber quartets. With the approxi-

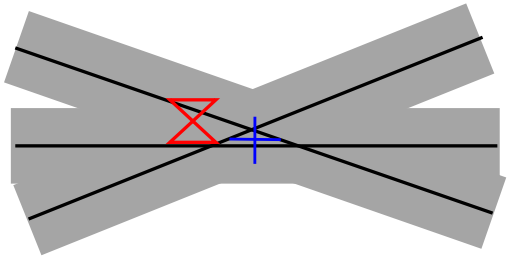

Figure 3.21: When a particle crosses the detector plane in the position indicated by the red marks, three channels, corresponding to the grey fiber quartets in figure, detect a signal. The three axes of the quartets, in black, identify a triangle, whose barycenter (blue cross) is the reconstructed hit position. If more than 3 fibers are above threshold, the smallest among all the reconstructed triangles is chosen.

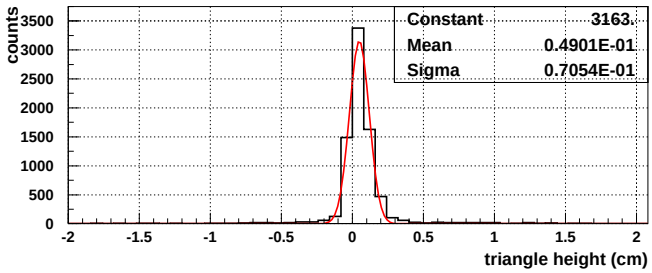

Figure 3.22: Distribution of the heights of the smallest reconstructed triangle, with a gaussian fit superimposed. The sigma of the gaussian, σ=0.71 mm, is well within the 2 mm width of the single channel.

mate assumption that the fiber quartets lay on the same plane (which is not the case since the three layers are positioned one above the other) their three axes identify a triangle, as shown in Fig. 3.21. Once the hit fibers have been selected, to extract the transit position the following operations have been performed:

- All the triangles formed by any fiber combination have been considered
- For each triangle the height has been computed; since all the triangles are similar (with angles 20°, 20° and 140°), the height can be used to estimate the quality of the reconstruction
- The triangle with the minimum height is selected (Fig. 3.22 shows the resulting height distribution), and the transit point is computed as the triangle centre of gravity.

Only events with at least one hit on each layer have been used: this reduces the sample to 70% of the total. Anyway, this fraction would

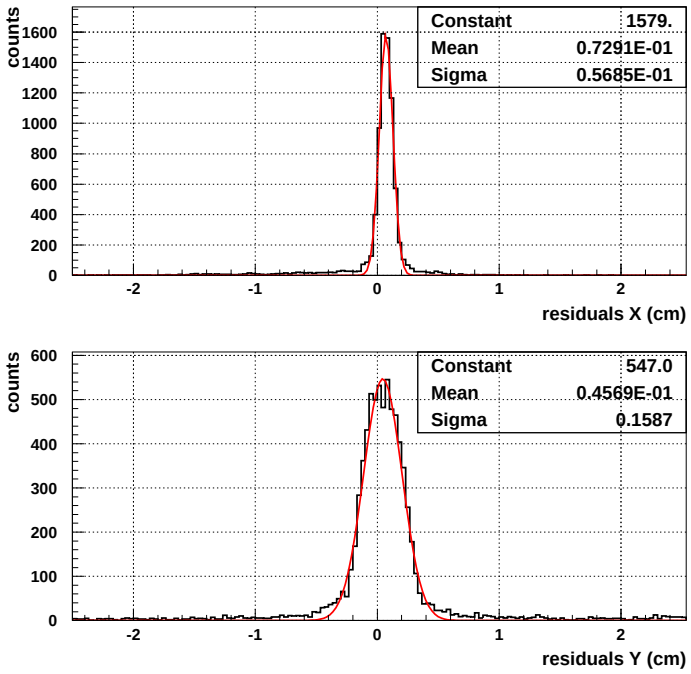

Figure 3.23: Prototype residuals from the Silicon detector tracks, in both directions, fitted with a gaussian curve. The σ for the x residual is in perfect agreement with the expected value for a digital detector with a pitch $p = 2$ mm, that is $\sigma_x = \frac{p}{\sqrt{12}}$=0.58 mm. The theoretical relation $\sigma_y = \frac{\sigma_x}{\tan 20^\circ}$ is also verified (with a <1% error).

have been much greater if the efficiency ϵ_2 of layer 2 were as high as those of the other layers.
To evaluate the spatial resolution the residuals have to be computed. They are defined as the distance between the Silicon strip detector track projected on the fiber module and the transit point as reconstructed by the fiber module itself. The sigma of the gaussian fit, shown in Fig. 3.23, is the spatial resolution of the prototype: the experimental values (σ_x=0.57 mm, σ_y=1.59 mm) are in very good agreement with the theoretical expectations (σ_x=0.58 mm, σ_y=1.59 mm).
Summarizing, the results on the prototype tests at the Frascati Beam Test Facility have demonstrated the feasibility of a $\pm 20^\circ$–0° stereo fiber detector with 2 mm pitch and the good performance of the readout electronics.

3.4 The FAST detector

With the results of the work previously reported, all the building blocks of the detector have been defined, and the constraints that they introduce well understood, allowing to complete the design of the scintillating fiber detector and to verify it with the montecarlo simulation.
Even if, from a chronological point of view, the simulation took place before the construction, these two items are described the other way round to let the details be understood.

3.4.1 The tracker assembly

The FAST tracker consists of nearly 10^4 scintillating fibers of different lengths organized in 2 axial and 4 stereo layers, assembled on 2 cylindrical shells (an inner and an outer one). The supports of the shells are two cylinders of plexiglass: the inner one is 3.4 mm thick and has an external radius of 115 mm and a length of 50 cm while the outer one, with a radius of 150 mm and the same length, is 4.4 mm thick.
The assembly phase of the FAST detector has required several steps:

- Fiber bundles, with 16 fibers each, have been assembled with the help of the tools shown in Fig. 3.24a. Bicron BCF-10 fibers (ø=1 mm) with multicladding and white EMA, the same of the stereo prototype, have been used
- The inner shell has been mounted on a flange to allow the support rotation and the needed stiffness (Fig. 3.24b)
- Following the 20° reference marking lines drawn on the cylinder, the bundles have been stuck, with the help of glue and bi-adhesive tape, to the cylinder surface
- Once one layer had been completed (see Fig. 3.25a), another layer of tape fixed it, and a transparent polycarbon layer 250 μm thick was used to prepare a smooth surface for the next layer to be placed
- After the 3 layers of the inner shell had been placed, a black tape has been used to increase the mechanical resistance of the ensemble and to provide a screening for the ambient light
- The complete procedure was repeated for the outer shell.

In Tab. 3.4 the most important geometrical parameters of the 6 fiber layers are summarized. The values have been measured during and after the layers assembly. A sketch of the (sliced) FAST detector is

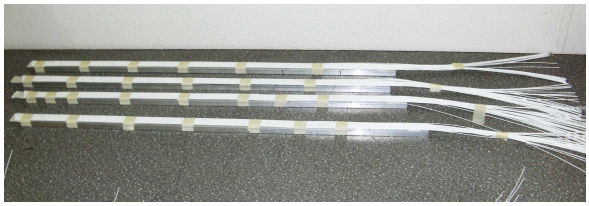

(a)

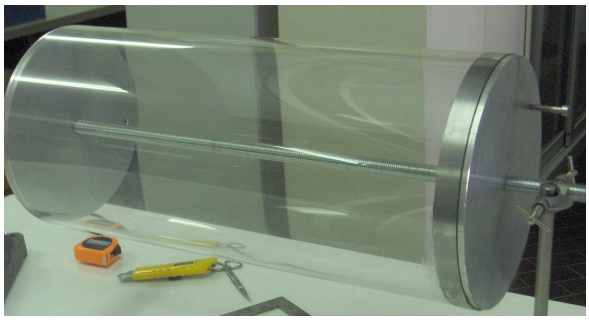

(b)

Figure 3.24: (a) Fibers have been glued, with the help of correctly shaped iron rods, in bundles made of 16 fibers each that have been then positioned and fixed on the cylindrical support. (b) The 3.4 mm thick plexiglass cylinder used as the inner shell support for the fiber placement. A second bigger one has been used for the outer shell.

represented in Fig. 3.26.

The two shells have been inserted in the Aluminum mechanical

Shell	Layer	mean radius (mm)	stereo angle	α	number of ch.
1	1	117.9	+20°	88.4°	333.5
	2	121.7	-20°	-85.5°	344.5
	3	125.5	0°	0°	377
2	4	151.8	0°	0°	460.5
	5	155.6	+20°	66.8°	436.5
	6	159.5	-20°	-65.2°	451

Table 3.4: Geometrical parameters of the six fiber layers. The angle α is the one covered by the single fiber path in the ϕ projection. A positive stereo angle identifies a right-handed screw. Each channel is made of 4 fibers, so that the 0.5 value in the total number of channels corresponds to 2 remaining fibers. The number of electronics channels is rounded to the next integer.

frame of Fig. 3.25b: it is a rectangular box with two 80×70 cm^2 faces (12 mm thick) and 75 cm long, and with 42 holes to house the PMT–fiber alignment masks in the front face. The box is 10 cm larger than the outer layer radius, to allow a future upgrade of the detector with

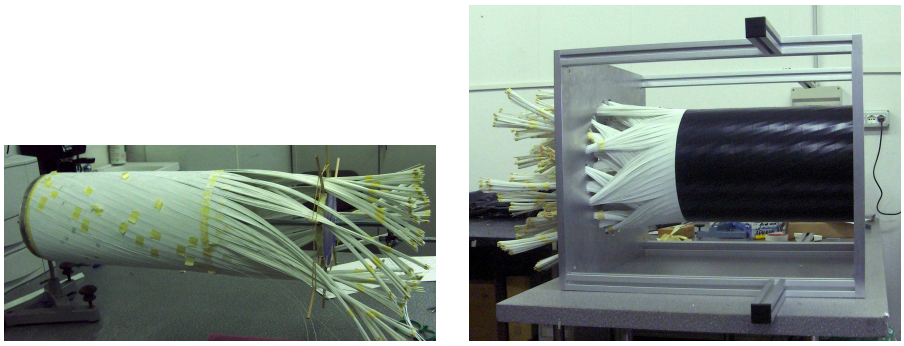

(a) (b)

Figure 3.25: (a) The innermost stereo layer soon after completion, before the polycarbon layer placement. The second layer is positioned directly on top of it. (b) The 6 completed layers, inserted in the mechanical box. The black tape delimits the area of the detector capable of coherent tracking; outside this region the fiber position is not known. The lateral panels are not in place.

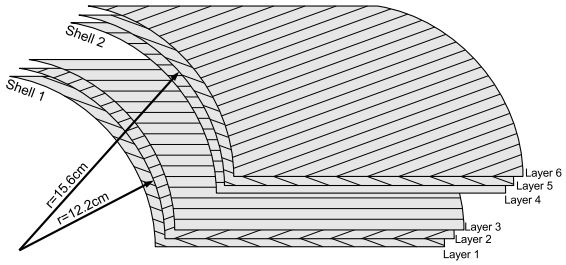

Figure 3.26: An exploded view of a slice of the FAST detector, with its 6 layers. The direction of the fibers is indicated.

an external layer. The front and back faces are light tight while four removable panels avoid the light to enter from the detector side.

All the fibers have been inserted in the alignment masks, they have been glued and the masks have been screwed to the detector front face (see Fig. 3.27a). The mechanical constraints on the fiber bending allowed an ordered fiber insertion only for a subset of the PMTs; for the others, the fibers have been inserted in the only possible way from the mechanical point of view, so that 42 maps have been created to extract the fiber number information from the position on the PMT. Once the masks were fixed on the support (a bi-component epoxy glue has been used), the fibers have been cut with a diamond fly cutter, then leveled with sandpaper and polished with abrasive powder.
After this operation was concluded, the photomultiplier support has

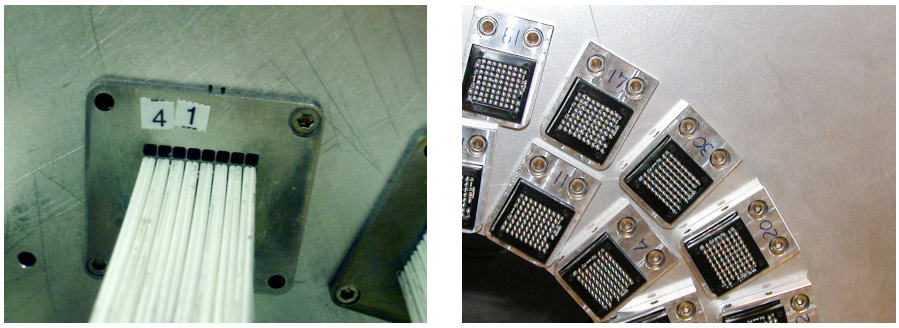

(a) (b)

Figure 3.27: (a) The fibers soon after the insertion in the alignment mask. Afterwards they were glued, cut, smoothed to the mask level and polished. Since the total number of fibers is not a multiple of 64, empty holes are sometimes present in the masks. (b) Detail of the PMT support plate with the screwed PMT holders allowing the alignment with the fiber mask. The PMT backsides with the anode pins are visible.

been put in place. It is a 2 cm thick Aluminum plate, to which 42 PMT holders are screwed. As shown in Fig. 3.27b, the screw system cannot drive the movement like in a micrometric positioning system but is only designed to keep or release the holder. So each holder should be manually moved in the right position and there fixed.
To simplify the alignment, a dummy PMT has been built: it is a box with the PMT dimensions, no backside and an empty alignment mask in place of the front face. When it is inserted in the holder the mask with the scintillating fibers can be seen under the empty mask, and the holder can be moved until the two masks are aligned. Then the holder is fixed and the dummy PMT replaced with a real one. An estimated positioning precision of $50 \div 75$ μm can be obtained in this way.
After this last step the FAST detector (see Fig. 3.28) was completed and prepared for the integration with its electronics, which will be described in Sec. 4.1 and in Sec. 4.2.

3.4.2 Montecarlo simulation of the detector

The montecarlo (MC) simulation of the tracker has been a fundamental benchmark to validate the geometrical properties of the scintillating fiber detector design.
In particular the goal of the MC simulation was to evaluate the vertex reconstruction efficiency and the resolution of the FAST detector, as well as the dependence of these parameters on the position of the

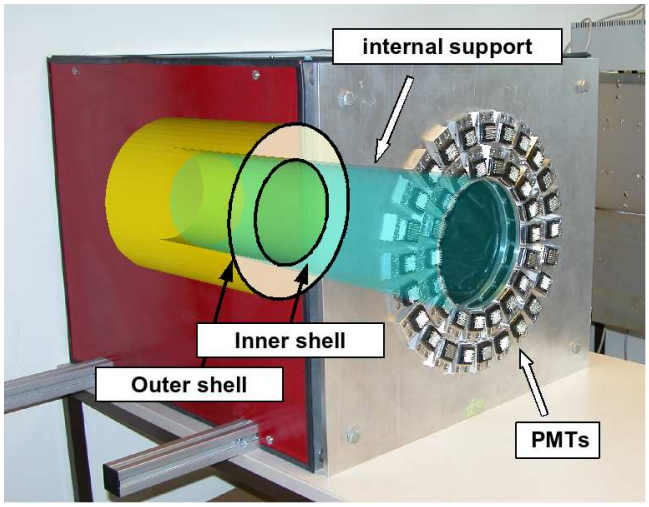

Figure 3.28: View of the assembled FAST scintillating fiber tracker.

vertices inside the sensitive volume.
The montecarlo simulation has been developed in GEANT 3.2.1 [73]. Since a simulation at the single fiber level was too heavy and beyond the goal of the investigation, the geometry of the detector has been sketched in the following way: each fiber layer has been simulated with a uniform cylindrical shell of plastic scintillator with a thickness of 1.57 mm, that is equal to the average thickness of a fiber doublet ribbon. The approximation is accurate from the point of view of the multiple scattering effects and of the radiation matter interactions and provides all the needed information for the efficiency and resolution studies. Moreover, the fibers which gave signal could be analytically computed from the hit (r,ϕ) positions on the layer itself, thus allowing to test the hit reconstruction capabilities of the stereo geometry.
A 3 mm thick Aluminum vessel with a 10 cm radius is also present, as well as all the plastic material needed for the scintillating fiber support; the thicknesses of these plastic layers are equal to those effectively used in the detector assembly. On the other side, the region where the scintillating fibers are no more aligned because of the bending towards the photomultipliers is not described by the simulation.
Since the focus was on the detector performances, the whole antiproton beam line has not been simulated in this phase; on the contrary the antiprotons have been generated, with a negligible momentum, inside a Hydrogen filled pipe with a 10 cm radius positioned on the detector axis. In this way they annihilate only a few μm around the generation position but, since the Hydrogen pressure is kept very low (a fraction of mbar), the trajectories of the pions are not influenced.

The geometrical reconstruction efficiency has been evaluated count-

Number of emitted charged π			2	4	6
Percentage			49.7%	47.9%	2.4%
Number of detected tracks	$\leq$1	2	3	4	$\geq$5
Percentage	14.0%	37.4%	16.5%	19.5%	1%

Table 3.5: Number of charged mesons emitted from the $\bar{p}$–H annihilation and detected by all the 6 layers of the tracker.

ing the number of times in which at least 2 charged pions crossed both shells of the tracker with respect to the total number of annihilations. For example, Tab. 3.5 classifies the annihilation events with the number of detected tracks, for annihilations in the center of the detector: in this case a geometrical reconstruction efficiency of 86% was measured.
To verify the dependence on the annihilation position, two scans have been performed: one on the detector axis and the other along one radius at z=0 (symmetry plane of the detector). The results for both the r and z efficiency scans, for 50000 generated $\bar{p}$s each, are shown in Fig. 3.29: the efficiency in the central region is greater than 80% while it decreases to slightly less than 50% at the detector edge, in good agreement with geometrical considerations. As far as the r dependence is concerned, little or no degradation in the efficiency appears when moving far from the detector axis. To compute the spatial resolution, three main contributions to the position error have to be taken into account:

- The multiple scattering effect, which causes a deviation of the particles from a straight trajectory: this effect is automatically taken into account by the GEANT software
- The intrinsic resolution of the $\pm 20°$–$0°$ stereo detector as measured during the prototype beam test presented in Sec. 3.3.2. This effect can be reproduced adding to each point used for the vertex reconstruction a value extracted with a gaussian probability distribution
- The parallax error due to the fact that the particles cross three thick layers with a non zero angle with respect to the normal direction, while during the reconstruction the three layers are considered to be on the same cylindrical surface.

The last component can be estimated *a priori* considering the triangle height distribution, since in case of consistent parallax errors the heights of the triangles used to find the hit position would increase.

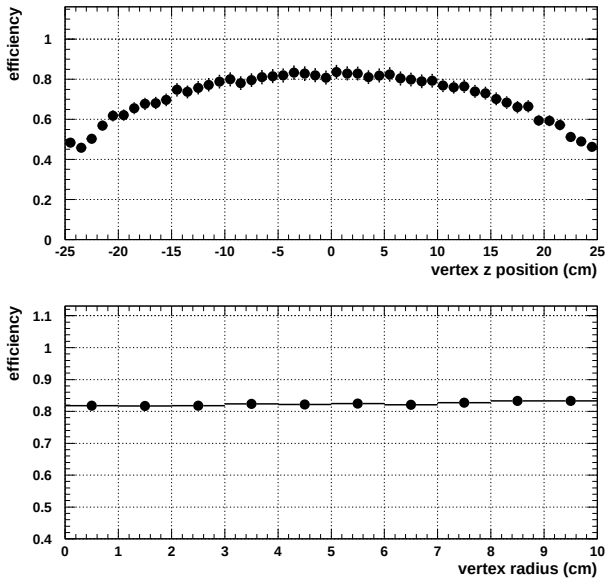

Figure 3.29: Vertex reconstruction efficiency evaluated in several points along the detector axis (top) and changing the radius on the z=0 plane (bottom).

The distribution, shown in Fig. 3.30, is larger than the corresponding one for the prototype (1.13 mm vs. 0.71 mm r.m.s.), measured during the beam test with a low divergence beam perpendicular to the module. Since the parallax errors are not negligible, a procedure that automatically takes into account this effect has to be used:

- A subset of the events in which *only* two tracks release energy in all the 6 layers of the detector has been selected. This has the great advantage that the reconstruction can be analytical, i.e. results are independent on the used algorithm; on the other side, this slightly underestimates the spatial resolution
- For each track the crossing points (x,y,z) of the 6 detector layers have been computed
- For each point the corresponding fiber channel with signal is extracted: at this point, for each track, six n_i, with $i = 1, 6$, channel numbers are available
- For each shell the hit position is computed from the hit channels, with a procedure similar to the one used for the stereo prototype (see Fig. 3.21): each channel is described by a function ϕ(z), so the three channels of the shell identify a triangle in a ϕ-z plane, from which the mean z and ϕ can be extracted. The (x,y,z) coordinates are computed projecting the (ϕ,z) ones on a cylinder

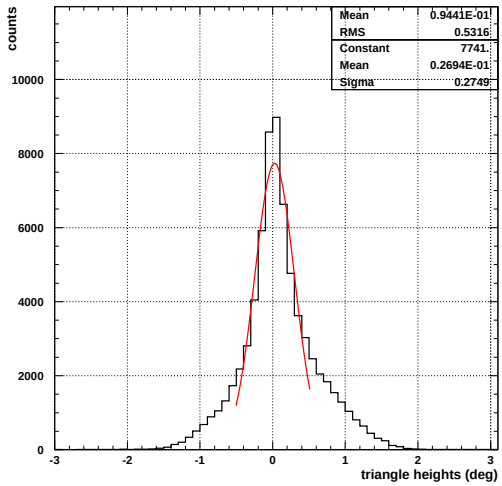

Figure 3.30: Distribution of the height of the triangles used to select the cross position, for the inner layer. The x axis is expressed in ϕ units, with one degree corresponding to 2.09 mm on the circumference. The core of the function can be fitted with a gaussian curve with $\sigma = 0.275°$, corresponding to 0.58 mm, but non gaussian tails are present. These tails increase the r.m.s. value to 1.13 mm (0.53°). As a comparison, the same distribution for the stereo prototype test had $\sigma = 0.71$ mm (see Fig. 3.22).

with a radius equal to the average radius of the three layers of the shell. This introduces the parallax error into the simulation

- Each (x,y,z) point in space has been spread along the ϕ and z directions using two gaussian probability functions (no spread has been inserted for the r coordinate) with the sigma equal to those measured during the prototype beam test
- Once the four final points have been found, the two lines connecting them have been (analytically) computed: the lines are skew lines, which almost intersect in the vertex region. So, the mean point of the distance-segment of the two lines has been considered as the reconstructed vertex.

The distribution of the residuals computed using the reconstructed vertices and the real annihilation positions are shown, both for the z direction and for a radial one, in Fig. 3.31. The effects of the multiple scattering on the resolution can be evaluated if the residuals are computed with the gaussian spreading of the hit points turned off. In this case the resolutions, as shown in Fig. 3.32, become $\sigma_x = 2.0$ mm and $\sigma_z = 1.5$ mm (to be compared with σ_z=10.4 mm and σ_x=6.6 mm of Fig. 3.31). It can be concluded that multiple scattering effects are a negligible contribution to the detector resolution in the FAST case,

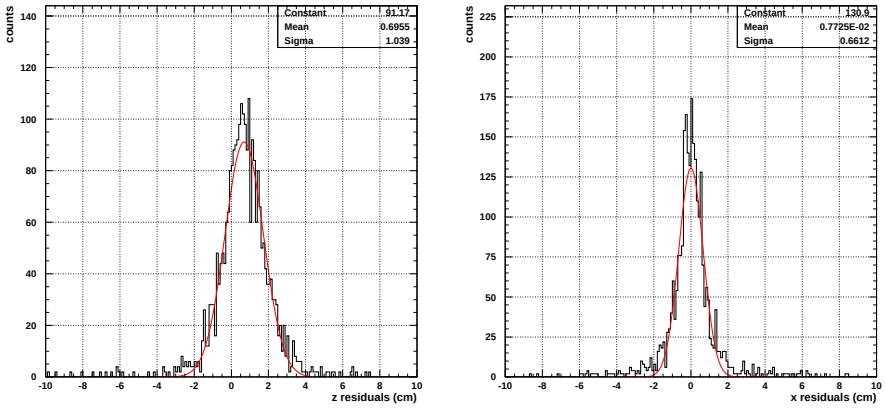

(a) (b)

Figure 3.31: (a) Residuals in the z direction, evaluated in the center of the detector. (b) Residuals in the x direction, for the same position. A fit with a gaussian curve allows to compute the vertex resolution values: σ_z=10.4 mm and σ_x=6.6 mm.

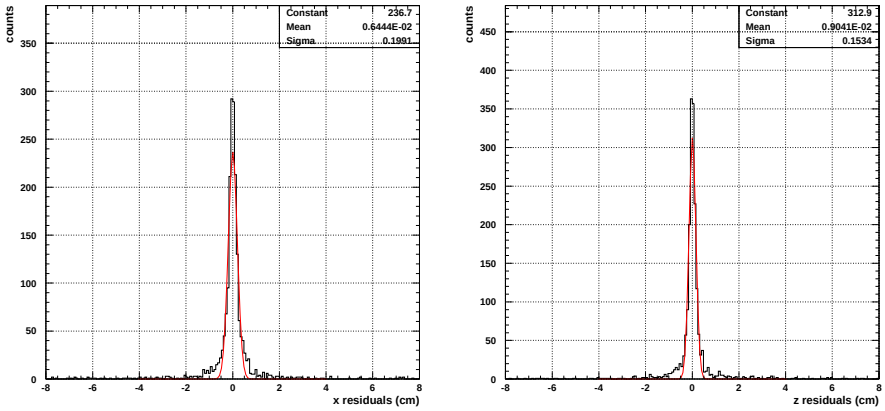

(a) (b)

Figure 3.32: Residual for the x (a) and z (b) directions computed without considering the finite resolution of the fiber detector: in this case the difference between the reconstructed vertex and the real annihilation point is totally due to the multiple scattering effects.

but they would have been the limiting factor if a smaller channel pitch had been used.

To investigate the resolution dependence on the vertex position, two scans have been performed on the z and x axes (see Fig. 3.33): along the z direction the resolutions are almost constant, and start to degrade only outside the detector ($|z| > 25$ cm); on the contrary moving away from the tracker axis the resolution becomes much worse because

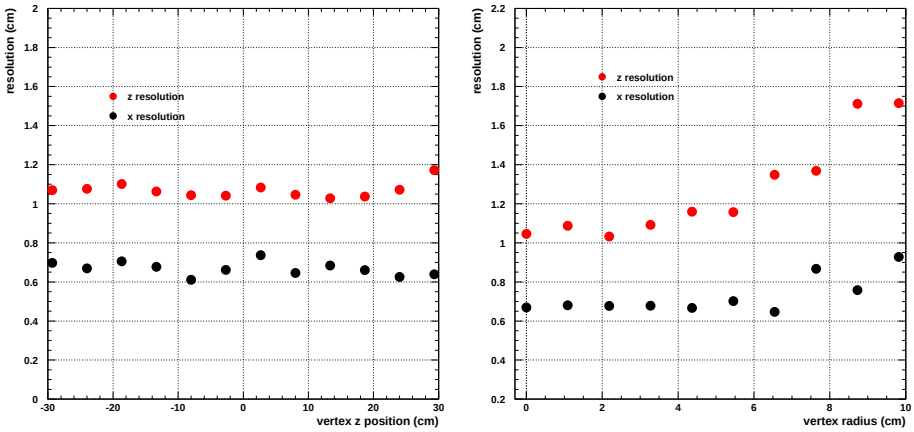

(a) (b)

Figure 3.33: (a) Spatial resolution, i.e. the σ of a gaussian fit as computed in Fig. 3.31, as a function of the position on the detector axis and (b) as a function of the distance from the axis itself.

of the increasing effect of the parallax error.

From the resolution values computed above, it is possible to evaluate the performance of the detector in the target–wall annihilation separation, if a scenario for the beam size inside the tracker volume is assumed.

In the hypothesis that the transverse beam size is gaussian with a σ_{beam}=1 cm [9], the on target annihilation events will be reconstructed in a region with a gaussian profile having $\sigma_{\text{beam}} + \sigma_x \simeq 1.2$ cm. So if a cylindrical fiducial region with a radius r=3 $\times$ σ = 3.6 cm is considered, the annihilation events can be reconstructed with a 99.8% efficiency; meanwhile, since the beam pipe diameter is ø=14 cm and the r vertex resolution, at r=7 cm, is $\sim$ 0.9 cm, the probability that a wall annihilation is reconstructed inside the fiducial volume is less than 10^{-3}.

It is worth to remember, anyway, that a large number of on–wall annihilations can be a problem for a second reason: they can lead to the saturation of the detector. This topic will be discussed in detail in the next Chapter.

[9] Value that should be considered very conservative, since the AD experts report as feasible a beam size well below 5 mm (private comunication).

Chapter 4

FAST commissioning and physics expectations

The detector development, which started in January 2005, has been concluded in time for the September 2006 two week data taking period; unfortunately the very bad beam conditions prevented the collection of any useful data in 2006 (the beam issues will be discussed later on). The detector has then undergone a cosmic ray commissioning phase, to evaluate its performances in terms of efficiency, hit reconstruction, cross talk and spatial resolution.
In June 2007 the detector has been positioned on the ASACUSA beam line, for a two week data taking period, during which annihilation events have been recorded.
This Chapter describes the configurations in which the FAST detector has been used as well as the obtained results.
In Sec. 4.1 the setup for the cosmic run is presented and the results of a two month cosmic ray data collection are reviewed.
Sec. 4.2, dedicated to the Summer 2007 data taking at CERN, will describe the setup at the ASACUSA beam line at the Antiproton Decelerator, the beam and the detector operation during the data taking period, and finally the results of the FAST tracker as a vertex reconstructor.

4.1 The cosmic ray run

4.1.1 Adapting FAST for cosmic ray detection

The information collected during the cosmic ray run has been of fundamental importance to understand the detector behaviour; nevertheless, for a better understanding of the cosmic ray setup, it is important

to list the differences, from the detector point of view, between this cosmic ray situation and the environment which the detector is designed for:

- The cosmic ray direction is mainly oriented with the zenith, so that the cosmic ray flux impinges on less than half of the detector; the coverage can be extended by turning the detector of 90°
- The cosmic rays pass through the tracker with no or very little deviation from a straight line, so there is no way to test the vertex reconstruction capability; on the other side an external reference tracking detector can be used for the spatial resolution measurement
- The cosmic particles are isolated in time: a single particle is detected in each trigger
- A trigger system has to be provided, for example with a plastic scintillator system
- The trigger will arrive to the frontend boards after the signal from the tracker itself.

To address the last problem a modified version of the sampling logic described in Sec. 3.2.2 has been loaded in the Cyclone 2 FPGAs. In the standard logic the shift registers which perform the sampling are activated only after the trigger signal is received. In the new one the registers are always running, apart during the time needed for the boards readout by the VME system. Once a trigger is received, a counter, with the clock synchronous with that of the register, is started: when the counter reaches 128, that is half of the registers depth, the clock to the registers is stopped and the boards wait for the readout.
This means that the fiber signal, if present, will be found somewhere before the half of the shift registers. One drawback of this logic is that the 320 MHz clock on the FPGAs is running most of the time, thus increasing by a factor 3÷4 the power consumption of the sampling system. Since the particles hit only half of the tracker, half of the PMTs have been actually assembled with the readout electronics. The PCBs of Fig. 4.1a have been used to route the multianode PMT signals to the four 26 pin ERNI cables for the frontend board connection. A lemo connector on the PCB supplies the high voltage to the PMT.
The twelve frontend boards have been stacked in front of the PMT support plate and connected with the photomultipliers themselves (Fig. 4.1b). In Fig. 4.2a the complete DAQ system, made of the

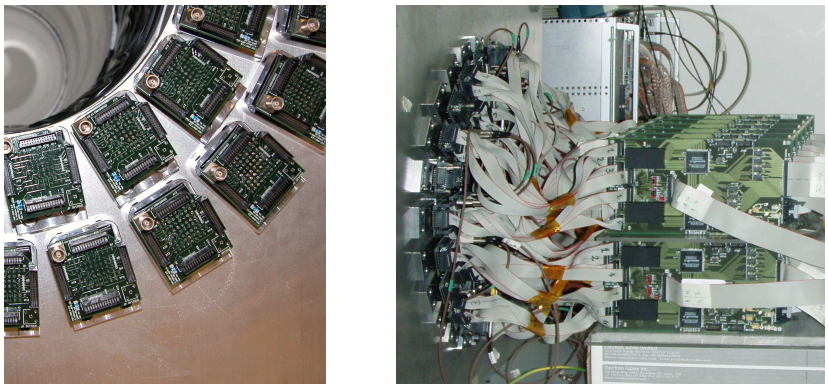

(a) (b)

Figure 4.1: (a) Detail of the printed circuit boards developed for the PMT–frontend electronics connection, already in place. Each 26 pin ERNI cable delivers 16 signals (the others are ground connections), while the high voltage is provided through the lemo connector. (b) The twelve frontend boards connected to the photomultipliers.

frontend boards, the repeaters and the VME system, is shown.
A full digital readout has been used for the cosmic ray detection, while one VFAS flash ADC allowed the pedestal analog readout for the noise evaluation. A Silicon strip tracking system, composed of the detectors described in Sec. 3.1.2, has been used to provide an external reference. To minimize the errors on the track projection, the FAST tracker has been inserted between the two X-Y planes of the Silicon system, as shown in Fig. 4.2b. The trigger system is provided by two plastic scintillators: a 20×30 cm^2 pad placed on the detector top, and a 10×10 cm^2 counter placed inside the detector itself. The scintillators could be moved to cover different regions along the z axis, maintaining the relative position of their centers. Their analog signals were digitized by a CAEN mod. 96 discriminator and sent to a LeCroy 465 coincidence unit that generated the trigger signal. A trigger rate of 0.1 Hz was obtained in this configuration.

4.1.2 Time resolution

The trigger system had an intrinsic time resolution better than 1 ns. This allowed to evaluate the time resolution of the FAST detector: the distribution of the arrival times for the hit channels is presented in Fig. 4.3a. The distribution shows a gaussian core with an asymmetric tail that extends towards the higher values of time. At least two effects contribute to this tail:

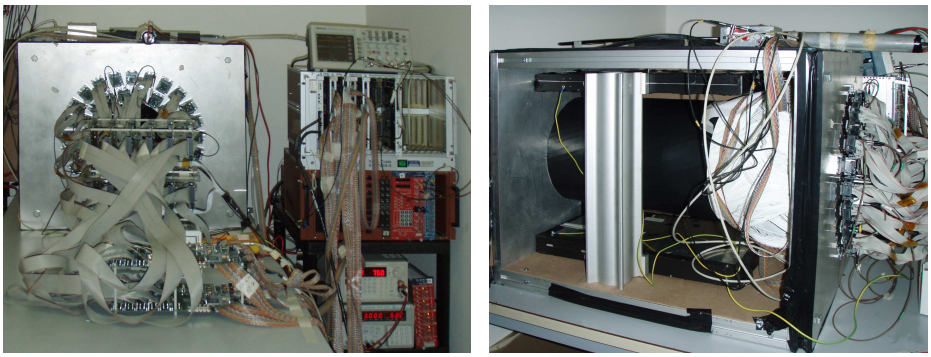

(a) (b)

Figure 4.2: (a) Front view of the whole FAST system during the cosmic ray run. To acquire data also with the other half of the detector, at a certain point the tracker has been turned of 90° clockwise and the other PMTs have been connected to the electronics. (b) Side view, with the light screening panel removed. The trigger system was provided by a scintillator on the top (whose PMT is clearly visible) in coincidence with a smaller one inserted into the tracker itself (hidden). The two Aluminum boxes mounted on the vertical rail contained the Silicon tracking system used as a reference.

- The intrinsic distribution of the collected charge, for a given channel, is poissonian: this means that hits with a low pulse height are possible, even if with a low probability. Since the measured time is the one in which the analog output of the shaper crosses a level (the threshold), these low amplitude events generate longer times, as shown in Fig. 4.4

- The gain spread of the different channels strengthens the effect, amplifying the differences between the highest and the smallest signals.

A threshold scan has been performed to verify if a dependence of the time resolution on the global threshold exists. Data sets have been taken with thresholds ranging from 27 mV to 210 mV. For each threshold the time distribution has been fitted with a gaussian curve. Since the width of the gaussian has a strong dependence on the fit limits, the fit procedure has been repeated 10 times for increasing size intervals: the mean and the r.m.s. of the sigmas have been used to compute, respectively, the time resolution and the error bars of Fig. 4.3b.
The variations of the time resolution with the threshold are within the experimental errors while the mechanism described in Fig. 4.4 would suggest that with a lower threshold the time spread could be reduced.

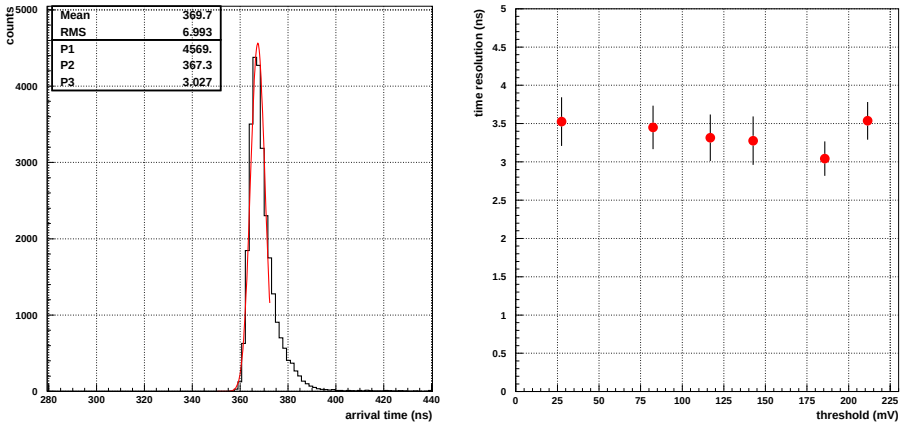

(a) (b)

Figure 4.3: (a) Distribution of the arrival times for the ∼1000 connected channels, with a gaussian fit superimposed. 88% of the counts are inside the gaussian. Data taken at a 800 V PMT bias and with a 140 mV threshold. (b) Time resolution threshold scan: for each threshold the arrival time distribution has been fitted with a gaussian curve. The resulting sigmas are plotted. The error bars are explained in the text.

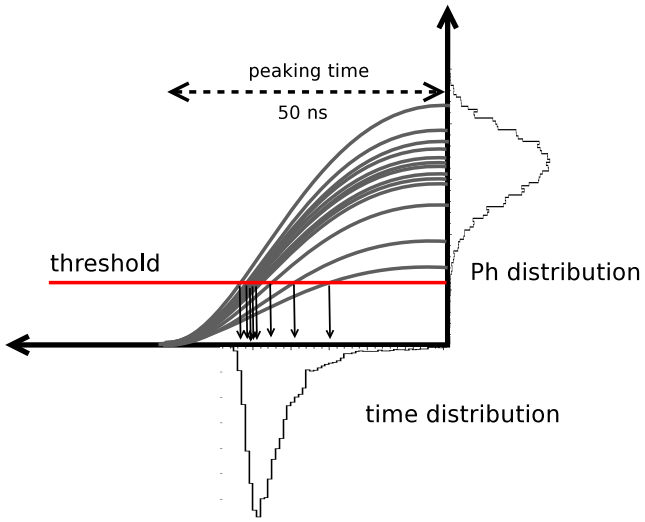

Figure 4.4: The tail in the arrival time distribution is generated by the statistical fluctuations in the pulse height (i.e. in the collected p.e. number), if a fix threshold is used. The represented histograms are from a computer simulation of the effect.

In a real system, however, lowering the threshold increases the time error due to the baseline shifts (induced by noise): in the FAST case the two effects cancel out almost completely. To summarize, two values for the time resolution of the FAST detector can be defined, depending on the working scenario:

- If the occupancy is high, with different annihilation events a few nanoseconds apart, and the arrival time information is used to associate the hit fibers to the correct annihilation event, the time resolution can be assumed equal to 7 ns, which is the r.m.s. of the distribution of Fig. 4.3a. In practice two annihilations occurring in an interval smaller than this value are not distinguishable
- If the occupancy is low and physical events are isolated, the time of each reconstructed event is known with an uncertainty lower than $\sigma_t = 7 \times \frac{1}{\sqrt{12}}$ ns=2.2 ns, since 12 is the minimum number of hits associated to the "vertex", corresponding to the 6+6 layers crossed by a cosmic ray.

4.1.3 Efficiency

The shell structure of the detector, with its 3 layers having approximately the same radius, has allowed an efficiency measurement independent from the hit reconstruction. Since the cosmic rays detected by the trigger system have crossed the center of the detector, they had to cross 2 times all the 6 fiber layers, one in the top half, the other in the bottom half. So, each layer has been vertically divided, obtaining 12 half-layers which have been grouped 3 by 3 following the shell structure.
Considering these groups, the efficiency of one layer could be computed as the ratio between the number of times all the 3 half-layers of a group had signals and the number of times at least the other two half-layers had signals. The results are shown in Fig. 4.5a for a threshold voltage of 142 mV and a PMT bias of 800 V: if the half-layer having one bad connected PMT[1] is excluded, the efficiency varies from 93% to 97% with an average value of 95.9%.
Since the efficiency is expected to be threshold dependent, a threshold scan has been performed: in Fig. 4.5b the average efficiency as a function of the threshold is reported. As expected, the efficiency decreases increasing the threshold, apart from the very first point where there is a high probability that noise hits in coincidence appear in two of the

[1] A poor quality soldering has been found to be the cause of the problem, that has been fixed for the following AD runs.

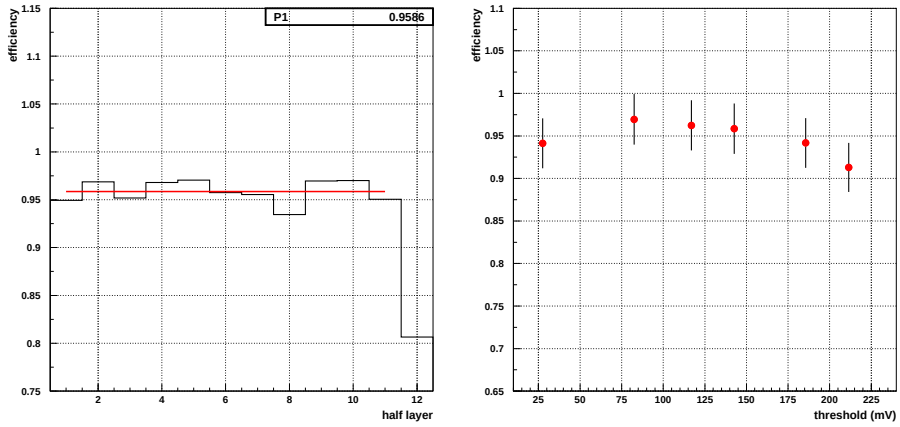

(a) (b)

Figure 4.5: (a) Efficiency of the 12 half-layers, for a 142 mV threshold. The layers are ordered from top to bottom, in the cosmic ray arrival direction. The last half-layer has a lower efficiency since one of the PMTs was missing. Once excluded, the average efficiency is 95.9%. (b) Efficiency as a function of the threshold voltage, for a 800 V PMT bias.

half-layers resulting in an apparent inefficiency of the third half-layer. It is worth to note that the efficiency is higher than the one measured during the prototype beam test ($< 92\%$). One possible reason is the fact that cosmic particles cross the detector layers with a non zero angle with respect to the perpendicular, thus releasing, in average, slightly more energy in the fibers. Anyway, the efficiency is correctly estimated, since the tracks of the pions coming from the antiproton annihilations inside the detector have similar characteristics.

4.1.4 Cross talk

The following procedure has been used to evaluate the optical cross talk at the fiber–photomultiplier interface (for the cross talk origin see Sec. 2.1.2). If a cross talk happens, two or more neighbouring anodes on the PMT surface are hit, generating what is called a cluster. For each group of hits the center of the cluster is computed, and a 3 by 3 grid around it is considered. Each point of the grid is filled only if the corresponding channel is over threshold. The resulting lego plot is shown in Fig. 4.6: in 63% of the events a pad near the central one is hit. For most of the PMTs the fiber order is such that the channels which are close together on the PMT are far on the detector layers, so the plot represents real cross talk events and not particles which have crossed two near fiber quartets.

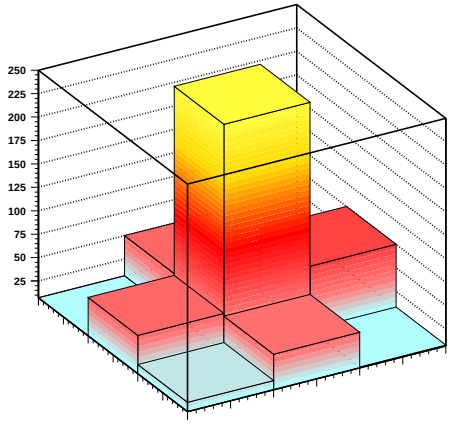

Figure 4.6: Example, for one PMT, of a 2D cross talk histogram. The 8 external pads are hit, because of the cross talk, in 63% of the events.

It is important to note that this "non order" between the fibers and the PMT pads makes the cross talk more problematic: in fact in case of an ordered fiber–PMT coupling, like the one used for the stereo prototype, the optical cross talk in one direction introduces little or no error on the position reconstruction, while with a random fiber–PMT coupling every hit due to cross talk effects appears as a fiber quartet located somewhere else in space.
During the very first cosmic ray run some of the PMTs showed a cross talk much worse than the average one: this has been ascribed to a misalignment of the PMTs themselves. For the following runs, they have been re-aligned: Fig. 4.7a shows the effects of this operation on one of the PMTs.

The cross talk is expected to decrease if the threshold is raised: a threshold scan has been performed, and the results are shown in Fig. 4.7b.
The detector design, which uses three layers for the point reconstruction, allows to find the correct hit position also in case that a few fibers randomly lighted for cross talk are present. In fact the exceeding fibers will produce, in almost all cases, larger triangles that will be rejected choosing the smallest triangle defined by the "true" channels. Anyway, the cross talk is disturbing for the following reasons:

- It prevents the possibility to reconstruct a hit if one of the three layers is missing when an inefficiency occurs. If no cross talk was there, two fibers on the two layers would be enough to define a point in space, although with a lower spatial resolution, but any cross talk fiber produces one or more ghost hits

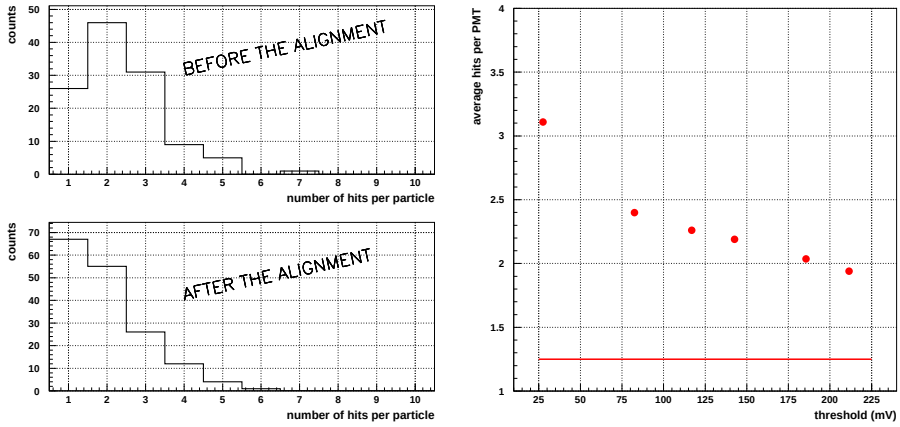

(a) (b)

Figure 4.7: (a) Effect of the photomultiplier misalignment on the cross talk probability. The cross talk of a PMT is proportional to the average number of detected hits per crossing particle. This value decreased, after the alignment, from 2.36 to 1.98. (b) The average number of hits per particle, over all the PMTs, is plotted as a function of the threshold. The horizontal line represents the theoretical average number of hits for the geometry of the fiber doublet ribbons with a readout every 4 fibers.

- It increases the apparent occupancy of the detector, since the channel which is enlightened because of cross talk is no more available for a particle detection.

4.1.5 Hit reconstruction and resolution results

From the channels above threshold, the hit position has been reconstructed using the same procedure developed for the prototype module, described in Sec. 3.3.2. The height of the reconstructed triangles can be used for a first evaluation of the tracker behaviour: for each cosmic ray, and for each half-shell[2], the smallest triangle height is considered. The resulting distributions are shown in Fig. 4.8.
The distribution widths, computed with the help of a gaussian fit, are in perfect agreement (0.70 mm vs 0.71 mm for the outer shell) with the one obtained during the stereo prototype beam test. The larger gaussian tails surrounding the cores, which are probably due to tracks far from the detector axis, that cross the detector layers with a larger angle with respect to the perpendicular, are again in agreement with the results obtained with the montecarlo simulation of the tracker itself (Fig. 3.30).

[2]A half-shell is obtained dividing the tracker on a horizontal plane so that a cosmic ray, on its path, crosses 4 half-shells: in other words, three half-layers make a half-shell.

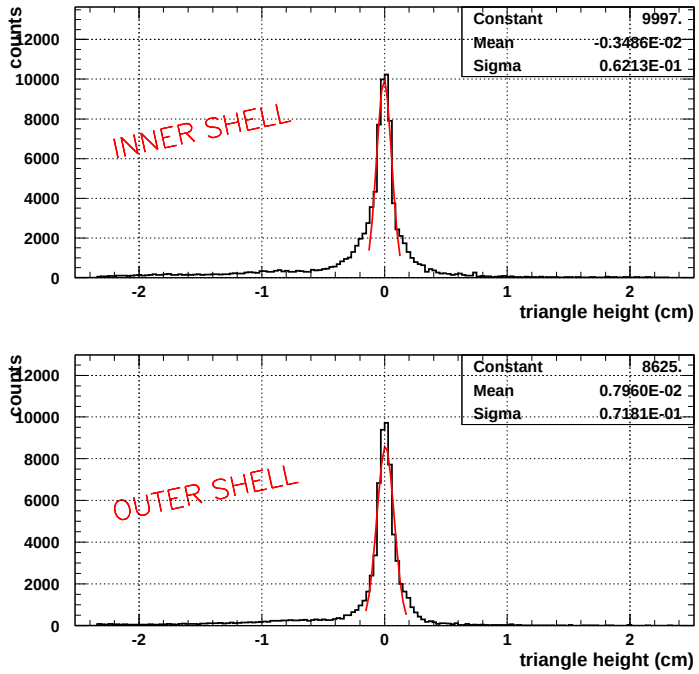

Figure 4.8: Distribution of the heights of the smallest reconstructed triangles for the inner and the outer shell. The cores of the distributions have a width (0.62 mm and 0.70 mm r.m.s. respectively) which is consistent with the value expected from the prototype results of Sec. 3.3.2, but non negligible tails, extending up to 2 cm, are also present.

Moreover, the tails are asymmetric, being larger towards the negative height region: this effect can only be explained with a fiber misplacing involving a large number of fibers; in other words the function $\phi(n)$, where n is the fiber number, which is supposed to be a simple linear relation, is not such.
A few hypotheses on the nature of the placement error have been investigated, with the hope to find some rule in the misplacement and to provide an offline correction: for example the function $\phi(n)$ could have a step discontinuity (hole in the fiber row), a different slope (bigger spacing between fibers, in a subregion) or a local inversion. Unfortunately, Fig. 4.9, where the heights of the triangles are plotted as a function of the ϕ position of the triangles themselves (namely the position of the axial fiber used as the triangle base), shows no evidence of a ϕ dependence of the misplacements: it seems that the errors are randomly distributed in the whole region covered by the cosmic ray flux. This implies that no offline corrections would solve the problem and the placement errors have to be taken as they are: while the hit reconstruction is still possible, a worse resolution will be obtained.

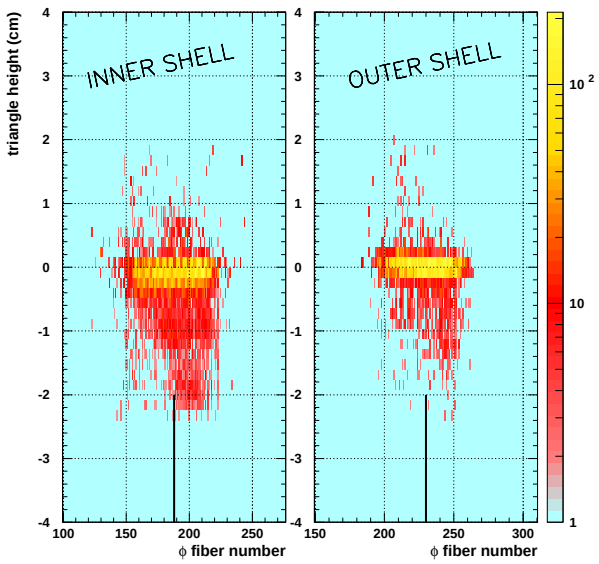

Figure 4.9: Height of the reconstructed triangle as a function of the fiber of the ϕ layers (layers 3 and 4) forming the triangle, for the bottom halves of the tracker. Note the logarithmic scale of the colour map. The inner shell is more affected by the error with respect to the outer one, but no dependence on the ϕ coordinate can be seen. The thick vertical line indicates the nadir.

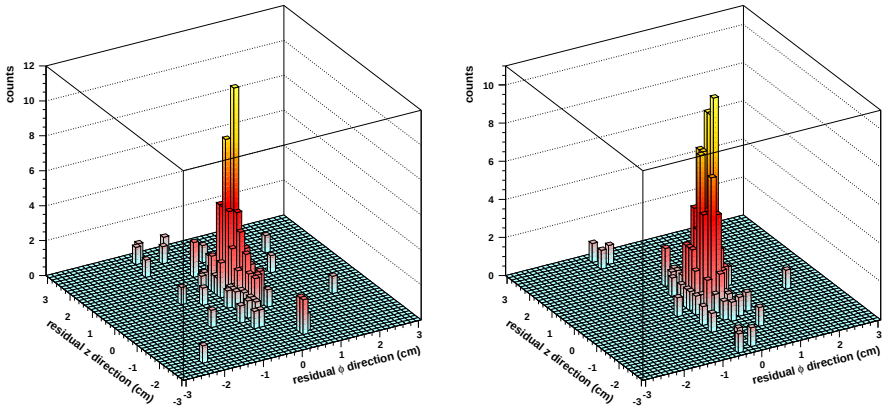

(a) (b)

Figure 4.10: 2D distributions, on the inner (a) and outer (b) shell, of the residuals between the muon track as computed by the Silicon detector and the hit position as reconstructed by the FAST tracker. In the ϕ direction a 1 cm distance corresponds to 9.4° and 7.4° respectively.

To evaluate the resolution, the tracks of the cosmic particles as given by the Silicon detectors have been used. The muon[3] tracks have been

[3]Cosmic rays at ground level consist in muons for more than 80%.

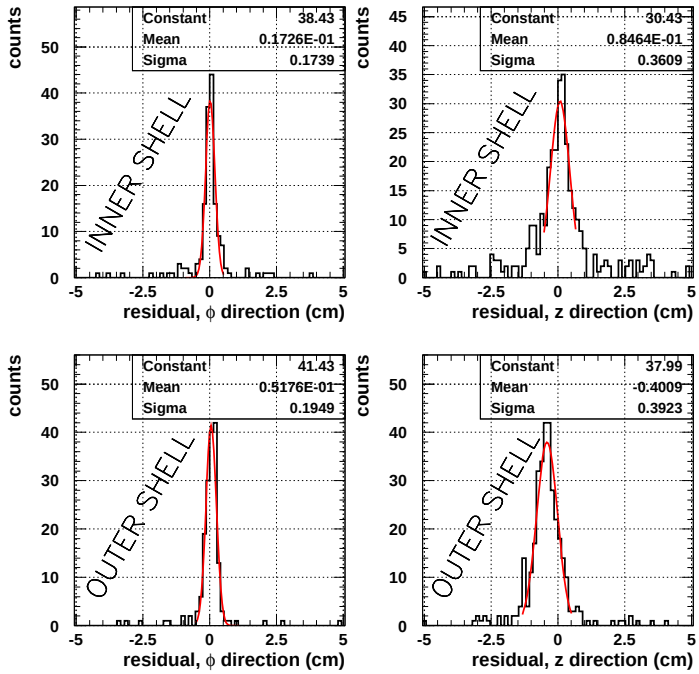

Figure 4.11: ϕ and z distributions of the residuals for both the inner and the outer shell. The gaussian fits allow to extract the following r.m.s. values: $\sigma_{r\phi in} = 1.7$ mm, $\sigma_{r\phi out} = 1.9$ mm, $\sigma_{zin} = 3.6$ mm and $\sigma_{zout} = 3.9$ mm.

projected on the two cylindrical surfaces corresponding to the detector shells, obtaining the (ϕ,z) coordinates of the four hit points. The FAST reconstructed hits have been computed, for each half-shell of the scintillating fiber tracker, as the center of gravity of the smallest triangle. The residuals, defined as the difference between the two points, are shown, for both the detector shells, in Fig. 4.10 (2D plot) and in Fig. 4.11 (ϕ and z projections).

The combined presence of cross talk effects and of the fiber misposition problem could, in principle, make the smallest triangle selection criteria useless. In fact, more than one triangle can be present in the surrounding of the hit point (because of the cross talk) and the right triangle is not always smaller than the others which are "randomly" created by cross talk (for the errors in the fiber positioning).

To verify how much this problem affects the resolution, the residuals have been computed also using a different selection method: the triangle which was nearer to the Silicon track has been selected. The results are shown, for the inner shell, in Fig. 4.12: with this method the resolution ($\sigma_{r\phi in} = 1.5$ mm, $\sigma_{zin} = 3.1$ mm) is smaller by a factor $20 \div 30\%$.

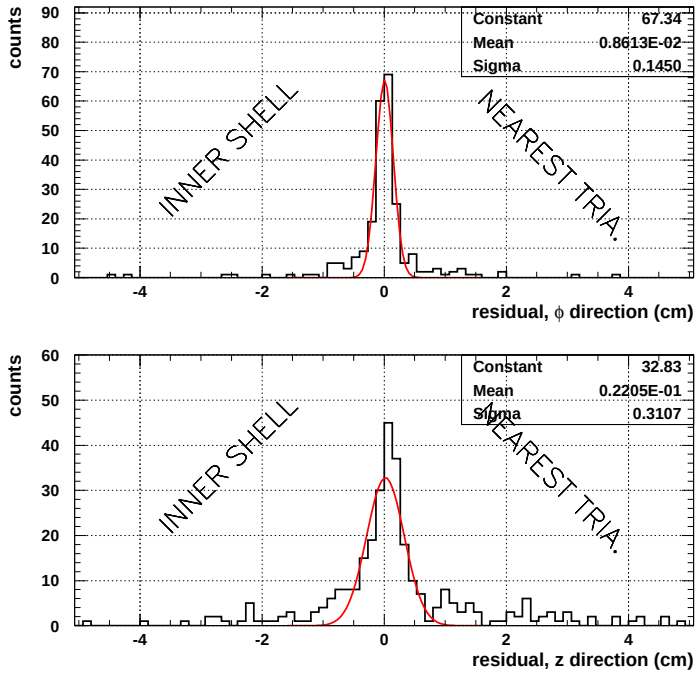

Figure 4.12: ϕ and z distributions of the residuals for the inner shell, computed considering the triangle nearer to the Silicon detector hit, instead of the smallest available triangle used for Fig. 4.11. A gaussian fit is superimposed.

Of course, the nearest triangle selection method, depending on the reference Silicon tracker, cannot be used in the normal data taking: thus the hit reconstruction errors obtained with the previous method (Fig. 4.11) have to be considered when evaluating the performances of the detector.
This can be accomplished by running the MC simulation of Sub. 3.4.2 with the real spreads instead of the prototype values, as previously done.

In Fig. 4.13 the results for annihilation events generated in the center of the detector are shown. Despite the resolution of the vertex reconstruction, which is almost a factor 2 worse than the expected one, these values can still allow a good target–wall separation and the needed target identification in the z coordinate.
As a final remark, if the r.m.s. values of the gaussian of the residual plots (Fig. 4.11) are compared with the ones obtained for the prototype beam test ($\sigma_{r\phi}$=0.57 mm, σ_z=1.59 mm, Fig. 3.23), the values are worse of a factor 2$\div$3. Since all the other conditions have been kept the same, the main cause for this is the unperfect fiber positioning over the cylindrical surfaces of the tracker. The manual assembly of

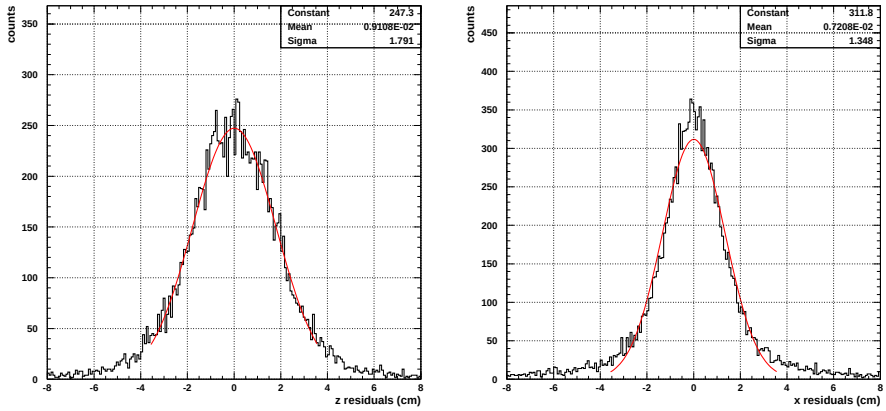

(a) (b)

Figure 4.13: Results of the montecarlo simulation described in Sec. 3.4.2, with the single shell resolution as measured during the cosmic ray run, instead of the stereo prototype one. (a) Residuals in the z direction, evaluated in the center of the detector. (b) Residuals in the x direction, for the same position. The resolution values are σ_z=17.9 mm and σ_x=13.5 mm, a factor 1.7÷2 larger than the design values reported in Fig. 3.31.

the whole tracker, which is a difficult task in itself, has been performed in a short time, to be ready for the data taking that couldn't be postponed, and in parallel with the electronics development, so that no tests could be made to verify the alignment; for these reasons a worsening of the resolution due to placement errors was expected.
A dedicated run with a high energy beam (to avoid multiple scattering) and with a reference telescope is foreseen to map the fiber positions.

4.2 Data taking at the ASACUSA beam line

4.2.1 The ASACUSA beam line

While the general working principles of the Antiproton Decelerator are listed in Sec. 1.4, a detailed description of the beam line where the detector has been positioned is presented in the following.

A global view of the experimental lines is shown in Fig. 4.14 [74]: the extraction line 7000 connects the magnetic septum which extracts the antiproton bunch from the AD ring with the bending magnet ATP.BHZ8000. This magnet steers the beam into the DE0 line, the common transport line for all the AD experiments; it is made of two horizontal bending magnets (DE0.BHZ12 and DE0.BHZ18), a quadrupole doublet (DE0.QN20 and DE0.QN30), two quadrupoles at

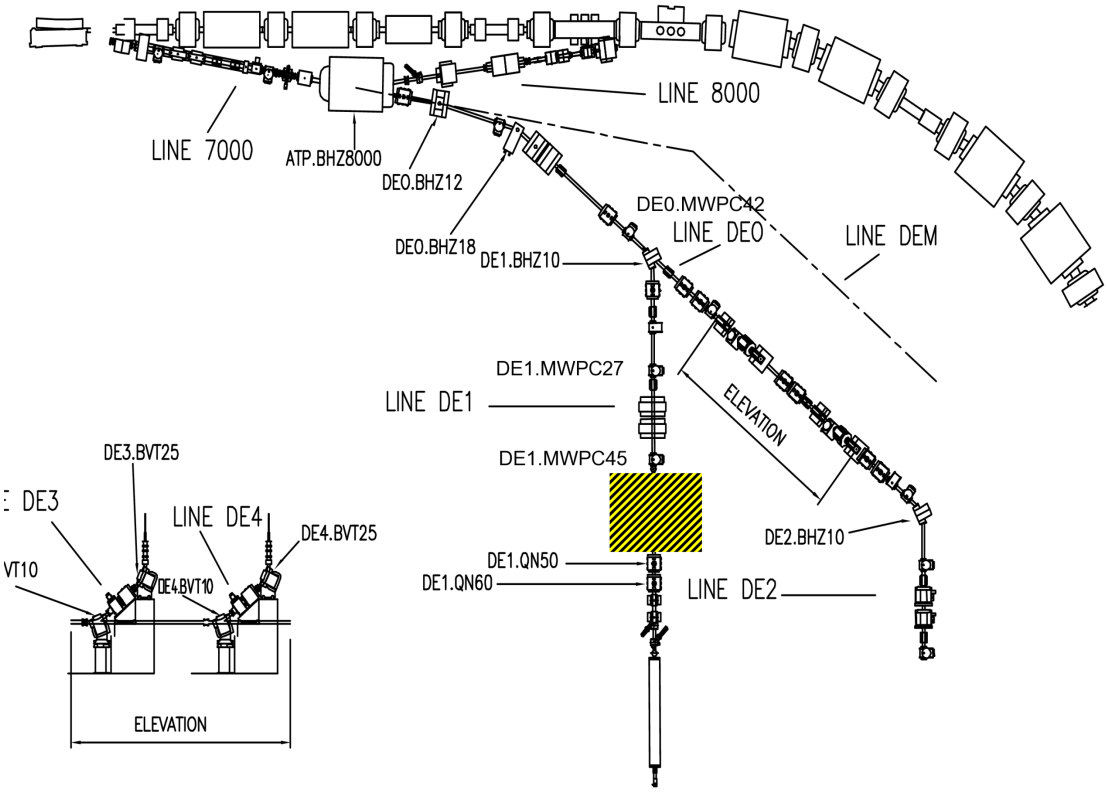

Figure 4.14: Overall view of the Antiproton Decelerator experimental lines, with the ASACUSA beam line indicated as DE1. The position where the experimental setup has been installed is highlighted.

the beginning and at the end (DE0.QN10 and DE0.QN40) and a corrector. The line ends into the DE0.BHZ10 bending magnet which selects the final antiproton destination: if it is turned off, the beam reaches the ATRAP and ALPHA zones, while if it is on, the beam is steered into the ASACUSA DE1 line.
On this line the following elements are positioned: one quadrupole (DE1.QN20), a corrector (DE1.DHV25), the beam stopper (which allows the area access with AD running), a second corrector (DE1.DHV28) and a quadrupole doublet (DE1.QN30 and DE1.QN40). While the DE1 line normally continues into the RFQD apparatus, for the 5 MeV data taking the experimental setups are placed after these two quadrupoles. The axis of the horizontal beam line is located 1.2 m above the ground level.
To check the beam steering, four Multi Wire Proportional Chambers (MWPC) are placed on the DE0 and DE1 lines. They are gas detec-

tors with two planes of anode wires operated in proportional mode [75][76]; each plane is made of 16 wires with a 5 mm pitch, so that the covered area is 8×8 cm^2. An automatic system allows to insert and remove the detectors from the line, a quite important feature since a single detector completely stops the beam.
Despite the fact that the MWPCs are the standard CERN beam profile monitors and are successfully used in a lot of experimental areas, in the AD case their performances are greatly reduced by the physics of the beam itself. In fact 5 MeV antiprotons annihilate in the first tens of μm of the first face of the detector: the isotropic burst of secondary particles which are produced impinges on the whole MWPC, so that an extreme blurring of the beam profile occurs. As a result these devices are still useful to center the beam inside the pipe, but give very little information on the dimension of the beam itself.
A much better profile monitor has been developed by the ASACUSA collaboration: it is a photocathode microwire monitor made of 32+32 x-y gold-coated tungsten wires (ø=10 μm), with a 2 mm pitch [77]; each wire detects the charge deposited by the stopped antiprotons, but the wires are small and distant, so that a very sharp profile of the beam can be obtained. Unfortunately, this kind of detector is fixed on the beam line and cannot be removed (this is possible since each detector stops only a tiny fraction of the particles), so it cannot be placed in front of the FAST detector to have the information on the beam profile just before entering the tracker itsef.

4.2.2 The experimental setup

To connect the apparatus to the ultra high vacuum AD pipe, a dedicated vacuum system (Fig. 4.15a) has been designed. Moving on the antiproton path, the following items can be found:

- A X shaped pipe with a turbo pump and a ionic pump respectively in the upper and lower branches. A vacuum flat valve allows to exclude the turbo pump at low pressures, when only the ionic pump is running
- A manual flat valve. Closing this valve the pumping system is isolated from the pipe assembly, which can be accessed for the target replacement while the ionic pump is still on
- The thin (3 mm) Aluminum pipe, one meter long, which houses the target support system
- The large diameter iron vessel which ends into a blank flange. This piece has to be unscrewed from its flange and taken away

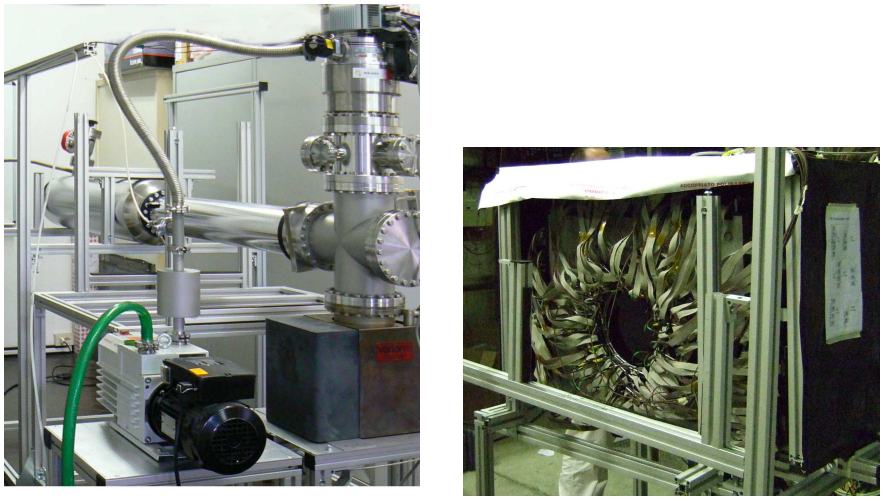

(a) (b)

Figure 4.15: (a) The vacuum system assembled for the vacuum test. From left to right the system is composed of: the turbo and ionic pumps, the manual valve, the thin pipe which will be surrounded by the detector and the large iron vessel. (b) The FAST detector before the vacuum system integration. The frontend boards are fixed on the detector faces, protected by the black plastic covers.

each time the Aluminum pipe is accessed for a target replacement. A 1" flexible pipe exits at the end of the vessel

- This pipe is connected, through a valve, to a turbo pump, to perform a fast emptying after the target replacement
- A gas rack, which is used to flush the apparatus with Nitrogen to prevent moisture contamination.

After a target replacement, the vacuum system can lower the pressure inside the apparatus to a level compatible with the AD line (a few 10^{-13} bar) in less than 5 hours. Since the target replacement, from the mechanical point of view, needs no more than 2 hours, the operation can be easily performed within the 12 hours between two shifts[4]. The longitudinal size of the apparatus is limited, and an easy and frequent access to the target pipe has to be possible, so the frontend electronics has been placed on the external faces of the FAST detector, with the 26 pin ERNI cables which connect the PMTs running on the front plate of the detector itself (Fig. 4.15b). The repeater boards have been placed on the top of the tracker, on the opposite side with respect to the PMTs. In this way the total length of the detector,

[4]The AD beam time was used by ASACUSA for 12 hours a day while the remaining time was exploited by ATRAP/ALPHA.

cabling included, has been kept under 90 cm.
To monitor the beam intensity, two beam counters have been used: a 20×10 cm^2 scintillator with Hybrid PhotoDetector (HPD) readout and a 60×40 cm^2 Cherenkov radiator.
The HPDs are high dynamic range photodetectors made of a vacuum housing with a photocathode, which is kept at a negative high voltage (a few thousands of Volts), on one side and a Silicon photodiode at the opposide side acting as an anode plane. When a photon strikes the photocathode emitting an electron, the electric field accelerates it towards the diode, where it stops releasing its whole energy inside the Silicon. Given the 3.6 eV energy needed, in Silicon, to create an electron-hole pair a single electron accelerated by a 10 kV potential produces $\sim$2800 e$^-$ inside the Silicon. The drift field of the diode (a bias of a few tens of Volts is applied to the diode itself) collects the electrons generating the output signal.
The HPD is connected to a 1 cm thick plastic scintillator (Bicron BC-408) with a lucite light guide, and is enclosed in a light tight Aluminum box. The detector has been successfully used to evaluate beam intensities as high as 10^7 antiprotons per bunch during the ATHENA experiment [78]. This detector has been fixed, in a vertical position, just behind the end wall of the vacuum pipe.
The Cherenkov counter [79] is made of an acrylic slab (Bicron BC-800), 2 mm thick, with a refractive index of 1.49, so that a charged particle with $\beta > 0.7$ (corresponding to a $\sim$130 MeV/c momentum given the mass of the charged pion) can produce Cherenkov radiation when crossing the device. The light is readout by a fine mesh gateable photomultiplier (R5505GX-ASSY by Hamamatsu), that is assembled inside a module with integrated high voltage supply and adjustable gain. Due to its big dimension, this detector has been placed vertically 20 cm far from the end wall, with the face pointing towards it.
The analog signals from the two detectors have been splitted: one output was sent to a passive attenuator (-24 dB and -36 dB respectively for the HPD and the Cherenkov detector) and then to a CAEN V792 charge to digital converter (QDC), while the other was sent to the counting room to be displayed on a Tektronik 2020 oscilloscope to monitor the timing and the beam status.
The experimental setup has been placed on the beam line of the ASACUSA experiment (Fig. 4.16a): the 5 MeV beam is available on the first part of the line, before the RFQD apparatus, interrupting the transfer line to the RFQD itself. For this reason a limited longitudinal space is available. The pump system has been aligned and attached to the beam pipe, the detector has been put in place, the thin Aluminum pipe inserted into the detector and screwed to the pump system, then

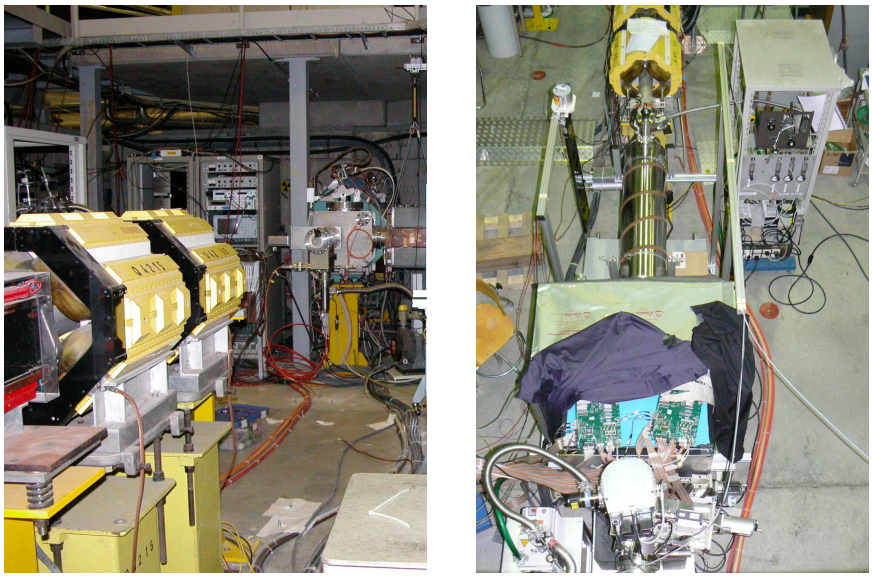

(a) (b)

Figure 4.16: (a) The first part of the ASACUSA beam line before the FAST tracker was inserted, with the beam arriving from top right. A part of the RFQD transfer line, two of the quadrupoles (in yellow) can be seen. (b) The complete setup during the data taking. From bottom to top the following items are visible: the turbo and the ionic pumps, the FAST detector with the repeater boards on top, the large diameter vacuum pipe, the HPD and the Cherenkov counter placed at the end wall and the gas rack.

the large vessel has been placed afterwards, with its supporting frame. The resulting setup, after cabling, is shown, in Fig. 4.16b while the inner part of the apparatus, hosting the target, is shown in Fig. 4.17.

4.2.3 Tuning the antiproton beam

When the beam reached the detector the first time, the situation appeared to be extremely different from the expectation. On one hand, the FAST tracker was triggered at least 600 ns before the arrival of the antiproton beam, on the other hand, the detector seemed to be saturated already at about 250 ns from the sampling gate start. This was confirmed by a 10×3 cm^2 plastic scintillator, sensitive to a single charged particle, placed just near the front face of the tracker itself: Fig. 4.18a shows a scope waveform of the scintillator superimposed on the track from the high range HPD. While, on one hand, the time width of the main antiproton bunch, computed as the sigma of a gaus-

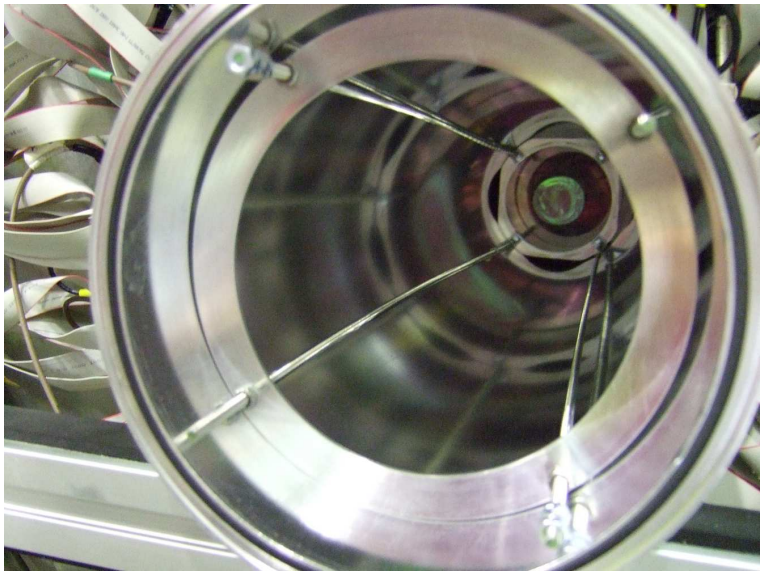

Figure 4.17: The inner part of the Aluminum pipe hosted by the FAST tracker, during one of the target replacements. The target support structure and the target itself are clearly visible. The 267 nm Ni layer sputtered on the mylar foils becomes greenish.

sian fit of the HPD signal (18.2 ns), is as small as expected, on the other hand a large number of particles hits the scintillator already 350 ns before the main antiproton bunch reaches the end wall, producing the peak in the HPD waveforms. These particles are enough to saturate the detector, so that, when the main burst arrives, it is recovering from saturation and only a small (and delayed) peak appears. As a further confirmation, a dedicated run has been taken lowering the photomultiplier voltage on a subset (6 PMTs) of the FAST detector; a 320 V bias has been set instead of 775 V, corresponding to a reduction factor of $\sim 10^3$ in gain. The resulting arrival time distribution, accumulated over 30 AD bunches, is shown in Fig. 4.18b. The main bunch is well detected by the low voltage PMTs while the normal ones are over the threshold already 400 ns before. It is important to note that a channel that has fired could in principle recover in 150$\div$200 ns and so be hit a second time, but this did not happen in our case since an uninterrupted flux of particles flooded the detector, preventing the electronics to restore from saturation.
Two possible sources of these first particles have been investigated. The first one was the production of secondary particles in the upstream regions of the beam line: since the antiprotons are travelling at a 3 cm/ns speed, if the bunch was hitting the pipe a few meters

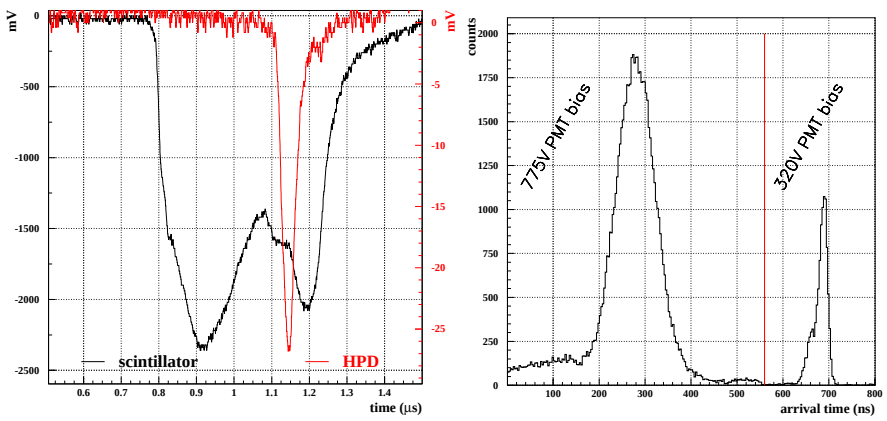

(a) (b)

Figure 4.18: (a) Scope waveforms from a high sensitivity scintillator (placed near the enter face of FAST) and from the high range HPD at the vessel end wall. The scintillator is saturated hundreds of nanoseconds before the main bunch arrival. (b) Distributions of the arrival times on the FAST fibers, during a dedicated run with 6 of the 42 photomultipliers biased with 320 V. All the "normal" channels of the tracker have been hit much before the main bunch arrival. The huge number of particles of the real bunch triggers the remaining "low voltage" channels. In the 2 plots the time scales are different: the t=0 ns point on plot (b) corresponds to 0.470 μs on the scope (plot (a)).

before the FAST tracker the produced secondaries would have arrived earlier than the main beam. The second hypothesis was the presence of a very long tail in the antiproton cloud, which was reaching the end wall much before the cloud core.
To make a long story short, it was found that the second hypothesis was the right one: if the vacuum valve placed just before the tracker (40 cm before the detector center) was closed, the intensity of these first particles on the detector increased and their arrival time was slightly reduced.
Unfortunately the diagnostic system of the Antiproton Decelerator is not designed to detect such a small fraction of the beam; moreover, all the experiments that are running (or have run) at AD are either not sensitive to single charged particles or are gated to start the data collection after the bunch arrival, so the presence of this "pre-bunch" antiprotons has been an unexpected discovery.
The only way to improve the situation was to change the timing of the extraction magnetic septum: the time of the septum ignition has been moved farther on, while monitoring the effects of these changes on the FAST detector. As soon as the septum starting time was moved, the hits on the detector started to move to later times. The delay has

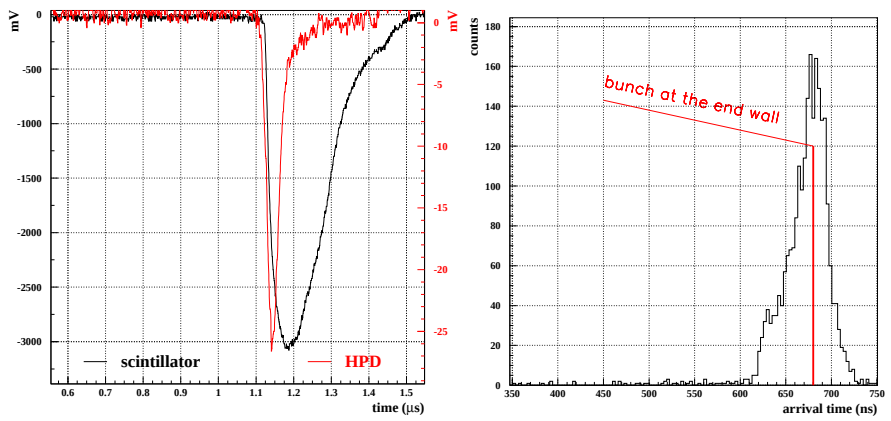

(a) (b)

Figure 4.19: (a) Scope tracks of the same two detectors used in Fig. 4.18a after the tuning of the extraction septum timing. No particles are detected by the high sensitivity scintillator until the main bunch arrives at the end wall. The delay of its edge with respect to the HPD track is due to the time of flight of the secondary particles back from the annihilation point and to the transit time inside the photomultiplier. (b) Arrival times on the FAST channels (collected over 10 bunches) after the septum adjustments, with the red line representing the time the bunch is expected to reach the end wall. Fibers which are hit before this time are due to wall annihilations.

been increased step by step until the signal on the scintillator and on the FAST detector started in correspondence of the main bunch peak. This condition has been obtained delaying the septum timing of 380 ns with respect to the starting position, which was considered optimal by the AD experts. The final results are shown in Fig. 4.19.

The tuning of the septum timing has been performed with the 0.9 μm mylar foil positioned in the first half of the detector, 10 cm from the entrance face of the tracker. As soon as the pre-bunch problem has been fixed, the first on target annihilation event has been detected: from the arrival time distributions of Fig. 4.20 the fibers which have been hit in the (highlighted) 10 ns window have been selected to be processed by the event reconstruction software. Fig. 4.21 shows the output of the software, with the presence of one vertex in the mylar target.

The beam has been optimized further on. Slow (fixed) scrapers have been inserted in the AD ring to obtain the twofold result of reducing the beam intensity by a factor 2 and of eliminating most of the beam halo.

Moreover, as far as the beam steering is concerned, an iterative procedure has been followed: first the beam was centered at best on the

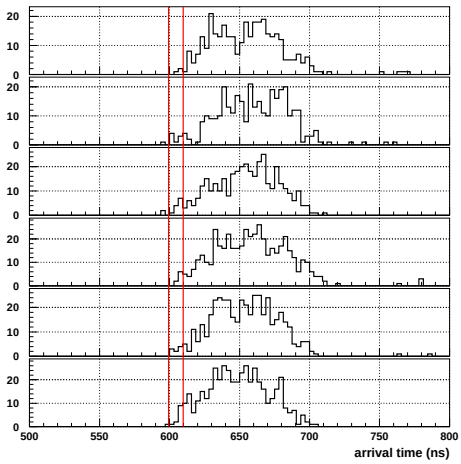

Figure 4.20: The arrival time distributions for one AD shot, layer by layer. The fibers hit inside the 10 ns time window identified by the vertical lines have been used for the event reconstruction of Fig. 4.21.

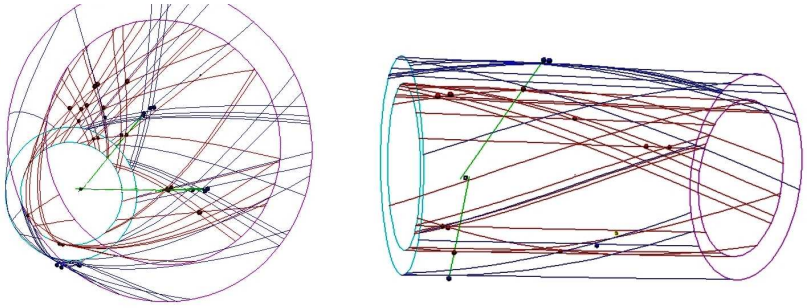

Figure 4.21: The first on target (namely a mylar foil) annihilation detected by the FAST tracker. Each track is reconstructed with one triangle on each shell. The hit fibers which are not involved in the reconstruction are either due to cross talk or should be associated to annihilations at earlier or (most probably) later times. In fact, the used fibers are not isolated in time, so that the selection is somehow arbitrary (Fig. 4.20).

MWPCs along the transfer line. Then using mostly the corrector magnets and the bending magnet (DZBH10), the beam has been moved in the horizontal and vertical directions trying to maximize the signal on the end wall counters and at the same time to minimize the hits at earlier times (due to wall annihilations) on the tracker fibers. With the same goal in mind, the last quadrupole doublet has been then tuned. When the best focusing was found, the correctors were used again, and so on until a satisfactory result was achieved.
Even if this beam tuning has been described here as a straightforward

process, actually it has been a time consuming trials and errors procedure, so that the whole setting up has required half of the available 10 days.
Since the whole overnight period is needed to move or change a target inside the vessel, the remaining 4 days have been divided as follows: one day for the empty vessel, for a background evaluation, and one day for each target (Nickel, Tin and Platinum). Since during the beam tuning the 0.9 μm mylar foil was inside the vessel (but not in the central position), information has been collected in this configuration too. A summary of the different running conditions is presented in Tab. 4.1.

Target	Thickness (nm)	mylar support (μm)	AD shots
empty	0	0	660
support only	0	0.9	690
Tin	412	0.9	1926
Nickel	267	0.9	1680
Platinum	169	0.9	1995

Table 4.1: Summary of the different target configurations and of the data collected for each configuration. The number of shots is mainly given by the AD duty cycle for the corresponding day.

4.2.4 Towards the cross section measurements

At the time of writing the data analysis of the 2007 data taking is only at its beginning. This section will report some of the preliminary results.
The hit time distributions of the tracker fibers for a typical AD shot with the empty vessel and with a Tin target in position are shown in Fig 4.22. With the target inserted, a lot of events at earlier times, when the main antiproton cloud is still far from the end wall, are generated; unfortunately these events are too many to be clearly isolated one from the other with a time selection.

Of course most of these detected particles are emitted by on wall annihilations, and constitute a background among which the interesting on target events have to be discovered. The situation is worse than foreseen, probably because of the presence of a rather wide beam halo, which increases the probability of on wall annihilation occurrence. Moreover, these annihilations will more likely arise towards the end of the small diameter vessel: in that region the fibers are placed in disordered bundles for the routing into the alignment masks, so each pion crossing will probably hit a large number of fibers corresponding to random regions on the detector cylinders.

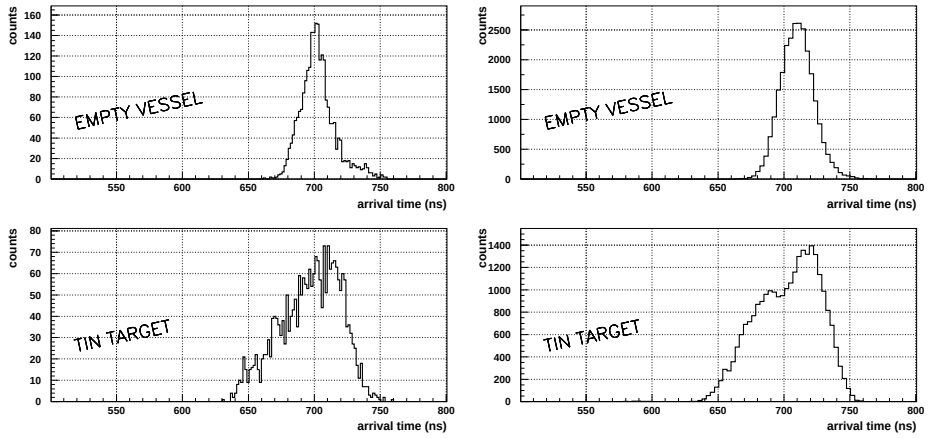

(a) (b)

Figure 4.22: (a) The arrival time distributions of all the FAST channels, for the empty vessel and for the Tin target (for a single AD bunch). In the former case all the antiprotons reach the end wall and there annihilate, while in the latter a few antiprotons can annihilate in the detector region, ∼80 ns before. (b) The same distributions, accumulated over ten random AD bunches, confirm the described behaviour.

To extract the annihilation events from the time distribution, the following procedure has been adopted: the first 30÷50 ns of the time distributions are sliced in 11 ns wide windows (this value can be, and eventually will be, tuned), 1.57 ns (LSB of the digital sample) apart one from the other, so that for each AD shot 20÷40 fibers sets are extracted. Each fiber set is analized independently by the event reconstruction software.
The algorithm searches for the intersections between fibers: three-fiber intersections (triangles) and unambiguous two-fiber crosses (i.e. groups in which none of the two fibers has other intersections beside the one considered) are used. At this point a track is drawn between each point on the outer shell and each point in the inner one, with the only condition that the ϕ coordinates of the points should be nearer than $\frac{\pi}{2}$ (to avoid to connect points on the opposite sides of the detector). Then the tracks are considered two by two, avoiding the couples with a point in common. The distance in space between every track couple is computed: if this distance is less than a given threshold, the point of minimum distance from the two lines (mean point of the distance-segment) is selected as a vertex candidate. If two vertices with a track in common are found, the three tracks are merged in a three pion vertex.

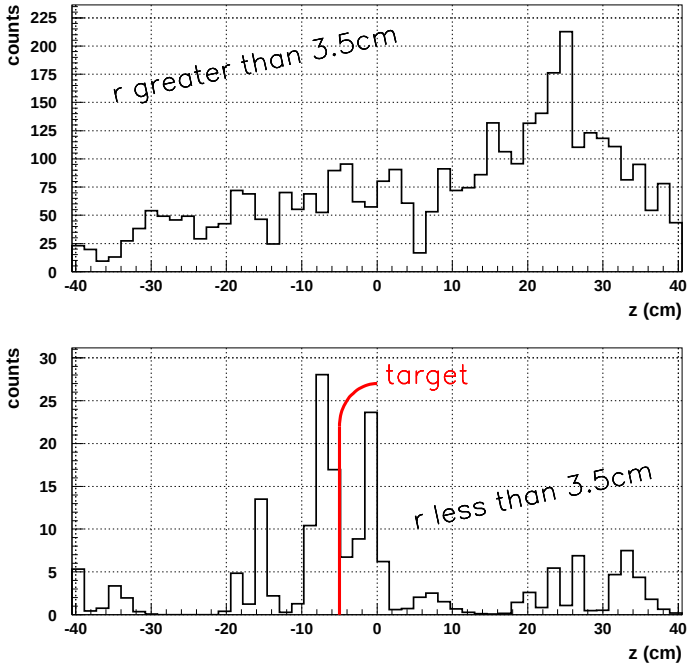

Figure 4.23: Distributions of the vertex position along z for different cuts: for events at a radius greater than 3.5 cm (wall events, top) and for the ones near the pipe axis (bottom). The position of the target is indicated.

A test has been performed to be sure that no evident bias or artifacts were introduced by the software itself. In principle, if the number of enlightened fibers is high (and this is the case), a software could reconstruct tracks and vertices just for a random combination of the hits. The situation has been simulated using random generated fiber hits, with the multiplicity of the real events; a few vertices are eventually found, especially at large radius, but their number is much smaller than in the real data case, so the effect can be treated as a background.
In the future, several improvements will be introduced in the algorithm: first of all, the fibers used for a track should not be used for another track in another time window, or, in other words, the program should compute one (or more) coherent set of tracks (vertices) for each shot. As a second issue, the time information of each fiber could be better exploited, using, instead of fix boundary time windows, a (gaussian or similar) function to weigh less and less the fibers at increasing distance from a (moving) reference time.

In the following some of the results that have been obtained by the current analysis software, despite the fact that the software itself is in an early development stage, are presented.

Fig. 4.23 shows the distribution of the positions of the reconstructed vertices along the beam axis for the data collected with the Tin target in place. If the vertices with a distance from the axis greater than 3.5 cm are selected, the distribution shows the expected asymmetry, consisting in a higher peak in the downstream region due to the scattering of the antiprotons on the target foil that steers a few antiprotons towards the pipe walls; for z greater than 25 cm the number of annihilations would still increase, but the reconstruction efficiency drops because of the end of the detector. As far as a quantitative analysis of these events is concerned, a further investigation is needed to clarify their origin. In fact, the Rutherford scattering alone would give a larger asymmetry in the distribution, with a ratio between the annihilations at $z>z_{target}$ and the ones at $z<z_{target}$ of the order[5] of 10 instead of the measured value of $\sim$2.5.
If the vertices near the axis are selected ($r<3.5$ cm) more than half of the events are located in the region where the target foil was positioned, namely a few cm before the detector center. Even if a background is present, which is due to either the combinatorial background at the fiber level or to the bad reconstructions that can happen in case of more simultaneous wall annihilations, the target peak can be easily identified.

As a further evidence of the presence of true on target annihilations, Fig. 4.24 shows the x-y distribution of the vertices for different regions along the z axis. While in the regions outside the target almost the whole number of events appears on the pipe walls (identified by the black circle), in the region of the target foil a few tens of events coming from the Tin layer (red circle) appears. These on target annihilations are about 20% of the wall ones.

[5] A montecarlo simulation with GEANT has been performed to compute this value, so that the geometry and the reconstruction efficiency have been taken into account.

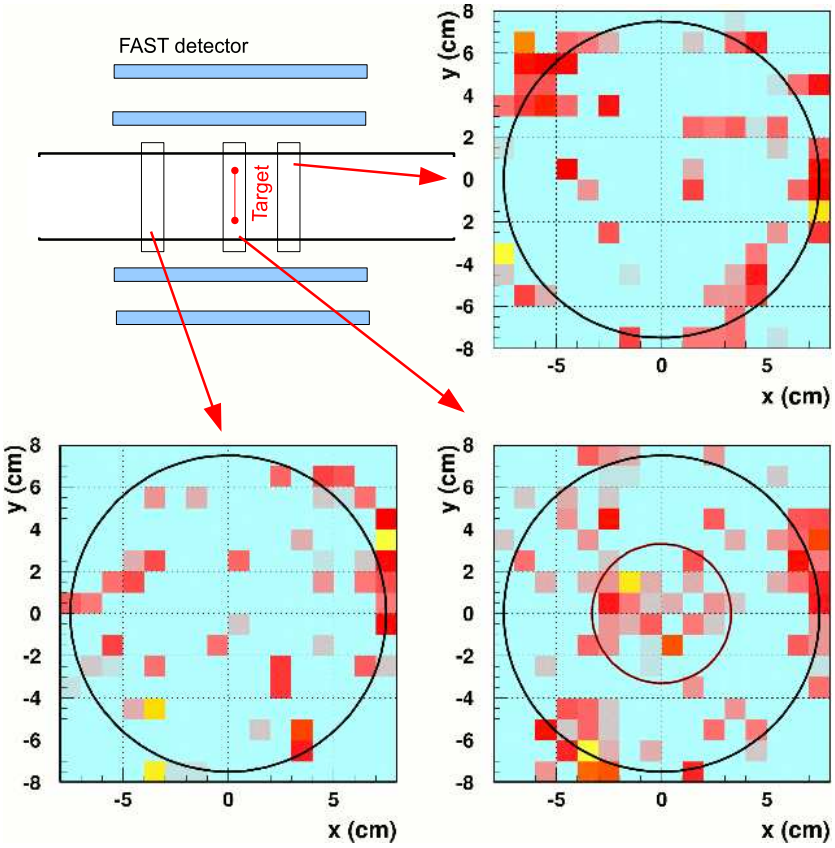

Figure 4.24: X-Y distributions of the reconstructed vertices, for the Tin run, at different positions along the beam pipe. The plot at the bottom right corner corresponds to the target region; the beam pipe is indicated by the black circle, while the red one bounds the target region.

Chapter 5

The FAST system in other physics fields

The electronics acquisition system developed for the FAST detector has been designed to be highly flexible so that it can be easily modified in case of a later detector upgrade. Moreover, given the short time available for the assembly and testing phases, a design with a strict hierarchical structure of relatively simple blocks was preferred, and this greatly improved the versatility of the system.
As a proof of this statement, this Chapter reports three different uses of the frontend board developed for the FAST tracker in different physics fields:

- A neutron detector with Time of Flight capabilities, to be used in radiotherapic environments
- A prototype based on a 2D GEM pad detector for high energy electron detection in a high radiation environment
- A beam profile monitor for high energy proton beams to study channeling effects in bent crystals.

For the first application only the digital part of the board is used, in particular the FPGA, while the other applications exploit all the board capabilities.

5.1 Sampling logic for a neutron Time of Flight

5.1.1 Neutrons from radiotherapic accelerators

Radiotherapic accelerators, if used in high energy (> 8 MeV) photon mode, produce a neutron flux due to the Giant Dipole Resonance of

high Z materials. A feasibility study in order to use this flux for neutron treatments such as the Boron Neutron Capture Therapy [80] is under way thanks to the PhoNeS (Photo Neutron Source) project [81]. The basic idea of the BNCT is the possibility to target a tumour with a carrier with elemental ^{10}B and to irradiate it with a thermal (energy <10 keV) neutron beam thus producing an α particle and a ^{7}Li nucleus, which, being high LET particles, deposit their whole energy in the cell, killing it.
The BNCT is not a widespread technique for several chemical/physical reasons: the need of high neutron fluxes ($> 10^8$ n cm^{-2}s^{-1}) in the thermal region, such as the ones produced in reactors and the lack of specificity of the Boron carriers. The development of a hospital neutron source, whose intensity and spectrum have to be verified, would be a great step forward on the BNCT way, arising hope on all the patients whose tumours are difficult to treat with the standard techniques (radiotheraphy, chemiotherapy, surgery): tumours located near vital organs (brain), extended tumours (liver, lung, stomach) and radioresistant tumours (melanoma).
In this framework a novel neutron detector has been developed to be used together with conventional neutron dosimetric methods [82][83]. The detector exploits the bunch structure of the beam; in medical Linacs the photons are emitted in short (3÷5 μs) bunches with a 100-300 Hz repetition rate, depending on the beam type, on the energy and on the dose rate. So, in the inter-bunch time no electrons or photons still survive and the neutrons (being slow, since the speed of a thermal neutron is 2.2 cm/μs) can be detected in a low background environment.
Spectral information can be obtained if the time elapsed from the neutron generation to the neutron arrival on the detector (Time of Flight) is recorded.

5.1.2 The detector

The sensitive volume of the detector is made of a cylindrical Bicron BC-454 boron loaded plastic scintillator with a 1 cm radius and a 5 mm height (Fig. 5.1a). A list of the scintillator most significant properties is reported in Tab. 5.1. The scintillator is doped with $(5.6 \times 10^{20}\ \frac{1}{\mathrm{cm}^3})$ ^{10}B atoms; a fraction of the impinging neutrons is captured by these atoms (σ=3836 barn at 0.025 eV). In this case the reaction ^{10}B(n,α)^{7}Li occurs, and an α particle of 1.47 MeV is emitted

together with a 850 keV Li ion[1]; in the 94% of the times a 480 keV γ is emitted too. The α particle stops in a few μm inside the detector, releasing its whole energy which is eventually transformed into light by the scintillator fluorine.

The $^{10}B(n,\alpha)^{7}Li$ is not the only reaction occurring when the scin-

Natural boron (weight)	5%
^{10}B atoms $\left(\frac{1}{cm^3}\right)$	5.6×10^{20}
Density	1.026 $\frac{g}{cm^3}$
Refractive Index	1.58
Softening point	60°C
Light output	∼8000 photons/MeV
Decay Time	2.2 ns
Wavelength of maximum emission	424 nm
Attenuation length	120 cm

Table 5.1: Bicron BC-454 boron loaded plastic scintillator properties. The light output is for a low energy transfer particle, while for a highly ionizing particle like the α emitted by Boron a lower output should be expected due to Birks' law [37]. The base is made of Polyvinyltoluene (from datasheet).

tillator is hit by a neutron beam. In fact fast neutrons have a high probability (e.g. $\sigma \simeq 3$ barn at 1 MeV) to hit one of the nuclei of the Hydrogen atoms of the material; if this happens part of the energy of the neutron is exchanged with the recoiling proton. The proton releases this energy inside the scintillator, resulting in a detectable signal. Nevertheless, since the energy of the proton cannot be larger than the neutron one, the signal is detected only if the energy of the neutron is larger than a given threshold (e.g. 500 keV): in our case such high energy neutrons cannot reach the detector in the time gate that is used for the sampling. In practice these fast neutrons arrive together with the main photon beam from the Linac and cannot be isolated.

The last reaction of interest for this work that occurs in the scintillator is the capture of slow neutrons from the Hydrogen nuclei ($H(n,\gamma)D$). The cross section is a factor 10^4 lower than the ^{10}B one, and the emitted γ, whose energy is 2.2 MeV, has a very low probability (at the percent level) to be detected in such a small scintillator by Compton effect. For these reasons the effect of this reaction can be considered small, if a great care is taken in placing the detector far from any material rich in Hydrogen (plastic, wood, water, etc.).

The scintillation light is readout by a 1" P30CW5 photomultiplier by

[1]The contribution of the latter is small, due to its lower energy and to the reduced light output for high linear energy transfer particles (Birks' law).

Electron Tubes, with integrated power supply.

The analog signal is sent to a CAEN mod. 84 NIM discriminator

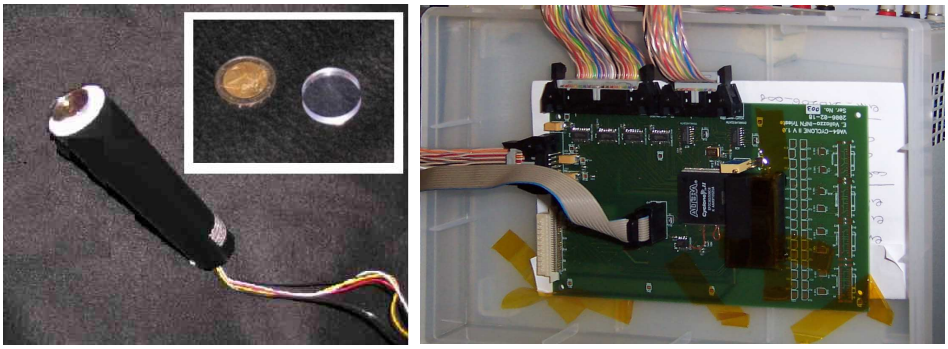

(a) (b)

Figure 5.1: (a) Picture of the BC-454 boron loaded scintillator assembled with the P30CW5 photomultiplier. (b) The prototype VA64TAP2.1 board, in the neutron ToF configuration. The discriminated signals from the detector reach the FPGA through the 16 pin flat cable, which also delivers the digital input needed for the readout.

(threshold -30 mV) which generates an output signal with a width of 200 ns. This signal is converted to the LVDS standard and sent to the prototype FAST board to be sampled by the Altera Cyclone 2 FPGA. Fig. 5.1b shows the board in the neutron ToF configuration with only the digital part connected.

For these measurements a 1 channel 64 kbit deep shift register has been implemented on the FPGA, corresponding to a 5 ms gate at a 12.5 MHz sampling frequency. The frequency corresponds to a period of 80 ns, that is small enough to ensure that the digital signal from the scintillator is detected always for two clock counts; in this way each neutron will appear as a couple of one (*1-1*) in the sampled bit stream. On the other side a faster clock would not increase the ToF performances[2], since the uncertainty on the neutron time of flight is limited by the $3 \div 5$ μs neutron generation time (the photon bunch length).

The sampled data are transferred to a VME I/O board and then to the PC through a SBS Bit3 bridge. The start of the integration gate is given by the Linac trigger, with a tunable delay in order to avoid the photon flux.

[2]In any case, a faster clock, together with a shorter discriminated signal, can be useful since it increases the maximum neutron rate the system can handle.

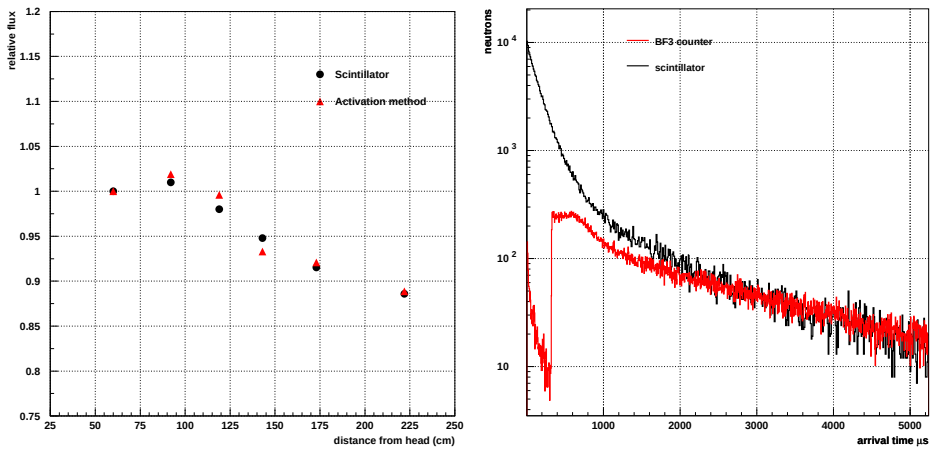

(a) (b)

Figure 5.2: (a) Relative neutron fluxes recorded by the prototype compared with the data obtained with Aluminum activation methods, for different distances from the Linac head. The plots are normalised to the first point. (b) Comparison of the arrival time distributions between the scintillator prototype and a BF_3 counter. The curves have been normalised in the tail region.

5.1.3 Flux measurements

The prototype detector works in a single neutron counting mode. To verify its capability to measure neutron fluxes, it has been positioned in different places inside the treatment room and the results have been compared with the values obtained with a standard reference method, that is the activation of Aluminum samples [84].
A Varian Clinac 1800CD/2100CD, delivering 400 M.U./min [3] of 18 MV photons[4], has been used; the Linac rate in this machine mode is 150 Hz.
The neutron flux has been measured increasing the distance from the accelerator head with no moderator in place and with the accelerator jaws stopping the main photon beam.
For each position the neutrons counted by the detector have been averaged over 1000 Linac bunches and the Aluminum samples have been irradiated for 125 s. A 2"×2" NaI(Tl) crystal and a standard spectroscopy chain with time recording capabilities have been used for the activity evaluation.
The results for the positions from 50 cm to 200 cm are shown in

[3] A Monitor Unit (M.U.) is a Linac output corresponding to a 1 cGy dose at the build-up region of a tissue equivalent phantom, placed at the isocentre.

[4] In radiotherapy the enegy of a γ beam is indicated by the accelerator voltage used for the primary electron beam, so a 18 MV photon beam is obtained by bremsstrahlung from 18 MeV electrons.

Fig. 5.2a; the data have been rescaled to the nearest point. The scintillator data are in good agreement with the Aluminum activation ones, the maximum difference being less than 2%. The moderator developed for the PhoNeS project, a 5 cm lead converter with a graphite shielding and a heavy water moderator, has been used to increase the slow neutron flux and to validate the prototype under high neutron fluxes. The detector measurements are in agreement with the activation data for all the experimental points; even if a proper calibration is still necessary to use the detector for an absolute flux measurement, it can be used as it is, to map the neutron flux fluctuations inside the treatment room.

5.1.4 Arrival time measurements

The arrival time distribution of the prototype has been compared to that of a neutron detector like the BF_3 counter[5]. The two detectors were placed in the same position and the BF_3 shaped signals were discriminated and acquired with the digital sampler. The results (Fig. 5.2b) show a good agreement for arrival times greater than 2 ms, while for shorter times the BF_3 counter is affected by a saturation effect due to its shaping time, greater than 10 μs, and its bigger size. The shape of the arrival time curve is the result of different contributions: the energy of the neutrons, the distance from the detector and the thermalization processes in the materials crossed by the neutron beam.
Two arrival time profiles recorded varying the distance from the moderator are shown in Fig. 5.3; shapes are clearly different, but to extract any spectral information from these data a careful parametrization and a comparison with simulation is still needed.

5.1.5 Montecarlo simulation

A montecarlo simulation has been developed, with the MCNP4B-GN toolkit [85], for two different purposes:

- Perform a correct evaluation of the flux measured with the activation method, the cross section of Aluminum having a $\frac{1}{v}$ energy dependence, where v is the neutron velocity
- Verify the agreement with the detected arrival time distribution.

To obtain the last result, an energy spectrum for the neutrons crossing the detector has been computed for every time slice in which the 5 ms

[5]By courtesy of Dipartimento di Energia Nucleare, Politecnico di Milano, Italy.

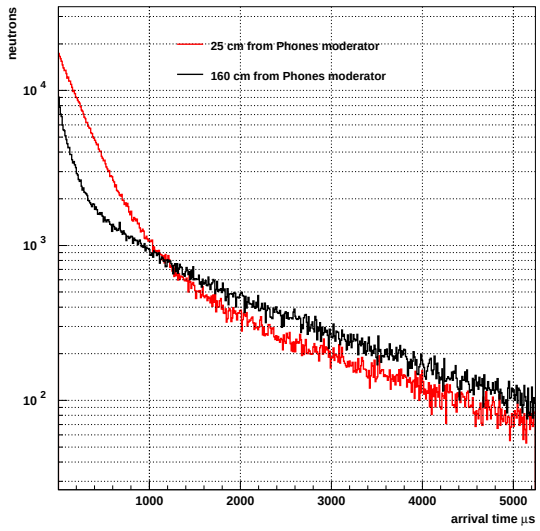

Figure 5.3: Comparison of the arrival time distributions for two detector positions, at 25 cm and 160 cm from the Linac head. Distributions are averaged over 500 bunches.

acquisition window has been divided; given the energy spectrum, the number of detected neutrons has been calculated taking into account the ^{10}B capture cross section energy dependence. The values for the cross section at the various energies are taken from the ENDF/EXFOR database [6].

The whole process starting from the primary photon beam is simulated, and most of the environment is included in the geometry. The obtained spectra, with the photon beam completely stopped by the jaws and with or without a PMMA[7] moderator, are shown in Fig. 5.4a; a small thickness of moderating material implies a major change on the fast-slow neutron ratio.

The results of the arrival time simulation are shown in Fig. 5.4b: the agreement with the experimental data is very good. This can be considered as a very accurate validation of the energy spectrum which has originated the time distribution (Fig. 5.4a). The results that have just been reported show that a system able to retrieve the time information of each neutron capture can be useful for both flux and energy spectrum measurements. The ASACUSA frontend board is not the only way to obtain this kind of information: for example oscilloscopes with a record length long enough to digitize a time window of a few milliseconds with a 100 ns resolution are nowaday available (although

[6]The Experimental Nuclear Reaction Data (EXFOR/CSISRS) contains an extensive compilation of experimental nuclear reaction data, based on more than 17000 experiments.

[7]PolyMethylMethAcrylate.

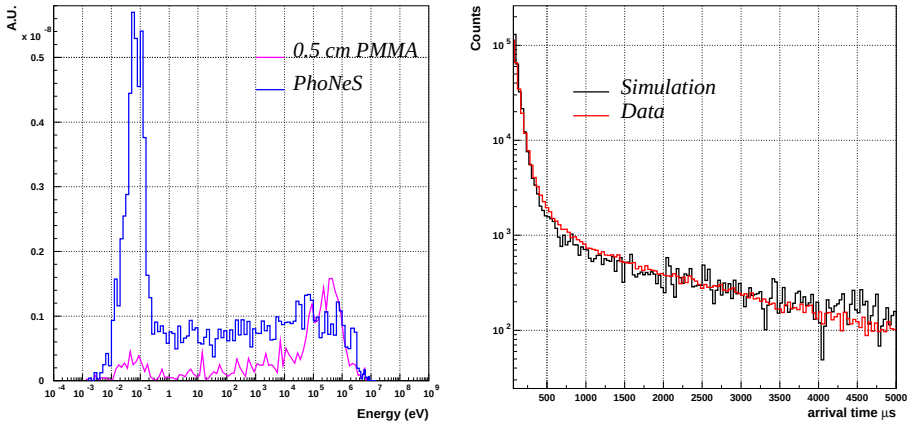

(a) (b)

Figure 5.4: (a) Neutron Spectra from the MCNP4B-GN simulation with a 5 cm PMMA moderator and with the PhoNeS prototype. (b) Comparison between the arrival time distribution measured by the prototype and the one extracted from the montecarlo, both obtained with the detector under a 5 cm PMMA moderator.

expensive). Anyway, the ASACUSA electronics, which is dedicated to the task, is compact, customizable and can be better integrated in a real time acquisition system.
Moreover, the ASACUSA electronics is well suited to the readout of a multichannel upgrade of the detector. The idea is to use boron loaded scintillating fibers, of small diameter (ø<1 mm) and short length (<1 cm), with a clear fiber used to transmit the light up to a 16 or 64 channel multianode PMT. In fact the board can be used as it is, with only a minor modification in the VHDL code. With respect to the bulk scintillator used in the present prototype a small fiber has the advantage to be almost insensitive to the photons which are produced by the neutron captures in the media surrounding the detector (mainly on the Hydrogen nuclei).
Each probe could be placed in a different position inside the treatment room, and could be inserted in moderator materials of various thicknesses. In this way a complete mapping of the neutron flux could be obtained with a single measurement and this would make the device an extremely useful tool for the study of the neutron production in a radiotherapic environment.

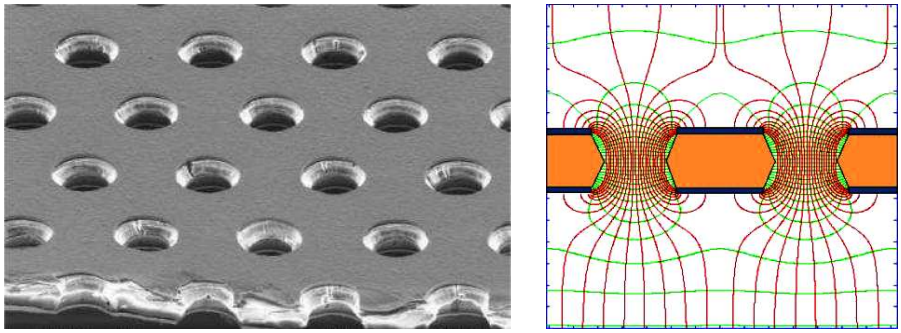

(a) (b)

Figure 5.5: (a) Microscope picture of a GEM foil. The hole diameter is 50 μm and the pitch is 140 μm. (b) Electric field lines inside a GEM hole: with voltages of the order of 500 V between the foil faces electric fields as high as 10 MV/m can be obtained.

5.2 VLSI readout of a GEM detector

5.2.1 The GEM detectors: principles and properties

A GEM (Gas Electron Multiplier) detector [86] is made of a very thin kapton foil ($\sim$50 μm), with a Copper deposit on each side, perforated with a high number (a typical value for the pitch is 140 μm) of holes, as shown in Fig. 5.5a: each hole has a biconical shape, with 50 μm and 70 μm of inner and outer diameter respectively. If the foil is placed in a gas mixture and a voltage difference (usually 350$\div$500 V) is applied between the two copper sides, each hole acts as an electron multiplication channel. In fact the high electric field inside the hole (Fig. 5.5b), that can reach 10 MV/m, gives rise to a multiplication process in the gas. Gains of the order of a few thousands can be reached with a single GEM foil: unfortunately in this case the discharge probability becomes very high [87].

For these reasons the double or triple GEM detectors have been developed; in these devices the GEM foils are assembled at a close distance with the help of insulating spacers, and the voltages between them are such that the electron exiting a GEM can be efficiently collected by the following one (Fig. 5.6). The foils are enclosed in two conductive planes, to provide the collecting drift field: the anode is commonly segmented, either in pads or strips, and connected to the readout electronics.

With a triple GEM, gains as high as $4{\cdot}10^4$ can be obtained, with a discharge probability (for each incoming particle) lower than 10^{-11} and with a $\sim$100% efficiency for the detection of minumum ionizing

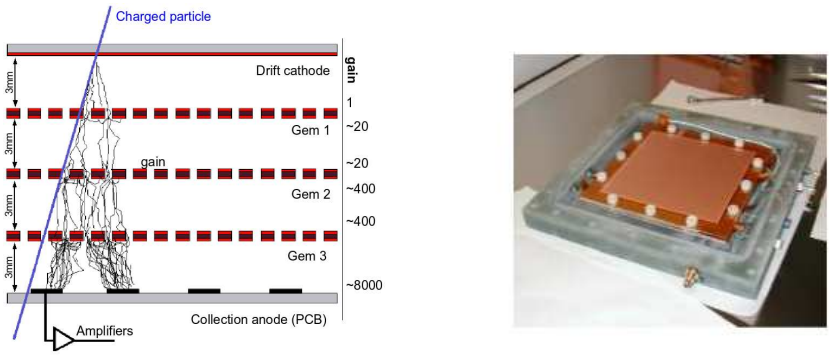

(a) (b)

Figure 5.6: (a) Scheme of a triple GEM detector. (b) A picture of the 10×10 cm^2 GEM detector tested with the ASACUSA frontend electronics.

particles [88]. Of course, since the GEMs are gas detectors, the parameters are influenced by the used gas mixture and by the environmental conditions as well.
Because of the small dead time and of the high radiation hardness, the triple GEM detectors can be used for tracking in high rate experiments; in particular these devices can represent a cheaper and effective solution compared to the silicon detectors if spatial resolutions in the range 100 μm$\div$5 mm are needed.
Moreover, the triple GEM can be optimised to obtain time resolutions better than 5 ns, so that it can be a promising candidate for high-rate charged particle triggering [89][90].
Since the GEM discovery in 1997, the technique has rapidly spread and is now being used, among the others, in the following experiments: LHCb [91], COMPASS [92] and TOTEM [93] at CERN, HERA-B [94] at DESY[8], and PHOENIX [95] at BNL[9].

5.2.2 The ASACUSA frontend board for the GEM readout

The readout of the GEM detectors in the running experiments have been accomplished by ASICs that have been developed for the silicon strip or MWPC readout. As an example, the COMPASS and TOTEM experiments are using the APV25, an analog pipeline ASIC built in 0.25 μm CMOS technology and developed for the CMS silicon microstrip tracker [96], which samples at 40 MHz the GEM (shaped)

[8]Deutsches Elektronen-SYnchrotron, Hamburg, Germany
[9]Brookhaven National Laboratories

signals. Its performances are very good as far as the efficiency and high rate capability are concerned [97][98], but it cannot provide a good time information or first level triggering.
In the last years a few ASICs have been developed specifically for the GEMs: a 32 channel readout chip for a GEM time projection chamber with a time over threshold logic is being developed at DESY [99]; an ASIC performing shaping, single threshold discrimination, dual-phase peak detection, timing detection and sparse readout with neighbour enabling is being studied at the Brookhaven National Laboratories for the same purpose [100] and a custom integrated circuit for GEM and RPC readout in a calorimetry context is being tested at the Fermi National Accelerator Laboratory [101]. Anyway, all these systems are still in a development phase and none is commercially available.
The VA64TAP2.1 ASIC, having a minimum operational threshold of $\sim$10 fC and a range of 160 fC for the input charge (Tab. 3.2), can be successfully used to perform a GEM readout; in fact the gain of a triple-GEM is of the order of a few 10^4, so a VA64 based electronics could be able to detect a signal if more than $4 \div 5$ primary ionizations occur in the ionization region (in fact a $\sim$10 fC threshold corresponds to $\sim$60000 e^-). Moreover the ASIC can exploit the high rate capability of the GEM detector: since each channel can sustain rates up to $\sim$1 MHz[10] and the discriminated outputs are completely independent, rates of tens of MHz on a (64 channels) detector are feasible. As far as the timing capabilities are concerned, the ASICs, when used for the scintillating fibers readout, can obtain a resolution of the order of 3 ns r.m.s. (see Sec. 4.1); in principle this value would be good enough to cope with the time resolution of the GEM detector. Anyway, since the timing performance depends on how large the pulse height fluctuations are (see Fig. 4.4), it is not possible to extend the fiber result without a new set of measurements.

5.2.3 Results at the Frascati BTF

A test run at the Frascati BTF has been held to verify the performances of the GEM–VA64TAP2.1 system: for this preliminary measurement the ASACUSA frontend board has been used. A custom cable to connect the scotchflex connector of the GEM detector PCB to the four ERNI connectors of the readout board has been built. Unfortunately in this procedure 24 channels of the ASIC were connected to ground, so that only 40 channels were available for the tests.

[10]The value of 2.5 MHz reported in Tab. 3.2 is measured with a periodic pulsing, while the rate for physical events distributed in time with a poissonian distribution is lower.

The GEM together with the readout electronics has been placed on

	bias (V)	ΔV (V)
cathode layer	3875	
GEM 1 top	2825	**440**
GEM 1 bottom	2385	
GEM 2 top	2035	**420**
GEM 2 bottom	1605	
GEM 3 top	905	**410**
GEM 3 bottom	495	
collecting anode	0	

Table 5.2: Voltage settings used for the triple GEM detector under test. The foils are numbered from top to bottom as in Fig. 5.6. The voltage drop across each GEM is indicated.

the BTF electron beam line, with the detector centered with the beam pipe axis; an analog readout mode has been used, with a timing for the hold signal similar to the one used with the fiber stereo prototype (e.g. ∼50 ns after the particle bunch). The beam line has been set to obtain 470 MeV electrons with low multiplicity: since the distribution of the number of the arriving particles is poissonian, some of the bunches were actually empty, half of them were made of a single particle, and the two (or more) particles occurrence was much suppressed.

In Tab. 5.2 the operating voltages that have been used during the measurements are indicated: each foil was biased with a 410÷440 V, corresponding to a total gain of about 3×10^4.

The pulse height and pull distributions obtained with the analog readout, for all the detector channels, are shown in Fig. 5.7. For the reasons explained in Sec. 3.3.1, a twofold cut on both the distributions has been used, so that the events with a pulse height greater than 300 ADC (arbitrary units) and a signal over noise greater than 10 have been selected. The so obtained bidimensional profile is shown in Fig. 5.8: despite the lack of some central channels, the beam profile is well reconstructed. Since no reference detector has been used, there is no way to measure the efficiency with precision. Anyway, the ratio between the single hit and two hit events on the GEM, which is ≃10, is compatible with the one measured, under similar beam conditions (same settings), with the (high efficiency) silicon detectors. This would suggest that the VA64TAP2.1 can provide a good efficiency if used for the readout of a GEM detector.

To test the time capability of the system a run with digital readout has been performed, using the signal from the linac as the start for the digital samplers on the FPGA. The results are reported in Fig. 5.9, where the time distribution is fitted with a gaussian curve

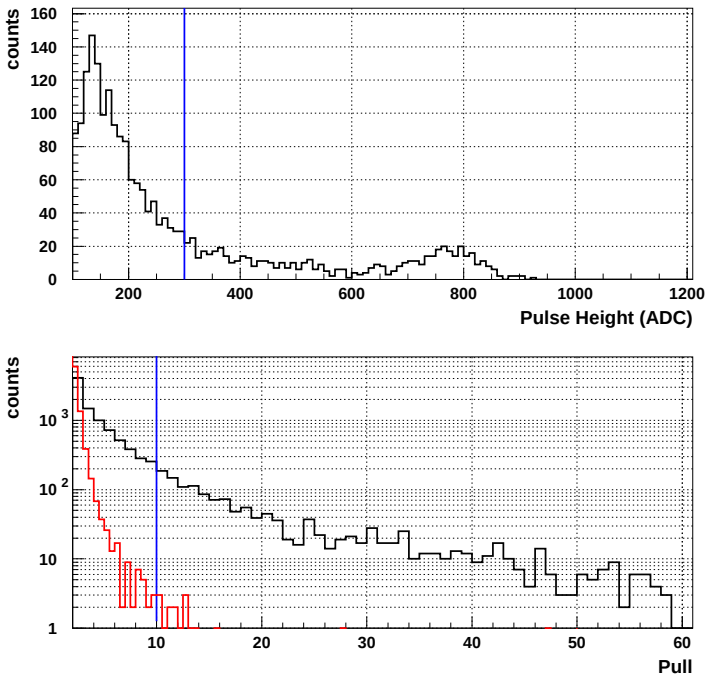

Figure 5.7: Pulse height (top) and pull (bottom) distributions for the GEM detector with the electron beam; in the pull case the noise distribution is superimposed in red. The cuts used for the event selection are indicated.

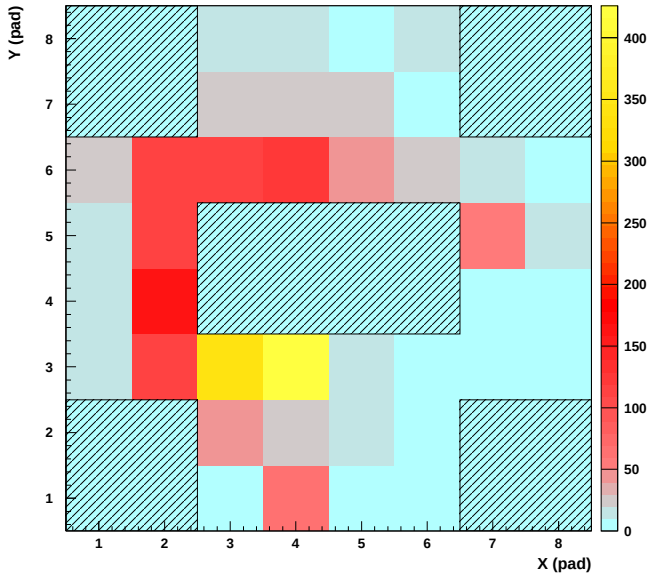

Figure 5.8: 2D profile obtained with the GEM detector. The regions of the detector which are not connected to the readout are indicated (hatching).

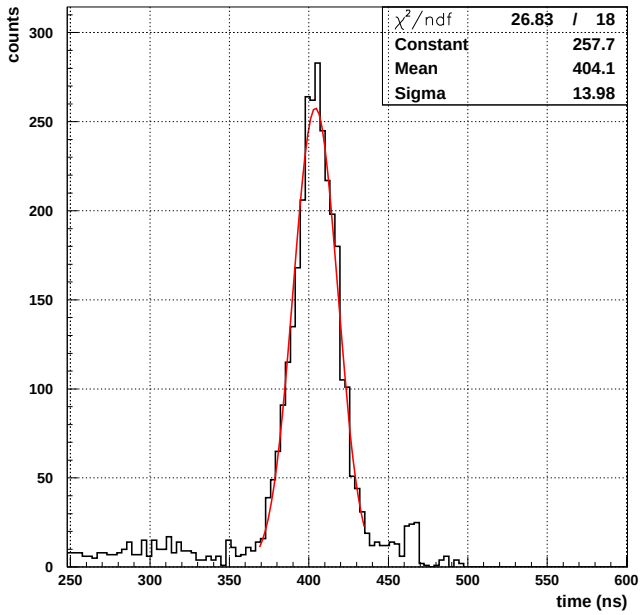

Figure 5.9: Time distribution of the GEM hits with the digital readout. A gaussian fit is superimposed and the sigma is 14 ns. The distribution takes into account also the time jitter of the beam particles with respect to the linac trigger.

whose width is σ =14 ns. This is not a direct measurement of the time resolution, since a non negligible contribution to the distribution width is given by the jitter of the arriving particles inside the bunch time width, which is of the order of 5÷10 ns r.m.s. (values from the linac specifications).

With no direct measurement of this time width, the resolution of the GEM system should be between 10 ns and 13 ns, which is competitive with the values obtained by other available integrated readout electronics (e.g. the APV25 ASIC), and can be suitable for most applications.

Future tests, with a more complete reference system for time and position, are scheduled, in particular to measure the efficiency of the system and its intrinsic timing capability. If the results are positive, a new electronics board based on the VA64TAP2.1 will be developed to ensure an optimal integration with the GEM detector.

5.3 The scintillating fiber profilometer

When a charged particle crosses a crystal with a direction parallel to that of the lattice planes, it can be captured by the lattice potential; in this case the medium atoms do not act any more as independent

scattering centers, and the particle is driven by the potential hole so that the energy loss is reduced. This effect, called channeling, appears as a higher transparency of a crystalline medium along certain directions [102], and has been experimentally seen both with ions and low energy particles during the '60s [103].
The H8-RD22 collaboration is testing the performances of different crystals at the CERN SPS H8 beam line, with 400 GeV/c protons, 200 GeV/c electrons and eventually with ions [106]. While the current investigations are performed with a high resolution Silicon tracking system, a fast and radiation hard beam profile detector could be useful to perform the measurements with a high particle flux, thus reducing the test time in case of a systematic scan of several crystals.
The scintillating fiber technology is a promising candidate for this task: to verify its feasibility, a prototype of a scintillating fiber profilometer has been developed and tested.

5.3.1 The profilometer assembly

The detector is composed of four fiber layers, grouped in 2 X-Y planes separated by 20 cm and each one is readout by two 64 channel R7600 Hamamatsu photomultipliers. A 5 mm thick Polyvinyl chloride (PVC) plate, with a 55×55 cm^2 area has been used as a support for each X-Y plane. The scintillating fibers (with ø=1 mm), identical to the ones used for the FAST tracker but without the white EMA, have been glued with a doublet ribbon configuration on the support plane (Fig. 5.10a): each plane is made of 128 fibers, thus covering a 6.4 cm width.
To make the fiber placement easier, the two fiber planes have been displaced on the two faces of the support; in other words an incoming particle would hit the X plane, cross the 5 mm PVC and then hit the Y fiber layer (Fig. 5.10b).

Two different fiber–PMT alignment mask configurations have been used for the two X-Y planes. In the first case, number 1 of Fig. 5.11a, for each PMT anode a rectangular hole of 1×2 mm^2 has been drilled, so that each channel houses exactly 2 fibers: this is the "standard" configuration. For the second case (number 2 in Fig. 5.11a), a more innovative design has been used: for each anode column a single slit has been drilled, having a width slightly larger than the fiber one. When the fibers are inserted they automatically arrange themselves in a staggered stack. In this way the one to one correspondence of the PMT channels with the fibers is lost, but the hit position is still a linear function of the channel with signal. The advantages of this method are twofold:

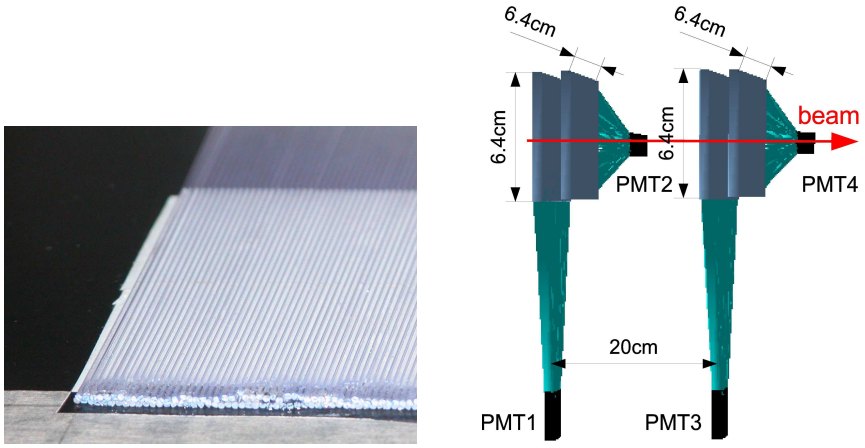

(a) (b)

Figure 5.10: (a) The scintillating fibers (ø=1 mm, no EMA, BCF-10 by Bicron) in the doublet ribbon configuration, glued onto the PVC support. (b) 3D schematic drawing of the four fiber planes composing the detector.

- The slit manufacturing is much easier and the fiber insertion is faster

- A wide and continuous range of fibers per channel can be achieved just changing the slit size: in a small slit two near fibers are roughly in column (∼2 fibers per anode), while increasing the slit size they become more and more off-axis (up to four fibers per anode). This allows to cover a wider area with a single PMT, of course at the expense of the spatial resolution.

For the slit width used in the profilometer assembly the 128 fibers fitted inside less than 7 columns, corresponding to 52 anodes (2.45 fibers per channel).

The photomultipliers have been aligned with the fiber mask with the help of two LEDs, embedded in the fiber plane, which enlightened the 2 anodes at the opposite corners. Once the PMTs have been fixed in the correct position, the two detector planes have been assembled together with 20 cm spacers. Two ASACUSA frontend boards, one per plane, and a repeater board have been fitted in the space between the two planes. The setup has been enveloped in a light tight plastic cover, so that only the repeater and the PMT high voltage connections were accessible.

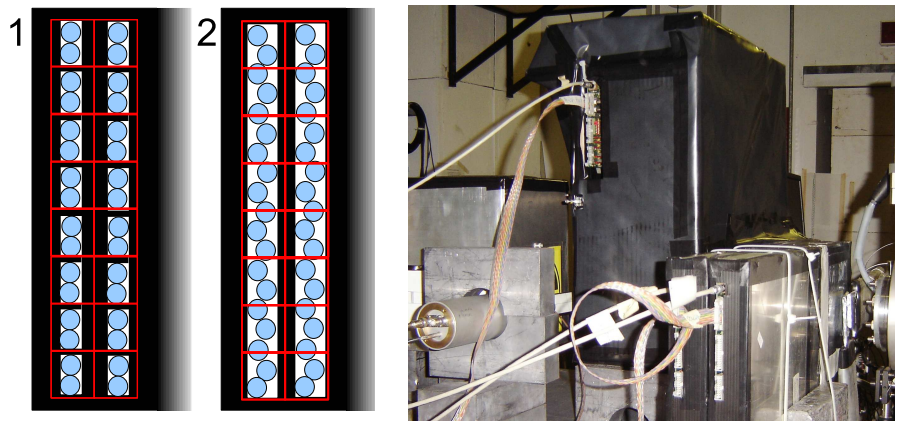

(a) (b)

Figure 5.11: (a) The two fiber mask configurations used for the two X-Y planes of the detector. The red squares show the anode zone, i.e. the 2×2 mm^2 anode area plus a ring that is half of the 0.3 mm anode spacing. (b) The complete detector (enclosed in the black box) under test at the Frascati Beam Test Facility. The beam, which comes from the pipe on the right, crosses the two Silicon detectors used as a reference (Aluminum boxes), hits first the profilometer and then the plastic scintillator used as a trigger (partially hidden).

5.3.2 The results at the Frascati BTF

The profilometer has been tested on the electron beam of the Frascati Beam Test Facility to characterise its resolution and efficiency figures. The reference silicon tracking system (described in Sec. 3.1.2) has been positioned just after the beam exit flange and the detector under test has been placed downstream (Fig. 5.11b). Since the multiple scattering of 500 MeV electrons crossing the 1 cm thick X-Y plane of the profilometer is not negligible, the evaluation of the spatial resolution using the silicon detector information is meaningful only for the first profilometer plane (in the beam direction). So, to measure the spatial resolution, two runs have been performed reversing the detector orientation.
The results are shown in Fig. 5.12. The transit point is the center of the channel if a single fiber is fired, and the mid point if two fibers are hit. The resolution values are significantly bigger than the expected digital resolution for both the planes of the detector, meaning that, at this scale, the error on the hit point determination is no more dominated by the channel pitch. Three other contributions have a major role: the multiple scattering effect, the uncertainty in the fiber positioning, and the absence of the EMA, that, while increasing the efficiency, allows some ligth to escape from the crossed fiber and to be

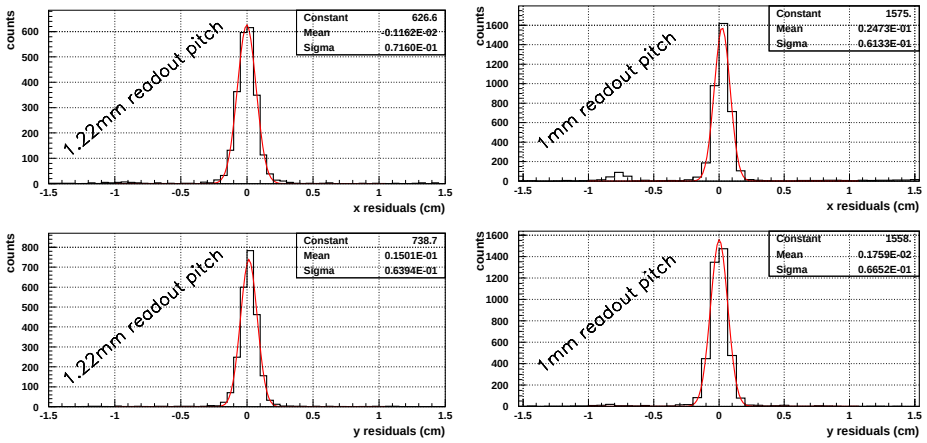

(a) (b)

Figure 5.12: (a) Residuals of the track reconstructed by the silicon detector, for the X-Y plane with the slit shaped alignment mask, that provides a 1.22 mm readout pitch. The resolution is (from the gaussian fits) σ_x=720 μm and σ_y=640 μm. (b) Same plot for the other X-Y plane, with 1 mm readout pitch. In average, a slightly better resolution (σ_x=610 μm and σ_y=670 μm) is obtained.

collected by another (but near) fiber.
One of the residual plots of Fig. 5.12, shows a second peak, accounting for a 5% of the events, at 8 mm distance from the main one: being this distance equal to the number of anodes of a column (8, in the 64 channel PMT) times the pitch (1 mm) this is certainly due to the cross talk.

As far as the efficiency is concerned, more than 99% of the tracks reconstructed by the silicon system have been detected by each plane of the fiber modules. This value greatly exceeds both the stereo prototype and the FAST tracker ones. Three possible reasons for this behaviour can be listed:

- The fiber length is smaller, 30 cm vs 70 cm
- No EMA is used, so the primary scintillating light exiting the fiber is not absorbed but enters in the neighbour fibers. As already shown, this effect does not worsen the resolution
- Fibers, being on a single plane, can be very closely packed thus avoiding dead spaces between them.

No efficiency loss has been measured for the X-Y stage with the slit masks, confirming that the dead area between two adjacent anodes is small, absorbing a very small light fraction.

5.3.3 Results on the SPS H8 beam line

The crystal under test was a 5 cm×2 mm silicon strip, with a thickness of 500 μm: the holder kept the silicon strip vertical, with the main bending radius perpendicular to the beam direction, so that the beam enters the 500 μm face. The plastic deformations given by the main bending produce a smaller curvature along the beam direction; with a main bending radius of the order of 1 m, deflection angles of $\sim$100 μrad can be obtained.
When a collimated beam (<1 mm in FWHM size, a few μrad in divergence) enters the crystal, three different situations can occur (Fig. 5.13a):

- Unperturbed beam: the angle with respect to the lattice planes is too big and the particles simply cross them. The only crystal effect is the multiple scattering on the silicon atoms, like in an amorphous material
- Channeling: the particles are almost aligned with the lattice planes at the entrance point: the potential barriers placed in correspondence of the planes themselves become channels in which the particles are confined. In this way, the beam is forced to follow the crystal bending. Since the effect has a small acceptance on the incoming divergence, with a real beam this process has an efficiency smaller than 100%
- Reflection: the beam is reflected by one of the crystal planes, whose potential barrier reflects the particle trajectories on the side opposite to channeling. The angle between the incoming and the reflected beam is smaller (by a factor 5$\div$10) than the channeling angle, that is the deviation angle induced by channeling.

The resolution of the fiber detector ($\sim$600 μm in the best case) is too low to detect the reflection of a single silicon strip (60 m×15 μrad= 900 μm). A multi strip device was also tested by the H8-RD22 collaboration: in fact, multiple crystals are the most promising option to obtain the deflection angles needed for a beam collimation system. The multi strip system was made of 8 crystals aligned in such a way that a particle which undergoes a reflection in the first strip enters the second one with the right angle for a second reflection and so on (Fig. 5.13b).
The detector was placed, on the SPS H8 beam line, 60 m downstream of the goniometer which controls the bent crystal holder rotation. The goniometer angle was moved in a 1200 μrad window around the starting point (pre-alignment position, which is found with a laser system),

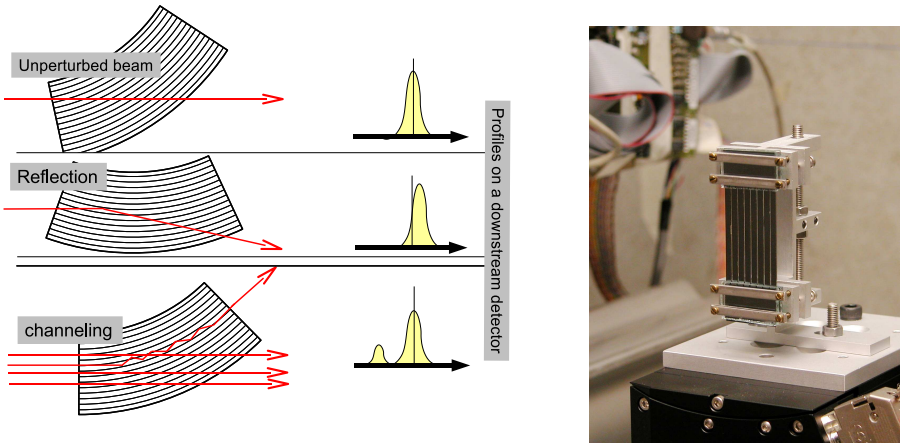

(a) (b)

Figure 5.13: (a) A particle crossing a bent crystal, depending on the angle between its trajectory and the crystal planes, undergoes channeling, reflection, or crosses with no interaction: the three situations give different results on a downstream profile detector. The angle scale is extremely enlarged, the real bending being of the order of 100 μrad. (b) The holder with 8 aligned bent crystals mounted on the goniometer on the SPS H8 beam line. Despite the 8 reflections, the deflection is still small (of the order of tens of microradians), so the crystals are placed 60 m upstream of the fiber detector.

and for each angular position a beam profile has been collected. The upstream silicon tracking system was used to select the particles that were really crossing the crystal (the beam size is larger than the strip cross section), to reduce the profile contribution of the undeflected beam.
The detector was readout in the analog mode, with the same DAQ chain described in Sec. 3.2.5: the system is capable of a maximum rate of a few kHz. While this rate is enough for the prototype characterization, in the future it could be increased at least by a factor 100 switching to the digital readout.
The 2D plot of Fig. 5.14, in which the profiles collected at different goniometer angles are summarized, shows clearly the presence of a $\sim$50 μrad reflected beam for the goniometer positions between 600$\div$800 μrad; the broad channeling peak is also visible.

To summarize, the tests on this prototype have demonstrated the feasibility of a scintillating fiber profilometer to be used for crystal channeling studies under high particle fluxes, preparing the way for a second detector that, with much smaller fibers (250 μm), will have the resolution needed to obtain physics results.

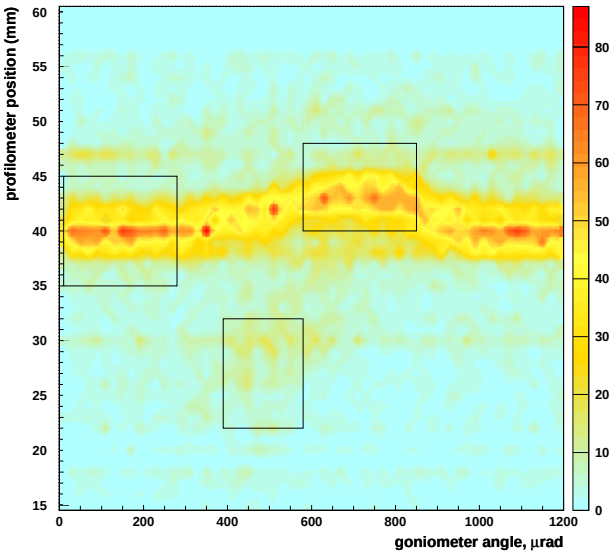

Figure 5.14: Beam profile as a function of the crystal angle set by the goniometer: at the beginning and at the end of the scan the profile is centered around 40 mm (left box), corresponding to the unperturbed beam, while in the region between 600÷800 μrad (right box) the whole beam is reflected by the crystals. The channeling peak is visible, although it is broaded, in the bottom square. One millimeter in the profile corresponds, at the detector distance, to 16 μrad, so the beam is bent, during the reflection, of $\sim$50 μrad.

Conclusions and outlooks

Antiproton-nucleus annihilation cross sections have been measured at very low antiproton momenta, down to 40 MeV/c, by the OBELIX experiment at the LEAR facility in the years 1992-1996: for the first time the behaviour of the annihilation rates has been investigated with high precision in a region where Coulomb attraction becomes of primary importance.
Surprisingly, it has been found that, at such low momentum, the $\bar{p}$-D and $\bar{p}$-He annihilation rates drop down to the $\bar{p}$-p level or even below it, contradicting the geometrical picture of the process which would suggest the increase of the annihilation cross section with the increase of the number of possible annihilating partners (i.e. the nucleons).
To understand the dynamics of the annihilation processes in this energy region, a new experiment, to be performed at the CERN Antiproton Decelerator, has been proposed in the framework of the ASACUSA collaboration.
To successfully exploit the high intensity $\bar{p}$ bunches of AD, which are $\sim$20 ns long, a novel vertex detector (FAST) with a time resolution of a few nanoseconds based on the scintillating fiber technology has been developed.
Several prototypes have been built and tested during the early phase of the detector development: modules with fiber diameters of 2 mm and 1 mm, with different PMT-fibers alignment masks, with or without extra mural absorber have been tested both with cosmic rays and with the electron beam of the Frascati Beam Test Facility.
The FAST detector has been designed taking into account both the experience collected with these prototypes and the results of a detailed montecarlo simulation, which has been useful to evaluate the tracking efficiency and the vertex resolution for the given geometry. Using the spatial resolution measured with the prototypes as an input for the montecarlo, values of 80%, 1.2 mm and 0.7 mm respectively for efficiency, the z and r resolution in the central region of the detector have been computed.
A custom electronics has been developed for the photomultiplier read-

out: it is based on the idea of using an ASIC for the analog signal (the VA64TAP2.1 by IDEAS) amplification and for the discrimination together with a fast FPGA for the digital time sampling of the discriminated data. The idea has been validated with the help of a prototype board which was tested with a fiber module prototype: a time resolution of 3.5 ns was measured with this system.
As a result, a frontend board able to readout 2 photomultipliers has been designed: 25 of these boards have been produced, assembled and successfully tested. To handle the 21 boards needed for the readout of the whole FAST tracker with a VME system a repeater board had to be developed. Multiplexing most of the digital signals and generating all the needed biases this board greatly simplifies the electronics system: each repeater handles 6 frontend boards and is driven by a VME I/O so that 4 I/Os, together with the power supplies and trigger system, are enough to accomplish the digital readout of the detector. An analog readout mode is also possible, using a pair of VME flash ADCs.
The FAST detector has been tested with cosmic rays during the commissioning phase. As far as the time resolution is concerned, positive results have been obtained, with a r.m.s. resolution of the order of 3 ns. On the other side, the spatial resolution figure of merit is more problematic: the non perfect fiber positioning on the cylindrical surface, together with the presence of cross talk, increases the width of the residual distribution by a factor $2 \div 3$ with respect to the planar prototype tested at the Frascati Beam Test Facility. When these numbers are translated, with the help of the montecarlo simulation, in terms of vertex spatial resolution, values of 18 mm (z) and 13.5 mm (r) are obtained. These values, despite being as large as twice the design specifications, still allow an efficient separation between target and wall annihilations.
The electronics has proved to work very efficiently during all the commissioning and physics runs, with a negligible noise count rate, completely fulfilling the design specifications.
Given the high flexibility of the frontend electronics, it has been successfully applied to physics fields completely different from the one it was developed for: in Medical Physics, allowing a Time of Flight Neutron detection in a radiotherapic environment, for the readout of a GEM pad detector and of a beam profile monitor with a large energy range and high rate capabilities.
As an example, in the case of the neutron ToF detector the advantage of this kind of integrated electronics will allow to build a real time neutron spectrometer/dosimeter which will able to retrieve, in a short time, the most complete information on the neutrons emitted by a

radiotherapy Linac, greatly overcoming all the traditional detectors. Two data takings have been held: the firs one (September 2006) hasn't allowed to collect any physics events because of several beam problems. A consistent part of the June 2007 data taking too has been devoted to the tuning of the beam and in particular to find a solution for the early antiproton arrival that saturated the tracker long before the main bunch arrival. When a reasonably good working condition was found, data have been collected for the various target nuclei.
The very high number of background events, due to the Rutherford scattering on the target, makes the time selection for the annihilation events difficult and somehow arbitrary, since a continuum of new hit fibers appears, as time goes on, on the detector. Anyway, with a fiber selection based on fixed width time windows it is possible to reconstruct tracks whose origin is either on the walls or (less frequently) on the target fiducial volume. A preliminary analysis of the vertex distribution, based on a simple automatic time selection, shows that an excess of annihilations is present in the target region, with a statistical significance over the background.
In the next future most of the efforts will be dedicated to a deeper data analysis which would allow to extract an estimation for the annihilation cross section on the target nuclei used during the 2007 data taking (Ni, Sn, Pt). Moreover, the analysis will provide useful information to tune the experimental setup for the 2008 run.
In the future, from the experimental point of view, the work has to be focused on three main aspects:

- The fiber misplacement problem has to be investigated and solved; a better knowledge of the fiber position, besides improving the spatial resolution, will allow a better rejection of the ghost hits induced by the cross talk effect. This can be done, with no interventions on the detector itself, through a beam test performed with high energy particles (to avoid multiple scattering) and a reference tracking system (to reconstruct the tracks with a very high precision)

- The dynamics of the antiproton beam in the apparatus has to be intensively studied, with the help of montecarlo simulations, in order to find the best experimental setup in terms of background reduction

- A (removable) monitor for the antiproton beam has to be developed to be able to center and focus the beam in an ideal way for the cross section measurement.

These improvements will definitively allow to measure the annihilation rates for different nuclei with the needed statistics.
With the 5 MeV antiproton line no more available after 2008, the detector will be moved, with little modification in the electronics, on the beam line after the MUSASHI decelerator, which can provide a $\sim$1 keV antiproton beam so it will be possible, for the first time, to study the nuclear processes in an energy scale comparable with that of atomic capture processes.

Appendix A

An apparatus for $\bar{p}$ studies: the OBELIX detector

Most of the annihilation cross sections discussed in Sec. 1.3 have been measured by the OBELIX collaboration. In this Appendix the experimental apparatus will be described and an example of cross section measurement, from both the experimental and analysis points of view, will be reported.
The OBELIX apparatus consisted in a magnetic spectrometer that operated at the Low Energy Antiproton Ring facility at CERN, in the 1991-1997 period. The goal of the experiment was the study of low-energy $\bar{p}$ and $\bar{n}$ annihilations on nucleons and nuclei, with the main purpose of investigating, with high statistics, the meson spectroscopy and the dynamics of the annihilation processes.
The layout of the OBELIX spectrometer is shown in Fig. A.1; the apparatus had a cylindrical symmetry and its central detectors operated in a 0.5 T magnetic field that was provided by the Open Axial Field Magnet which had previously been used for other experiments at the CERN ISR. A detailed description of the detector can be found in [107][108].
The apparatus was composed of the following subdetectors:

- The Spiral Projection Chamber (SPC), an imaging vertex detector with three-dimensional readout for charged tracks and X-ray detection
- The Time-of-Flight (ToF) system which was composed of two cylindrical barrels (18 cm and 136 cm of radius respectively) of plastic scintillator tiles (30 for the inner, 84 for the outer). A time resolution of $\sim$800 ps could be achieved by the system
- The Jet Drift Chamber (JDC) for tracking and for particle identification through dE/dx measurements. The 3280 wires of the

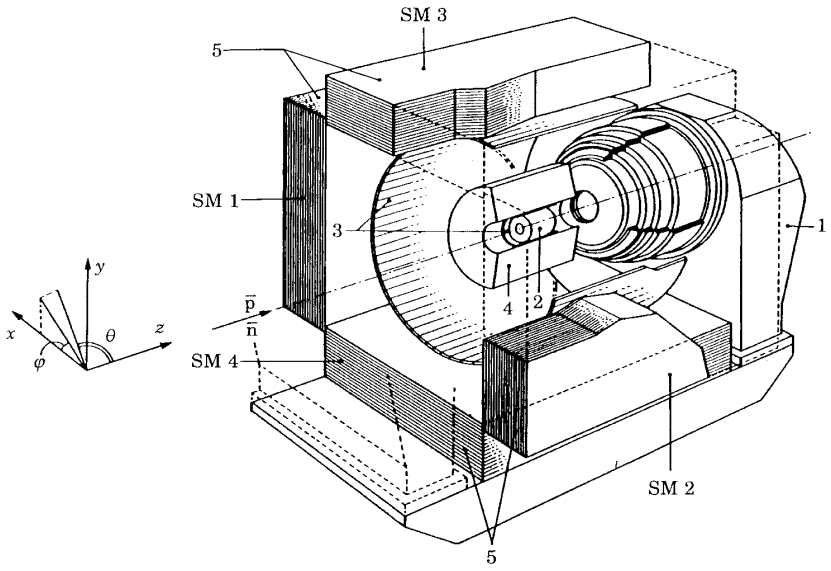

Figure A.1: Scheme of the OBELIX apparatus. The following subsystems are shown in the picture: (1) Open Axial Field Magnet; (2) Spiral Projection Chamber; (3) Time-of-Flight System; (4) Jet Drift Chamber; (5) Electromagnetic Calorimeter (SM1 to SM4). From [107]

chamber were readout by flash analog to digital converters. The spatial resolution of the chamber was σ_z=12 mm and σ_r=200 μm, while the momentum resolution (at 0.5 T) was measured to be 3.5% at 928 MeV/c

- The High-Angular-Resolution Gamma Detector (HARGD). It is a calorimeter system made of 4 modules (SM1-SM4). Each module is composed of 3×4 m^2 3 mm thick lead converter foils and limited streamer tubes acting as active medium. Twenty converter layers, for a total of $\sim$10 radiation lengths, were present.

The apparatus allowed the use of different targets: a liquid Hydrogen target, a gaseous Hydrogen target at room temperature and pressure and also a low pressure target (down to 30 mbar). The molecular Hydrogen could also be replaced by Deuterium.
The detector also offered the possibility to study antineutron interactions: the $\bar{n}$ beam was produced by charge exchange in a liquid Hydrogen target (positioned 2 m upstream with respect to the centre of the OBELIX detector). The efficiency of the $\bar{p}$ to $\bar{n}$ conversion process was of the order of 10^{-4}.

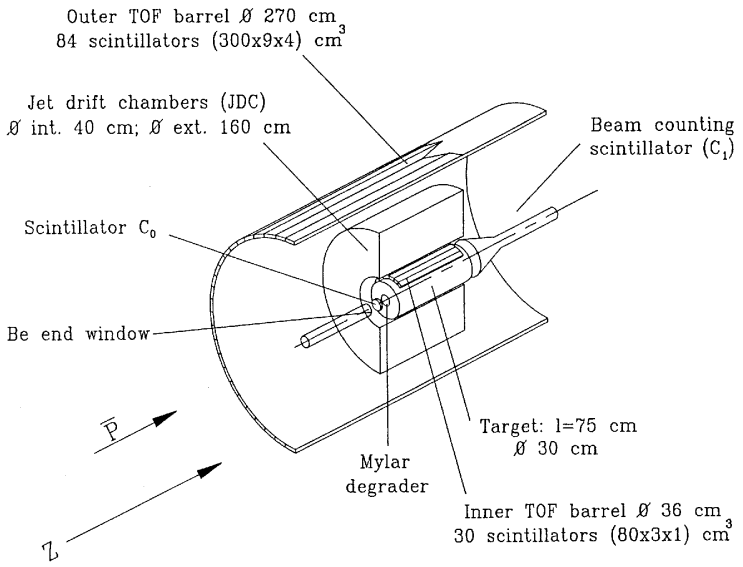

Figure A.2: The subset of the OBELIX detectors used for the measurement of the $\bar{p}$-p and $\bar{p}$-A annihilation cross sections. The Spiral Projection Chamber was replaced by a 70 cm long Aluminum vessel with a 30 cm diameter, containing the gaseous targets at variable pressures.

For the measurement of the $\bar{p}$-p and $\bar{p}$-A annihilation cross sections, only a subset of the OBELIX apparatus was used. In Fig. A.2 a sketch of this subset of detectors is shown. In particular, the Spiral Projection Chamber was substituted by a large cylindrical Aluminum tank containing the gaseous targets at variable pressure, while the Jet Drift Chamber was used as a tracking device for the reconstruction of the annihilations vertices and the ToF system was used to record the time at which each annihilation occurred with respect to the start time given by the thin scintillator detector (C_0 in Fig. A.2). The experimental procedure for the measurement of the annihilation cross section is described in detail in [109].
The antiproton beam coming from the LEAR machine, with a momentum of 201 MeV/c or 105 MeV/c depending on the interesting momentum range, crossed the 100 μm Beryllium window of the beam pipe, the scintillator counter C_0 (500 μm for 201 MeV/c, 80 μm for 105 MeV/c) and its enclosure (6 μm of mylar and 13 μm of Aluminum), a few centimeters of air and the Aluminum foil of the target vessel entrance window. These materials were acting as degraders, lowering the energy: the energy of interest was reached adding or removing calibrated mylar foils.

The target vessel was filled with gaseous targets at different pressures: higher than the atmospheric one for the data at 201 MeV/c beam momentum, to increase the number of in flight annihilations, and lower than the atmospheric pressure for the data at 105 MeV/c beam momentum. This last condition was needed to allow the low energy incident antiprotons to reach the end wall in absence of in flight interactions.
Essentially, the annihilation cross sections were measured by counting the number of in flight annihilations into charged products and comparing this value with the number of $\bar{p}$s crossing the target without any interaction and annihilating at rest, near or upon the end wall of the vessel.
The ToF of the annihilation events was used, as far as the trigger is concerned, to select a time window in which "interesting" events would occur: in case of a ToF between the start of the C_0 scintillator and a time corresponding to the whole travel up to the end wall, the data from the Jet Drift Chambers were recorded.
These data allowed the reconstruction of the different tracks and of the vertex coordinates of the annihilation events with an uncertainty on the determination of the coordinates of about 1.0 cm in the z direction and about $2 \div 3$ mm in x and y.
The antiprotons crossing the target without interacting were counted, detecting the charged products of the annihilations, with a system composed of the same scintillator barrel used for the ToF and of the additional scintillator disc C_1, placed near the end of the target.

If the z coordinate of the reconstructed vertices (after a r<10 cm cut) is plotted as a function of the annihilation time (Fig. A.3), the in flight annihilations can be easily separated from the annihilations at rest due to the antiprotons which have lost most of their energy in the degraders and so stop inside the target. Moreover, the slope of the plot z (vertex coordinate) vs. t (annihilation time) can be used to compute the average momentum of the $\bar{p}$ beam. Since the $\bar{p}$s lose energy inside the target, for the lowest initial energies the particle speed changes with z and the momentum has to be computed inside small slices in the z direction.
A description of the technique that has been used to extract the number of in flight annihilations inside the fiducial volume taking into account all the possible contributions from the background is beyond the goals of this Appendix; a detailed explanation can be found in [109].
Once the number of events N_{event} is correctly computed, the total annihilation cross section σ_{ann} can be obtained with the following for-

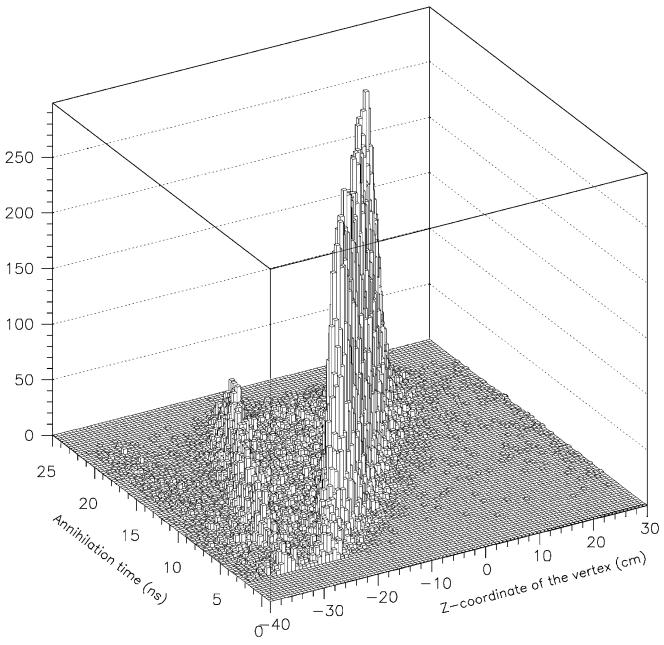

Figure A.3: 2D plot of the annihilation time vs. the vertex z coordinate, for data at 105 MeV/c with no mylar degrader. Vertices with r>10 cm have been rejected. The vessel entrance window is at z≃-40 cm. Two categories of events can be identified: the in flight annihilations (high peak), and the annihilations at rest given by the antiprotons that, being in the lower tails of the momentum distribution, stop inside the target (lower peak near the time axis).

mula:

$$\sigma_{ann} = \frac{N_{event}}{N_c N_{\bar{p}} \rho \frac{N_A}{M} l \epsilon_{rec}} \tag{A.1}$$

where $N_{\bar{p}}$ is the number of antiprotons crossing the region of interest, ρ is the density of the target at the given pressure, $\frac{N_A}{M}$ the number of molecules for one gram of gas, N_c the term which accounts for the number of scattering centers per molecule (e.g. $N_c = 2$ for H_2), l is the length of the fiducial volume and ϵ_{rec} the reconstruction efficiency, which has to take into account also the annihilation in the neutral pions channel, impossible to detect with the apparatus.

Appendix B

The FAST DAQ software

For a modern detector, which, like the FAST tracker, has a large number of channels, the data acquisition software is a fundamental part of the experimental apparatus.
An experiment DAQ has to perform a very high number of operations (for example read/write accesses to the VME bus) in the correct order; it has to be highly flexible to cope with all the possible hardware modifications, it should give to the user some sort of feedback on the collected data (online monitoring) and, more important, it has to perform these tasks as fast as possible. For example, in the FAST case, the program has to transfer almost 1.5 Mbit of data from the frontend FPGAs to the computer, to store the data and to set the hardware for the next shot in much less than 1 s, which is the time between two consecutive shots (for the 6 bunches of each AD cycle).
For these reasons, the FAST data acquisition software, working under Scientific Linux 3.5[1], is written in C and makes use of a low level driver, written as a kernel module, for the SBS PCI [2] board that provides the link with the VME bus. Moreover care has been put in avoiding that the tasks of secondary importance, like those needed for the monitor system steal computing power and memory resources to the main readout cycle.
While some global run-time parameter, like the addresses of the VME boards and other hardware specific settings, can be modified editing a configuration file, most of the user operations can be performed through a graphical user interface (GUI). This interface, that is shown in Fig. B.1, is written in Tcl-Tk[3], and is divided in four parts:

- The control window, that allows to perform the standard oper-

[1] *http://linux.web.cern.ch/linux/scientific3/*
[2] The Peripheral Component Interconnect standard specifies a computer bus for attaching peripheral devices to a computer motherboard
[3] Tcl (Tool Command Language) is a dynamic programming language and Tk is its graphical user interface toolkit *http://www.tcl.tk/*

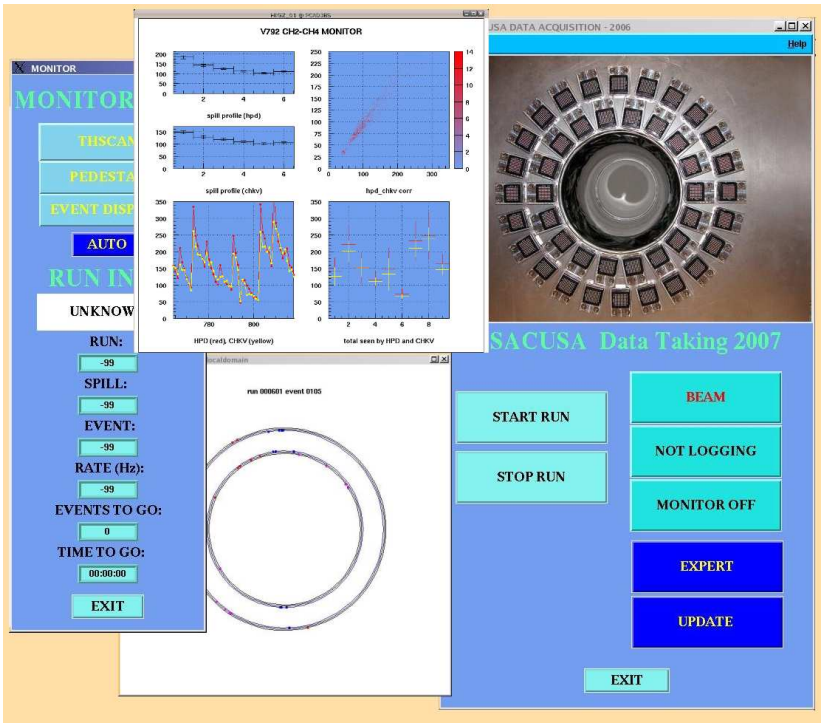

Figure B.1: Snapshot of the data acquisition software, where the main control panel (right), the monitor panel (left), the monitor graphical windows (bottom-center) for the fiber tracker and the graphical windows used for the online evaluation of the beam intensity (top-center) are shown.

ations like starting and stopping the run, selecting the analog or the digital readout mode, choosing whether to save or not an output file and finally turning on and off the monitor and expert windows

- The monitor window, which shows a list of useful running parameters (like bunch number and time information) and allows to select the histogram to be plotted on the (separate) HIGZ[4] window. The following data can be plotted: cumulative and event by event time profiles, cumulative spatial hit distribution, pedestal and rms values

- The expert window, opened upon request from the control window, which allows to perform dedicated tasks like pedestal acquisition, threshold scan and continuous mode (for debugging). These operations should be rarely performed, and most of them

[4]High Level Interface to Graphics and Zebra, see CERN Program Library Long Writeups Q120 and Y251

```
*****************************************************************************
* Ntuple ID = 1       Entries = 61         New Ntuple                       *
*****************************************************************************
* Var numb * Type * Packing *     Range     *  Block    *  Name              *
*****************************************************************************
*       1  * I*4  *         *               * ASANTUPR * IEVENT
*       2  * I*4  *         *               * ASANTUPR * ITIME
*       3  * I*4  *         *               * ASANTUPR * IATIME
*       4  * I*4  *         *               * ASANTUPR * ISPILL
*       5  * I*4  *         *               * ASANTUPR * IRAW_DATA(16,64,2,6,4)
*       6  * I*4  *         *               * ASANTUPR * IRAW_ADC(32)
*****************************************************************************
*  Block   *  Entries  * Unpacked * Packed *   Packing Factor                 *
*****************************************************************************
* ASANTUPR *  61       * 196752   * 196752 *       1.000                     *
* Total    *    ---    * 196752   * 196752 *       1.000                     *
*****************************************************************************
* Blocks = 1          Variables = 6          Columns = 49188                *
*****************************************************************************
```

Figure B.2: Header of the ntuple used by the DAQ software to store the collected data. It contains the general information on the run such as the absolute time and the trigger number; the `IRAW_DATA` array stores the information from the scintillating fibers while the `IRAW_ADC` variable contains the beam intensity data acquired by the CAEN V792 QDC reading the HPD and the Cherenkov detector.

need some hardware intervention, so they have been grouped in a separate "expert" window to avoid accidental use. It is also possible to modify the global thresholds, acting on the repeater DACs

- The intensity monitor, a separate HIGZ window showing a list of information on the intensity recorded, during the last AD cycles, by the two beam counters placed near the end wall (the HPD and the Cherenkov detectors). It shows the average value of the 6 bunches of the AD cycle, the last 50 shots, a scatter plot to check the level of correlation between the two detectors and the average intensity for the last ten AD cycles.

The monitor capabilities have been extremely useful, in particular during the beam tuning phase, because they gave an immediate feedback about the machine setting effects in a much faster way with respect to the offline analysis.

The data are saved as a PAW ntuple, whose header is shown in Fig. B.2: the information from the fiber tracker are stored, for each trigger event, in the `IRAW_DATA(`X_1`,`X_2`,`X_3`,`X_4`,`X_5`)` 5-dimensional array. The last three indices of the array define the FPGA (and thus the photomultiplier) of interest, specifying the repeater (X_5), the frontend board position on the repeater (X_4) and finally the FPGA on the frontend board (X_3). X_2 selects the channel of the PMT, in the Hamamatsu numbering convention (as shown in Fig. 2.8). The 512 sampled bits of each channel (each one corresponding to a 1.57 ns time slice) are divided in 16 groups of 32 bit each, so that X_1 specifies the group number, and the value of `IRAW_DATA()` is the (signed) integer result-

ing from the translation of the 32 sampled bits.
This solution allows the storage of a big number of sampled bits in a structure relatively easy to address; nevertheless, since no compression is applied, the size of the output file, corresponding to the total sampled bits (1.5 Mbit per trigger), is rather large. This is not a problem with the low repetition rate of the AD machine; anyway, for an application with a higher rate, simple data reduction methods could be applied easily, for example specifying, in the bit flow, the beginning of each train of 1s and its length (see Fig. 3.10). Each run is saved as a different file, and if the ntuple reaches 100 events the corresponding file is closed and a new ntuple is opened as a following file with an automatic naming system that avoids any human error.

List of acronyms

AA	Antiproton Accumulator
AC	Antiproton Collector
AD	Antiproton Decelerator
ADC	Analog to Digital Converter, also stands for Analog to Digital Converter unit
ALPHA	Antihydrogen Laser PHysics Apparatus
APD	Avalanche PhotoDiode
ASACUSA	Atomic Spectroscopy And Collisions Using Slow Antiprotons
ASIC	Application Specific Integrated Circuit
ASTERIX	Antiproton STop Experiment with tRIgger on X-rays
ATHENA	AnTiHydrogEN Apparatus
ATRAP	Antiproton TRAP
BNCT	Boron Neutron Capture Therapy
BNL	Brookhaven National Laboratories
BTF	Frascati INFN National Laboratories Beam Test Facility
CBAR	Crystal BARrel detector
CCD	Charge-Coupled Device
CERN	European Center for Nuclear Research
CFT	Central Fiber Tracking detector of the D0 experiment
CMOS	Complementary Metal Oxide Semiconductor
DAC	Digital to Analog Converter
DAQ	Digital AcQuisition system
DC	Direct Current
DESY	Deutsches Elektronen-SYnchrotron
ECL	Emitter Coupled Logic
EMA	Extra Mural Absorber
ENC	Equivalent Noise Charge, expressed in number of electrons
ENDF	Evaluated Nuclear Data File
ERNI	ERNI Electronics, Inc., USA
EXFOR	Experimental Nuclear Reaction Database
FAST	Fiber Antiproton Scintillating Tracker, the subject of this work
FLAIR	Facility for Low-energy Antiproton and Ion Research

FNAL	Fermi National Accelerator Laboratory
FPGA	Field Programmable Gate Array
FR4	Flame Resistant ver. 4
FWHM	Full Width Half Maximum
GEM	Gas Electron Multiplier
GEANT	Detector Description and Simulation Tool
GSI	Gesellschaft fr Schwerionenforschung
GUI	Graphical User Interface
HARGD	High Angular Resolution Gamma Detector (OBELIX)
HPD	Hybrid PhotoDetector
IEEE	Institute of Electrical and Electronics Engineers
I/O	Input/Output
ISR	Intersecting Storage Rings
JDF	Jet Drift Chamber (OBELIX)
JTAG	Joint Test Action Group, common name for the IEEE 1149.1 standard
K2K	KEK to Kamioka neutrino experiment
KEK	Koo Energy Ken
LEAR	Low Energy Antiproton Ring
LED	Light Emitting Diode
LET	Linear Energy Transfert
LSB	Least Significant Bit
LVDS	Low Voltage Differential Signal
LV-TTL	Low Voltage TTL Signal
MA-PMT	Multi Anode PMT
MC	MonteCarlo
MCNP4b	General MonteCarlo code for Neutron and Photon transport, version 4 rev. b
MCP	Micro Channel Plate
m.i.p.	minimum ionizing particle
MUSASHI	Monoenergetic Ultra-Slow Antiproton Source for High-precision Investigations
MWPC	Multi Wire Proportional Chamber
MRS-APD	Metal Resistive layer Semiconductor APD
NIM	Nuclear Instrument Module
PBD	Phenyl-Biphenyl-Diazole
PCB	Printed Circuit Board
PC	Personal Computer
PCI	Peripheral Component Interconnect
PDE	Photon Detection Efficiency
PhoNeS	Photo Neutron Source
PLL	Phase Lock Loop
PMMA	PolyMethyl MethAcrylate

PMT	PhotoMultiplier Tube
POPOP	P-bis-phenyloxazolyl-benzene
PS	Proton Synchrotron
PSB	Proton Synchrotron Booster
PVC	PolyVinylChloride
PVT	PolyVinylToluene
QDC	Charge to Digital Converter
Q.E.	Quantum Efficiency
RAM	Random Access Memory
RF	RadioFrequency
RFQD	RadioFrequency Quadrupole Decelerator
r.m.s.	root mean square
SCI-FI	SCIntillating FIbers
SiPM	Silicon PhotoMultiplier
SFD	Scintillating Fiber Detector (UA2)
SPC	Spiral Projection Chamber (OBELIX)
SPS	Super Proton Synchrotron
S/N	Signal over Noise ratio
TDC	Time to Digital Converter, also stands for Time to Digital Converter unit
ToF	Time of Flight
TTL	Transistor Transistor Logic
TSSOP	Thin-Shrink Small Outline Package
VHDL	Very high speed integrated circuit Hardware Description Language
VLPC	Visible Light Photon Counter
VLSI	Very Large Scale of Integration
VME	Versa Module Europe
3HF	3-HydroxyFlavone

List of Figures

1.1 The first antiproton annihilation event detected with the emulsions 4
1.2 The PS complex and LEAR. 6
1.3 Annihilation cross section for $\bar{p}$ and $\bar{n}$ between 200 MeV/c and 800 MeV/c 7
1.4 Annihilation cross section for $\bar{p}$ and $\bar{n}$ for p<100 MeV/c 8
1.5 The plan of the Antiproton Decelerator. 11
1.6 The Antiproton Decelerator cycle. 12
1.7 Scheme of the proposed experimental setup. 15

2.1 Electron energy states in an organic molecule 21
2.2 Cross section of single and double cladding fibers. . . . 23
2.3 Light emission of particles crossing a fiber. 24
2.4 Light collection and limit angle. 24
2.5 The fiber doublet ribbon. 26
2.6 Square fiber photo and configuration scheme. 27
2.7 An image intensifier system with CCD readout. 29
2.8 The front face of a Multianode Photomultiplier. 30
2.9 Scheme of an avalanche photodiode. 32
2.10 Scheme of a Silicon Photomultiplier. 33
2.11 Scheme of the Visible Light Photon Counter. 35
2.12 A picture of a VLPC array. 36
2.13 The geometry of the UA2 Scintillating Fiber Detector. 37
2.14 Pulse height and residual plots for the UA2 Detector . 38
2.15 Overview of the D0 scintillating tracker. 39
2.16 Pulse height and residual plots for the D0 detector. . . 40

3.1 Efficiency profile on the anode surface. 43
3.2 First prototype time resolution and light propagation speed. 44
3.3 2D profile and efficiency for the ø=2 mm fiber module. 45
3.4 Efficiency of the ø=1 mm fiber module: experimental setup and results. 46

3.5 The VA64TAP2.1 channel architecture 48
3.6 Photo of the bonded VA64TAP2.1+LS64_2 pair. 50
3.7 Picture of the first prototype VA64TAP2.1 board. . . . 51
3.8 VA64TAP2.1 pedestal plots and photo of the LED matrix. 53
3.9 Threshold scans and threshold uniformity. 54
3.10 Time diagram for one hit channel, as seen by the FPGA. 55
3.11 Arrival time distribution, with digital readout. 56
3.12 The VA64TAP2.1 board, photo and block diagram. . . 58
3.13 Threshold scan and gain and offset uniformity. 59
3.14 Photo of the repeater boards 60
3.15 Connection scheme for the complete DAQ chain. 61
3.16 Diagram of the I/O–FPGA comunication. 62
3.17 Schematic and picture of the stereo fiber module. . . . 64
3.18 The fiber-PMT alignment mask, before and after the fiber insertion. 64
3.19 Pull and pulse height distributions for the fiber prototype. 66
3.20 Number of hits per layer and beam profile plots. 66
3.21 Hit reconstruction with the triangles method. 67
3.22 Heights of the smallest reconstructed triangle. 67
3.23 Prototype residuals using the Silicon detector tracks. . 68
3.24 Fiber placing on the plexiglass cylinder. 70
3.25 The inner layer and the whole detector after completion. 71
3.26 An exploded view of a slice of the FAST detector. . . . 71
3.27 The fibers in the alignment mask and the PMT supports. 72
3.28 View of the assembled FAST scintillating fiber tracker. 73
3.29 Vertex reconstruction efficiency vs. z, from simulation . 75
3.30 Simulated distribution of the height of the triangles for the inner layer 76
3.31 Residuals for the z and x directions, from simulation . 77
3.32 Residuals for the x and z directions, considering only the scattering. 77
3.33 Spatial resolution vs. z and r, from simulation. 78

4.1 The frontend boards connected to the photomultipliers 81
4.2 Front and side view of FAST during the cosmic ray run. 82
4.3 Arrival time distribution and time resolution vs. threshold. 83
4.4 Plot explaining the time distribution generated by the fluctuations in the pulse heights. 83
4.5 Efficiency of the fiber layers as a function of the threshold. 85
4.6 Example of a 2D cross talk histogram. 86
4.7 Cross talk before and after the alignment, and as a function of the threshold 87

4.8 Distribution of the triangle heights, for the cosmic run. 88
4.9 Triangle heights vs. fiber ϕ position. 89
4.10 2D residual distributions. 89
4.11 ϕ and z residual distributions, for the inner and outer shells 90
4.12 ϕ and z residual, with the nearest triangle method. . . 91
4.13 Residuals for the z and x directions, from a MC simulation considering the single plane resolution of the cosmic ray run 92
4.14 Overall view of the AD experimental lines 93
4.15 The vacuum system and the detector before the integration. 95
4.16 Photo of the beam line and of the complete setup. . . . 97
4.17 The target inside the FAST tracker. 98
4.18 Scope tracks and FAST arrival times, before the beam tuning. 99
4.19 Scope tracks and FAST arrival times, after the beam tuning 100
4.20 The time selection for one event reconstruction. 101
4.21 The first collected annihilation event. 101
4.22 Arrival times with the empty vessel and the tin target. 103
4.23 Distributions of the vertex z position, for different radial cuts 104
4.24 XY vertex distributions at different z 106

5.1 The prototype VA64TAP2.1 board, in the neutron ToF configuration 110
5.2 Relative neutron fluxes in comparison with the activation method; comparison of the arrival time distributions of the prototype and a reference BF_3 counter . . . 111
5.3 Arrival time distributions for different detector positions. 113
5.4 Neutron spectra from the MCNP4B-GN simulation, and comparison between measured and simulated ToF . . . 114
5.5 A GEM photo and scheme of the GEM electric field . . 115
5.6 Scheme of a triple GEM detector, and picture of the tested GEM assembly. 116
5.7 Pulse height and pull distributions, with the cuts used for the event selection. 119
5.8 2D profile obtained with the GEM detector. 119
5.9 Time distribution of the GEM hits. 120
5.10 Fiber profilometer during the assembly phase 122
5.11 Alignment masks and complete module at the Frascati BTF 123

5.12 Spatial resolution of the 2 profilometer planes. 124
5.13 The crystal strips on the goniometer and a particle crossing a bent crystal (scheme). 126
5.14 Beam profile as a function of the crystal angle set by the goniometer 127

A.1 Scheme of the OBELIX apparatus. 134
A.2 The subset of the OBELIX detectors used for the measurement of the $\bar{p}$-p and $\bar{p}$-A annihilation cross sections 135
A.3 2D plot of the annihilation time vs. the vertex z coordinate 137

B.1 Snapshot of the data acquisition software control window 140
B.2 Header of the ASACUSA raw data ntuple 141

List of Tables

1.1 Transverse emittance and momentum spread during the various phases of the AD cycle. 13

2.1 Properties of the most widespread waveshifters 21
2.2 Bicron BC-400 plastic scintillator properties. 22
2.3 Bicron BCF-10 scintillating fiber properties. 25
2.4 Parameters of the Hamamatsu R7600-M64 photomultiplier. 30
2.5 Optical cross talk for a multianode photomultiplier. . . 31

3.1 Complete list of properties of the R7600-M64 photomultiplier. 42
3.2 The main VA64TAP2.1 specifications. 49
3.3 The Altera Cyclone 2 EP2C8Q208C7 specifications. . . 51
3.4 Geometrical parameters of the six fiber layers. 70
3.5 Number of charged mesons from the $\bar{p}$–H annihilation. 74

4.1 Summary of the data collected with different targets. . 102

5.1 Bicron BC-454 plastic scintillator properties. 109
5.2 Voltage settings for the test of the GEM detector. . . . 118

Bibliography

[1] P. Dirac, Proc. Roy. Soc. London A126, 360-365 (1930).

[2] C.D. Anderson, Phys. Rev. 43, 491-494 (1933).

[3] H.S. Bridge et al., Phys. Rev. 95, 1101-1103 (1954).

[4] E. Amaldi et al., Nuovo Cimento 1, 492-500 (1955).

[5] H.S. Bridge et al., Phys. Rev. 102, 930-931 (1956).

[6] O. Chamberlain, Phys. Rev. 100, 947-950 (1955).

[7] B. Cork et al., Phys. Rev. 102, 1193-1197 (1956).

[8] N. Barash et al. Phys. Rev 139, 1659 (1965).

[9] C. Baltay et al., Phys. Rev. 140, 1039 (1965).

[10] C. Baltay et al., Phys. Rev. 140, 1042 (1965).

[11] R. Armenteros and B. French, *High-Energy Physics* vol. 4, New York, Academy Press (1969).

[12] M. Chiba et al., Phys. Lett. B177, 217 (1986).

[13] M. Chiba et al., Phys. Lett. D36, 3321 (1987).

[14] R. Klapisch, Hyperfine Interactions 24, 311-319 (1985).

[15] G. Bendiscioli and D. Kharzeev, Rivista del Nuovo Cimento 17, 1 (1994).

[16] V.G. Ableev et al., Il nuovo Cimento A107, 943 (1994).

[17] E. Botta, Nuclear Physics A692, 39-46 (2001).

[18] M. Astrua et al., Nuclear Physics A697, 209-224 (2002).

[19] A. Zenoni et al., Phys. Lett. B461, 413-416 (1999).

[20] A. Zenoni et al., Phys. Lett. B461, 405-412 (1999).

[21] A. Bianconi et al., Phys. Lett. B481, 194-198 (2000).

[22] A. Bianconi et al., Phys. Lett. B492, 254-258 (2000).

[23] L.I. Schiff, *Quantum Mechanics*, McGraw Hill, New York (1968).

[24] K.V. Protasov and R. Duperray, Proceedings of the 9^{th} International conference on hadron spectroscopy, 783-785 (2000).

[25] K.V. Protasov, Nucl. Phys. A692, 112-115 (2001).

[26] K.V. Protasov et al., Eur. Phys. J. A7, 429-434 (2000).

[27] A. Gal et al., Phys. Lett. B491, 219-224 (2000).

[28] C.J. Batty et al., Nucl. Phys. A689, 721-740 (2001).

[29] S. Maury, Hyperfine Interactions, 109, 43-52 (1997).

[30] P. Belochitskii et al., CERN/PS 2002-046-OP (2002).

[31] S. Maury, CERN/PS 99-50-HP (1999).

[32] M. Brouet et al., Proceedings of the 1999 Particle Accelerator Conference 1, 562-564 (1999).

[33] E. Klempt et al., Phys. Rep. 413, 197-317 (2005).

[34] G.T. Reynolds, IRE Trans. Nucl. Sci. NS-7, 115 (1960).

[35] H.C. Burrows et al., Nuclear Electronics I, 153 (1962).

[36] S.R. Borenstein et al., IEEE Trans. Nucl. Sci. NS-31, 396 (1984).

[37] J.B. Birks, *Theory and Practice of Scintillation Counting*, New York, MacMillan (1964).

[38] Th. Forster, Z. Naturforsh. A 4, 321 (1949).

[39] I.B. Berlman, *Handbook of Fluorescence Spectra of Aromatic Molecules*, New York, Academic Press (1971).

[40] R.C. Ructhi, Annu. Rev. Nucl. Part. Sci. 46, 281319 (1996).

[41] T.O. White, Nucl. Inst. and Meth. in Phys. Res. A273, 820-825 (1988).

[42] B. Baumbaugh et al., IEEE Trans. Nucl. Sci. 43(3), 1146 (1996).

[43] I. Efthymiopoulos, arXiv:hep-ex/0510078 v1 31 (2005).

[44] J.M. Gaillard et al. (UA2 Collaboration), Proc. DPF Conf., Eugene, Oregon, 921 (1985).

[45] A. Suzuki et al. (K2K Collaboration), Nucl. Inst. and Meth. in Phys. Res. A453, 165-176 (2000).

[46] N. Tagg et al., Nucl. Inst. and Meth. in Phys. Res. A539, 668-678 (2005).

[47] T. Yoshida, T. Sora, Nucl. Inst. and Meth. in Phys. Res. A534, 397-402 (2004).

[48] H. Dautet et al., Applied Optics, 32 (21), 3894-3900 (1993).

[49] S. Vasile et al., SPIE Proceedings, 3765, 2-11 (1999).

[50] A. Akindinov et al., Nucl. Inst. and Meth. in Phys. Res. A387, 231 (1997).

[51] G. Bondarenko et al., Nucl. Inst. and Meth. in Phys. Res. A442, 187 (2000).

[52] E. Guschin et al., Nucl. Inst. and Meth. in Phys. Res. A567, 250-254 (2006).

[53] O. Mineev et. al., arXiv:physics/0606037.

[54] M.D. Petroff, M.G. Stapelbroek and W.A. Kleinhans, Appl. Phys. Lett. 51, 406 (1987).

[55] J. Kim, Y. Yamamoto and H.H. Hogue, Appl. Phys. Lett. 70, 2852 (1997).

[56] E. Waks et al., Quantum Electronics, IEEE Jour. of Sel. Top. in Quant. Elect. 9, 1502-1511 (2003).

[57] A. Bross et al., Nucl. Inst. and Meth. in Phys. Res. A394, 87-96 (1997).

[58] R. Ansorge et al., Nucl. Inst. and Meth. in Phys. Res. A265, 33 (1988).

[59] S.G. Katvars et al., Nucl. Inst. and Meth. in Phys. Res. A276, 482 (1989).

[60] J. Alitti et al., Nucl. Inst. and Meth. in Phys. Res. A279, 364 (1989).

[61] J. Kirkby, CERN/EP 87-60 (1987).

[62] A.D. Bross, Fermilab-Conf-95/030-E

[63] J. Ellison, Fermilab-Conf-01/012-E

[64] S. Glenn et al., Nucl. Inst. and Meth. in Phys. Res. A360, 314-317 (1995).

[65] A.E. Baumbaugh, Nucl. Inst. and Meth. in Phys. Res. A360, 1-6 (1995).

[66] A. Mozzanica et al., Nucl. Inst. and Meth. in Phys. Res. A567, 315-318 (2006).

[67] D. Bolognini et al., Nucl. Inst. and Meth. in Phys. Res. A572, 281-283 (2007).

[68] M. Prest et al., Nucl. Inst. and Meth. in Phys. Res. A501, 280-287 (2003).

[69] U. Koetz et al., Nucl. Inst. and Meth. in Phys. Res. A235, 481 (1985).

[70] M. Krammer et al., Nucl. Inst. and Meth. in Phys. Res. A397, 232-242 (1997).

[71] G. Barbiellini et al., Nucl. Inst. and Meth. in Phys. Res. A490, 146-158 (2002).

[72] G. Mazzitelli et al., Nucl. Inst. and Meth. in Phys. Res. A515, 516-534 (2003).

[73] GEANT 3.2.1, CERN Library Report No. W5013, (1993).

[74] M. Giovannozzi et al., CERN/PS 98-047 CA (1998).

[75] G. Charpak et al., Nucl. Inst. and Meth. in Phys. Res. 62, 202-226 (1968).

[76] F. Sauli, CERN/EP 98-051 (1998).

[77] M. Hori, Rev. Sci. Instr. 76, 113303 (2005).

[78] M.C. Fujiwara, Nucl. Inst. and Meth. in Phys. Res. A484, 162-173 (2002).

[79] M. Hori et al., Nucl. Inst. and Meth. in Phys. Res. A496, 102122 (2003).

[80] International Atomic Energy Agency, "Current status of neutron capture therapy", IAEA-TEDOC-1223, ISSN 1011-4298, Vienna: IAEA, 2001.

[81] R. Bevilacqua et al., Nucl. Inst. and Meth. in Phys. Res. A572, 231-232 (2007).

[82] G. Bartesaghi et al., Nucl. Inst. and Meth. in Phys. Res. A572, 228-230 (2007).

[83] V. Conti et al., Nucl. Inst. and Meth. in Phys. Res. A581, 88-90 (2007).

[84] E. Steinnes, "Activation Analysis in Geochemistry and Cosmochemistry", edited by A. O. Brunfelt and E. Steinnes, Universitetsforlaget, Oslo, 113- 128, (1971).

[85] A. Zanini et al., Phys. in Med. and Biol. 49, 571-582 (2004).

[86] F. Sauli, Nucl. Inst. and Meth. in Phys. Res. A386, 531 (1997).

[87] S. Bachmann et al., Nucl. Inst. and Meth. in Phys. Res. A438, 376 (1999).

[88] S. Bachmann et al., Nucl. Inst. and Meth. in Phys. Res. A470, 548 (2001).

[89] G. Bencivenni et al., Nucl. Inst. and Meth. in Phys. Res. A478, 245 (2002).

[90] G. Bencivenni et al., Nucl. Inst. and Meth. in Phys. Res. A488, 493 (2002).

[91] M. Alfonsi et al., IEEE Nuclear Science Symposium Conference Record, V1, 5-9 (2004).

[92] B. Ketzer et al., IEEE Trans. Nucl. Sc. 49, 2403 (2002).

[93] T. Zeuner et al., Nucl. Inst. and Meth. in Phys. Res. A446, 324 (2000).

[94] M. Bozzo et al., Design and construction of the Triple-GEM detector for TOTEM, IEEE Nuclear Science Symposium Conference Record, V1, 5-9 (2004).

[95] Z. Fraenkel et al., Nucl. Inst. and Meth. in Phys. Res. A546, 466 (2005).

[96] M.J. French et al., Nucl. Inst. and Meth. in Phys. Res. A466, 359-365 (2001).

[97] E. Noschis et al., Nucl. Inst. and Meth. in Phys. Res. A572, 378-381 (2007).

[98] B. Ketzer et al., IEEE Trans. Nucl. Sc. 48, 1065-1070 (2001).

[99] A. Kaukher, IEEE Trans. Nucl. Sc. 53, 749- 755 (2006).

[100] G. De Geronimo et al., IEEE Trans. Nucl. Sc. 51, 1312-1317 (2004).

[101] J. Hoff et al., published in the 2005 IEEE Nuclear Science Symposium proceedings.

[102] J. Lindhard, Phys. Lett. 12, 126 (1964).

[103] G.R. Piercy et al., Phys. Rev. Lett. 10(4), 399 (1963).

[104] E.N. Tsyganov, Fermilab reports TM-682, TM-684 (1976).

[105] R.W. Assmann et al., PAC06 proceedings (2006).

[106] W. Scandale et al., Phys. Rev. Lett. 98, 154801 (2007).

[107] A. Adamo et al., Sov. Jour. Nucl. Phys. 55, 1732 (1992).

[108] S. Affatato et al., Nucl. Inst. and Meth. in Phys. Res. A325, 417 (1993).

[109] A. Zenoni et al., Nucl. Inst. and Meth. in Phys. Res. A447, 512-535 (2000).

Acknowledgements

I would like to acknowledge the institutions which gave support to the described research, i.e. the INFN (Section of Pavia) and University of Brescia. Many thanks also to the whole ASACUSA collaboration, for the strong support and the fruitful discussions during the beam time, and for the warm welcome they all reserved to me and our group of newcomers. A special word to Masaki Hori, whose thoughts and suggestions have been of crucial importance for us.
I would like to thank also the crew of the Antiproton Decelerator at CERN, who performed a lot of efforts to fullfil our demanding requests.
Thanks to Prof. Lodi Rizzini for the opportunities he gave me, for the valuable learnings received from him and, most importantly, for trusting me. Together with him, I would like to acknowledge the whole team at Brescia University: Luca, Maurizio, Nicola, Marco and Giorgio.
Thanks to my tutor Prof. Iori, for the valuable and spontaneous help received during this thesis work.
A few good words go to Valerio, whose help and friendship has been so important during the whole genesis of this thesis.
Tanks also to Davide, that was with me during the whole board production and testing (and of course at CERN too).
Special thanks to all the other students at the Physical Department at the University of Insubria: Ale, Andrea, Cri, Dani, Giacomo, Said, Selly, Valentina. With their presence they made the working place a warm place.
I have to thanks Erik for the things he could teach me, for the support given during the whole duration of this work and for the extreme kindess always reserved to me.
I warmly thanks Michela for... well, here the list should be very long. In one word, is she that made everything possible. I have been very lucky to work with her.
My last words are for my family, for always being there..